DISS ETH NO.24128

PLASMONIC COLOR FILTERS FOR INDUSTRIAL APPLICATIONS

A thesis submitted to attain the degree of

DOCTOR OF SCIENCES of ETH ZURICH

(Dr. sc. ETH Zurich)

presented by

LUC DUEMPELMANN

Master of Science in Nanosciences,
University of Basel

born on 15.12.1986

citizen of Switzerland, Frauenfeld TG

accepted on the recommendation of

Prof. Dr. Lukas Novotny, examiner
Prof. Dr. David J. Norris, co-examiner
Prof. Dr. Harald Giessen, co-examiner

2017

Abstract

Light can strongly interact with metallic nanostructures, leading to resonant excitation of the confined electrons. This results in a strong near-field enhancement with subwavelength confinement. The resonance condition can be controlled by the material, shape and surrounding of the metal nanostructures. Thus, this so-called field of plasmonics holds great potential for applications in photonics. Besides biosensing, novel applications are scarce though, not only due to challenges in the up-scaling process, but also because of expense of material, design complexity and sensitivity of the structures in ambient conditions. Furthermore, intrinsic losses impede the implementation compared to competing alternatives.

This thesis describes the development and realization of color filters based on plasmonic structures. The structures are tailored for intriguing applications and their large-scale manufacturing. Specifically the variability of plasmonic color filters is exploited and applied. This precisely controllable change of color appearance can be essential for applications such as optical security or imaging systems, for which first realizations are presented here.

In particular, color filters are investigated, which strongly change their optical appearance with the angle of incidence. Additionally, a given color is only visible from one tilt direction. This unique feature makes these color filters highly attractive for optical security applications. Further, the high sensitivity to the surrounding material can be utilized; a position dependent modification of the color filters can be achieved by inkjet printing of transparent inks with different refractive indices. Additionally, a different set of plasmonic color filters are studied, which can be precisely controlled with the incident polarization while having almost angle-independent optical properties. This renders them ideal for camera filters, where a large-field-of-view is desired. By controlling the optical properties of the filters, a plasmonic multispectral imaging device is demonstrated. Overall, the used fabrication methods and materials are compatible with large-scale and cost-efficient manufacturing methods. Thus this thesis may help paving the way for everyday products based on plasmonics.

Zusammenfassung

Starke Interaktion von Licht mit metallischen Nanostrukturen führt zu resonanter Oszillation bestimmter Elektronen. Dies resultiert in einem verstärkten Nahfeld im Subwellenlängenbereich. Die Resonanzbedingung kann durch das Material, die Form, oder die Umgebung der Metall-nanostrukturen verändert werden. Deshalb birgt das Gebiet der Plasmonik grosses Potenzial für Anwendungen im Bereich der Photonik. Abgesehen von Biosensoren, ist die Realisierung von neuartigen Anwendungen jedoch selten. Dies liegt einerseits an Problemen bei der Fabrikation im industriellen Massstab, anderseits an Materialkosten, der Komplexität sowie der hohen Anfälligkeit der Struktur im Alltagsgebrauch. Zudem erschweren intrinsische Streuverluste die Anwendung im Vergleich zu konkurrierenden Alternativen.

Diese Dissertation beschreibt die Entwicklung und Realisierung von Farbfiltern mit Hilfe von plasmonischen Strukturen. Diese sind für anspruchsvolle Anwendungen und deren Herstellung geeignet. Insbesondere wird die Veränderlichkeit von plasmonischen Farbfiltern genutzt. Diese genau kontrollierbare Veränderung der Farberscheinung kann für Anwendungen wie optische Sicherheits- oder Abbildungssysteme, für welche erste Realisierungen gezeigt werden, von wesentlicher Bedeutung sein.

Die erste Entwicklung, die in dieser Arbeit untersucht wurde, sind Farbfilter, welche ihre optischen Eigenschaften stark unter dem Einfallswinkel verändern. Dabei ist die jeweilige Farbe nur aus einer Richtung sichtbar. Diese einzigartige Eigenschaft macht die Farbfilter für optische Sicherheitsanwendungen sehr interessant. Ferner kann die starke Abhängigkeit des optischen Effekts von der Umgebung ausgenutzt werden; mit Hilfe eines kommerziellen Tintenstrahldruckers und transparenten Materialien mit unterschiedlichen Brechungsindizes wird eine ortaufgelöste Anpassung der Farberscheinung ermöglicht. Des Weiteren wurden winkelunabhängige plasmonische Farbfilter entwickelt, welche mit der Polarisation des Lichtes präzise gesteuert werden können. Solche Farbfilter sind ideale Kandidaten für Kamerafilter, bei denen ein grosses Gesichtsfeld erwünscht ist. Schlussendlich wurde die Kontrolle der optischen

Eigenschaften verwendet um eine plasmonische Multispektrale-Kamera zu realisieren. Insgesamt sind die eingesetzten Fertigungsprozesse und -materialien kompatibel mit grosstechnischen und kostengünstigen Verfahren. Diese Dissertation könnte dabei helfen, den Weg in Richtung plasmonische Alltagsprodukte weiter zu ebnen.

Acknowledgments

First, I would sincerely like to thank Benjamin Gallinet for his great supervision and guidance throughout the entire thesis. In weekly meetings I learned a lot from him about plasmonics, simulation tools and how to write papers. Further, I strongly want to thank Daniele Casari and Judith Müller for their great work in the lab. Great thanks to Fabian Lütolf, a former PhD student, who inspired me in many things I was finally doing; Angelique Luu-Dinh who was a great support and teacher in the lab; Guillaume Basset for numerous discussions on industrial applications and his work with patenting; and Igor Zhurminsky for introducing me with the laser interference lithography setup. Furthermore, I would like to thank the entire CSEM team for their support and patience, in particular Nicolas Glaser, Jan Mayer, Christian Seitz, Fabienne Herzog and Florian Schleiss. Finally, I would like to thank Marc Schnieper and Christian Bosshard for this great opportunity to carry out my thesis at CSEM. As well as for the possibility they gave me to present my work at several events and conferences.

To no lesser extent I would strongly like to thank Lukas Novotny for the very inspiring and fruitful collaboration, the time and patience he took for this project and the provoking questions he confronted me with. Although I have not been to Zurich on a weekly basis, Lukas and the group members always were a great source of inspiration and discussions; in particular thanks to Zachary Jordan Lapin, Shawn Divitt, Achint Jain. Also thanks to the nano-optic group for the great time outside the lab, in particular to Nikolaus Flöry, Xavier Palou, Cynthia Gruber, Markus Parzefall and Vijay Jain. Finally, special thanks also to Barbara Schirmer for taking care of me. And Sarah Kurmulis for the great idea of using art in science.

Additionally, special thanks to David Hasler and Amina Chebira from CSEM Neuchâtel for inspiring discussions and technical advices concerning the camera application; And the PhD club of CSEM, which was a great network for exchange. I would also like to thank Michael Gerspach for the inspiring coffee break. Further, I would strongly like to thank Benjamin Bircher, Nicholas Arnold, Ralf Dümpelmann, Nicolas Glaser, Fabian Lütolf, Julia Ebner and of course Benjamin Gallinet for reading and correcting parts of this thesis.

A great thanks to my friends how supported and encouraged me. In particular to the ones not active in the field of science, who brought me back down to the ground of reality and showed me that the world outside the "PhD bubble" is not that complex. Also to my badminton and surf mates who helped me to refresh my mind.

Special thanks to my family who gave me the love and support to reach my goals. Specifically I would like to acknowledge my father Ralf who was a great source of inspiration throughout my scientific career and still is; My mother Ursula who always doubtless supported me in what I was doing; And my sister Lea; it is great how we push ourselves further. Special thanks to my partner Julia who supported me restless and unconditionally throughout the thesis; and I assume will be the only "non-scientist" who has read my papers.

Foreword

I have performed all of the work presented in this dissertation, with the following exceptions.

- Chapter 3: The final samples as well as further improvement of the immersed laser interference setup was done by Daniele Casari, see Figure 3.5 and 3.7. Further the SEM image of Figure 3.1 was done by him.

- Chapter 4: The laboratory work of Chapter 4 was done by Judith Müller. This includes fabrication of samples, testing of inks and measurements of the samples. Further the final sample, see Figure 4.5 was done by her.

- Chapter 5: The SEM image in Figure 5.5 was done by Zachary Jordan Lapin.

The work presented in this thesis was performed mainly at the Swiss research institute CSEM SA, in fruitful conjunction with the group of Lukas Novotny at ETH Zurich. The work was financed by CSEM.

Table of Contents

3   Color Rendering Plasmonic Aluminum Substrates with Angular Symmetry Breaking   24

1   Introduction

Structural Colors

For million of years, nature has displayed its beauty in the whole diversity of colors. This elaborate coloration is sometimes just a by-product of molecular absorption. But often, a colorful appearance is specifically designed to attract conspecific or to deter predators, ensuring the survival of a species. Likewise, for mankind color generating structures are of key importance for various applications in daily life such as for decoration, identification and perception. Obviously, there is a great demand for further development of current technologies. Absorbing dyes or pigments form the major part of color substances, in nature but also nowadays in consumer products,[1] with about 15'000 being synthesized on an industrial scale.[2] Recently it was discovered, that several species, *e.g. Morpho butterfly*, not only use dyes and pigments for coloration but incorporate additional complex color generating structures showing thin film and multilayer interference and diffractive effects.[3,4] The structural coloration arises from interaction of light with nano- or micro-structured surfaces. Often these structural colors are strongly angle-dependent and iridescent. To produce diffuse reflected light, a combination of regular and irregular structures is used.[5] Another example is the *chameleon*; its variable skin coloration is based on active tuning of photonic crystals.[6] This great variety of optical effects, present for over 500 million years,[7] has inspired biomimetic research.[8,9] Interestingly some of the first structural colors made by mankind date back to the glass makers and alchemists of the Bronze Age.[10,11] "Nanometric-sized" gold or silver particles were dispensed in glass allowing a colorful appearance.[12] The most prominent example is the Lycurgus cup made in the 4th century AD.[13] While transmission through the cup appears to be red, reflection is green. It was only in the 1850s that this non-obvious effect could be explained by the interaction of light with metal particles.[14] Later, this effect was related to the field of plasmonics.[15,16]

Plasmonics

The scientific discovery of plasmonic effects dates back to 1902 and the observation of an anomalous intensity change in the reflection spectra of metallic gratings by Richard W. Wood.[17] Whereas one part of the effect was related to diffractive effects, described by Lord Rayleigh,[18] the other part can now be clearly related to the generation of surface plasmons.[19,20] Later, a unifying theory described a novel type of resonances, the so-called Fano resonances, featuring an asymmetric line shape.[21] Such resonances are not limited to optical phenomena but are also present in many other physical areas, thus being one of the most important discoveries of the 20th century.[22] The field of plasmonics itself experienced a rediscovery after the observation of "extraordinary transmission" through subwavelength holes in 1998.[23] Surface plasmons facilitate transmission of a greater amount of light through these apertures than geometrically expected. Since then the field of plasmonics has rapidly expanded into many scientific areas demonstrating its great potential.[16,24,25] The ability of plasmonic structures to generate extremely strong and confined fields in the subwavelength scale[16] facilitated the first and most prominent application: the surface plasmon resonance sensor.[26] By further exploiting these features, novel biosensors were developed.[27,28] The working principle is based on the strong sensitivity of the plasmon resonance to its surroundings. The underlying strong near-field enhancement and possibly arising hot carrier generation[29] show great potential for enhancing the efficiency of photovoltaics[30–32] and photodetectors[33–35] or for enabling chemical reactions[36] and vapor generation.[37] The strong and highly localized interaction of light with electrons is utilized in hybrid circuits merging the fields of plasmonics and electronics.[38–40] Such devices could ultimately replace classical semiconductor circuits, due to potentially very small device dimensions and high operating speed.[41–43] Besides, a nanoscale surface plasmon laser, so-called spaser, was described[44] and demonstrated.[45] The small device dimensions arise from the resonant property of plasmonic structures, leading to a possibly "high printing resolution" of plasmonic structures.[46] Plasmonic color substrates include and utilize such plasmonic structures for controlled color generation. More details are discussed in Section 2.2. Closely linked to the strong resonant interaction with light is the capability of modifying the light in such a way, as to have optical properties, which are not found in nature: the so-called field of metamaterials.[47–50] The most prominent examples of metamaterials are negative refractive index materials,[51,52] which can be utilized for "perfect lenses"[51] or cloaking.[53,54] Other examples include metalenses,[55–58] perfect absorbers[59,60] or phase shaping structures.[61] Overall the field of plasmonic color structures and

metamaterials have a high congruence,[i] as shown in the example of optical holography by plasmonic metasurface.[62,63] More recently the confinement of plasmonics within 2D materials (*e.g.* graphene) and the interaction with quantum emitters[64–69] has gained strong interest. After a peak of excitement about potential applications in the fields of plasmonics, it turned out that one of the limiting factors are challenges in up-scaling the fabrication processes and the losses induced by the plasmonic material itself[70,71] (see discussion in Section 2.3.4). Nevertheless, plasmonic structures are present in many diverse scientific areas and eventually will find their way into applications.[20] After first applications in biosensing, it is very likely that the next ones will be in the field of plasmonic structural colors.[72,73]

Applications

Plasmonic color substrates can be applied for long-lasting and stable surface decorations, optical security, display and camera filters, sensors, and optical data storage.[74,75] Besides potential ease of fabrication and wide spectral tunability, plasmonic structures outperform their chemical counterparts thanks to their high resolution beyond the diffraction limit, higher compactness and non-bleaching.[46,72,76] These properties make plasmonic structures valuable for tunable, compact and flexible decorative elements and suitable for illumination, art or advertising purposes. In addition, the field of optical security is constantly seeking for novel optical effects less prone to counterfeiting. A majority of holograms used today are still based on diffractive effects,[77,78] but recently, security elements based on plasmonics were demonstrated[79,80] and are now commercially available.[81] Besides, displays and cameras are present in many fields of daily life. They utilize color filters to narrow a broadband source for emitting colors or measure the color composition of reflected light. There is great demand for improving such devices in terms of tunability, compactness and flexibility.[72,75] Finally, the field of optical sensing, for biological or physical purposes, has been of great interest. A minute change in refractive index of the surrounding can cause a strong modification of the plasmon resonance.[82,83] One could imagine a disposable plasmonic sensor, of which a color shift could be read out by a commercial camera.

Fabrication

For appropriate control of the light – metal interaction, the metals have to be structured with subwavelength dimensions. In the visible range this corresponds to ∼50-300 nm. Compared to the chemical synthesis of dyes or pigments, the fabrication of plasmonic structures requires sophisticated machines for fabrication and alignment of such structures. Due to recent advances

---

[i]Throughout the thesis I will relate the generation of colors based on periodically arranged and subwavelength spaced metallic nanostructures to the field of plasmonics and limit metamaterials to above mentioned examples.

in nanofabrication tools, lithographically-defined nanostructures can be manufactured with high resolution and reliability.[84] Generally such methods (*e.g.* electron-beam lithography) are very versatile for fabrication of small-scale samples for proof-of-concept purposes. But nanomanufacturing, *i.e.* "the commercially scalable and economically sustainable mass production" of nanostructures, requires low cost, high throughput and fast time to market.[85] These requirements strongly restrict the methods and material of choice accompanied by a limited variety of plasmonic structures. But ultimately, appropriate choice assures large-scale and cost-efficient manufacturing paving the way towards consumer products. These ambiguous factors can have major consequences on the final product and application, highlighting the importance of appropriate material and fabrication methods for the design of novel plasmonic devices.

Objective

The objective of this thesis is to develop plasmonic color substrates, which can be utilized for novel kinds of applications. The work includes the design and evaluation of outstanding properties compared to other color substrates, a fabrication method compatible with large-scale manufacturing using abundant materials and optical characteristics satisfying the requirements of potential applications.

Motivation

Color efficiency and contrast of plasmonic color substrates are often significantly lower than those of alternative color generating substances or structures (*e.g.* dyes or multilayers), leading to pastel-like colors.[75] Consequently, when considering only the color contrast and brightness there is no direct financial or color-related benefit of plasmonic colors compared to chemically synthesized colors. However, one of the most outstanding and distinguishing features of plasmonic color substrates is the controlled and dynamic variability of the color generation *in situ*. Plasmonic color substrates can work in transmission or reflection, but a greater potential is most likely in applications of transmission, *e.g.* camera filters. Due to the resonant nature of plasmonic substrates, a strong optical response can be obtained, while keeping a high overall transmission. Additionally, the resonant absorption allows working in zero order transmission. Compared to diffractive or multilayer structures, no higher orders or iridescent colors are observed, respectively. This property enables the use of plasmonic color substrates in diffuse environment. Moreover, they can be lithographically defined with a very high spatial resolution,[46] which can be essential for camera or anti-counterfeiting applications. Finally, such structures can be embedded with a protective coating, assuring stability in ambient conditions.

4

Structure of the Thesis

This thesis is organized as follows: Chapter 2 provides an overview of dielectric color substrates as well as different types of plasmonic color substrates. The state-of-the-art design and fabrication of plasmonic substrates will also briefly be discussed. Chapter 3 is dedicated to plasmonic substrates rendering optical symmetry breaking color effects. Such asymmetric transmission is enabled by the tilt geometry of the structure, facilitated by angular evaporation of aluminum. Distinct color appearance is achieved by variation of evaporation angles. Similar structures are used in Chapter 4. Here a novel printing technique is presented to modify the color appearance of geometrically identical structures by printing inks with different refractive indices. Chapter 5 describes polarization-dependent plasmonic color filters. The plasmonic structure enables a wavelength-dependent phase shift of the incident light, leading to four completely distinct transmission states. Besides being sensitive to the polarization in an active manner, the structure is designed to have nearly completely angle-independent transmission properties. Active tunability and angle-stability form essential parameters for active tunable filters suitable for spectral analysis. Chapter 6 describes the concept and realization of such a plasmonic multispectral imaging system. Each chapter will be completed by a short conclusion and includes the experimental details. A general conclusion and outlook is given in Chapter 7.

2 State-of-the-art of Structural Colors
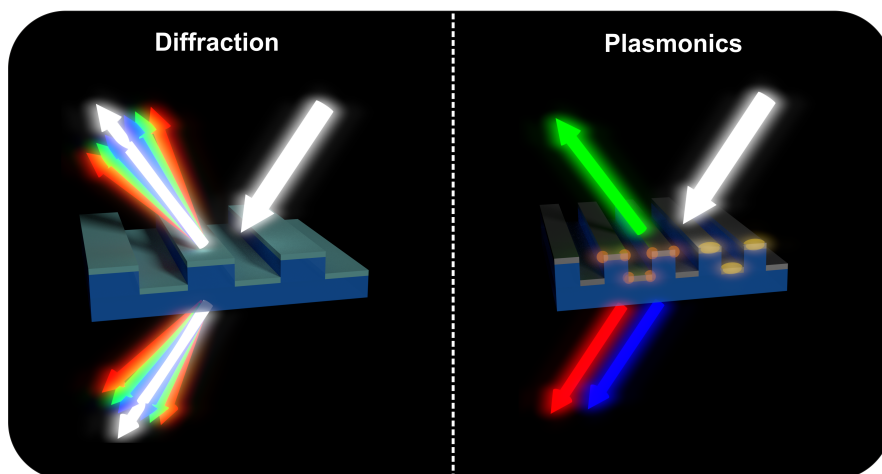
Figure 2.1 – Left: interaction of light with a diffractive dielectric grating. The diffracted light waves interfere and form orders of diffraction, leading to the typical rainbow color generation. Right: Scheme of light interacting with metallic gratings, so-called plasmonics, leading to collective oscillations of the electrons in the metal (yellow) and electromagnetic near-field enhancements (orange). This can lead to a distinct color appearance of reflected (green) and transmitted light (red and blue).

In Section 2.1 dielectric structural color substrates will be discussed. Section 2.2 gives an overview of some of the most popular plasmonic color substrates. It categorizes them by their geometrical structure and discusses their optical properties. In Section 2.3 the process of designing and fabricating plasmonic substrates will briefly be discussed. This includes state-of-the-art fabrication techniques, followed by a process scheme for large-scale fabrication, which was employed throughout this thesis. Further, a brief overview of simulation techniques and plasmonic materials is given.

2.1 Dielectric Structural Color Generation

This section highlights concepts of color generation, which are based on dielectric structures. It includes diffractive gratings, thin films and multilayers, photonic crystals, and nanowires and -particles.

2.1.1 Diffractive Gratings

Diffraction occurs when light (with wavelength λ) is incident on a periodic structure with period p (*e.g.* a grating) and the resulting scattered waves form diffractive orders by interference, see Figure 2.3a. In the Bragg regime, $0.5\,\lambda < p < 2.5\,\lambda$, one or two diffractive orders are present.[86] This is the regime where diffractive colors typically are produced. The intensity maximum at the angles θ_m are given as

$$p(\sin\theta_m + \sin\theta_i) = m\lambda \tag{2.1}$$

with the incident angle θ_i and the number of the diffraction order expressed by the integer m. Through equation 2.1 it is evident that the diffraction angle strongly depends on the wavelength λ, while p and θ_i are kept constant. Hence, under white illumination, the emerging coloration is strongly iridescent, leading to a "rainbow" effect, see Figure 2.3a. While this dispersion can be essential for spectrometers,[87] the lack of color stability and control is often undesired for structural colors.[88] Example given, in diffuse light conditions, diffractive color effects fade out or are challenging to observe, due to a narrow range of appropriate viewing angles,[88] compare with Chapter 3. Modification of the periodic structure or coating with high refractive materials, allows a certain control of diffractive orders.[89] Nevertheless, it is challenging to completely suppress iridescent color generation of a periodic structure (within the Bragg regime).[87] A method to reduce diffractive orders is to use smaller periods, which generate colors in the zeroth diffraction order up to certain tilt angles (see below).[78] In summary, diffraction leads to a wavelength-dependent distribution of light into different angles,[87] but not to an absorption as *e.g.* by dyes[2] or plasmonic structures.[75] Therefore, light is not "lost" but will appear either at diffraction angles or will be trapped in the plane of the structure. Overall, diffractive effects, *i.e.* implemented as diffractive optical variable image device (DOVID), are widely used for optical security.[90,91]
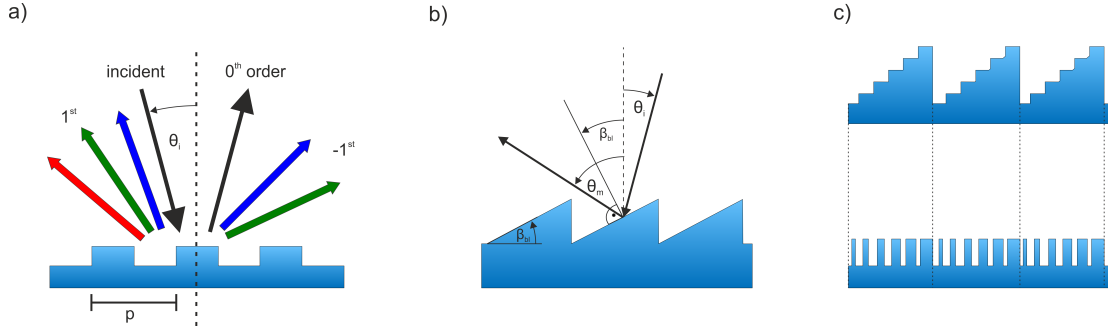
Figure 2.2 – Scheme of a (a) diffractive structure, (b) blazed grating and (c) multilevel (top) and binary (bottom) blazed grating. The different colored parts of the dielectric structure indicate different refractive indices. θ_i: angle of incidence, θ_m: angle of diffraction, β_{bl}: facet angle. Naming convention following Palmer.[87]

Blazed Gratings

The diffraction efficiency of gratings can strongly be enhanced in a given order under certain conditions by using blazed gratings.[87,92] This property is in particular important for applications such as spectrometer,[87] wave-guiding,[93,94] laser cavities,[95] lighting or photovoltaics.[89,96] Blazed gratings generally show a triangular profile with an inclination angle to the surface normal, see Figure 2.2b. The highest efficiency is often achieved if the *blaze condition* ($\theta_i - \beta_{bl} = \theta_m - \beta_{bl}$, see Figure 2.2b) is satisfied.[87] The diffraction efficiency of periodic structures can be calculated using Fourier transforms,[97] which in return can be used to evaluate the design of blazed gratings. Compared to other simulation tools (see Section 2.3.3) certain assumptions and restrictions have to be made, but a rather simple solution can be provided.[97] In general, the field of Fourier optics includes the study of classical optics using Fourier transforms.[98] Hereby Fourier analysis can be utilized to model the optical performance of optical elements, which in particular is well-suited for cascades of optical systems including *e.g.* lenses and phase masks.[97] The continuous profile of the permittivity function of the blazed grating imparts a phase variation across the wavefront. The transmitted wavefront of an incident one onto the grating can be expressed as convolution between a "Dirac comb" and a "rectangle function" multiplied by a phase factor:[97]

$$U(x) = \text{comb}\left(\frac{x}{p}\right) \otimes \text{rect}\left(\frac{x}{p}\right) \exp(i \cdot [2\pi(n-1)d/\lambda] \cdot x/p) \tag{2.2}$$

with the period p and depth d of the grating, the wavelength λ of the incident light and the refractive index of the grating n. Due to the periodicity of the grating, light will propagate away into distinct diffraction orders, which are mathematically the Fourier transform of this convolution.[97] As a result all light can be diffracted into a specific diffraction order as long as

the depth of the grating is small compared to its period.[98] Often the fabrication and replication of such sawtooth or slanted[99] gratings remains challenging.[89] A method to circumvent this is to fabricate multilevel ("stair-case") gratings[100] or to use "pulse width modulated"[101,102] or "binary blazed"[103,104] gratings with similar optical properties, see Figure 2.2c. Therefore the continuous permittivity profile of a blazed grating can be decomposed into a Fourier series approximated as a staircase function. These can be used to design a grating divided in subgratings with different parameters, *e.g.* varying duty cycles, overall having a similar permittivity profile and therefore optical property as a geometrically blazed grating.[101]

Most common blazed gratings, used for color generation, enhance diffraction in a preferred order. Generally, this requires a period within the Bragg regime,[86] see Section 2.1.1. In contrast, the periodic nanostructures used in Chapter 3 and 4 have a blazed profile with a subwavelength period. Due to the low periodicity, there is no visible diffraction orders leaking out of these substrates, only zero order transmission is visible. Further, a metallic layer leads to resonant absorption of light, which strongly depends on the incident angle of light due to the underlying blazed profile. A more detailed discussion is given in Chapter 3.3.

Dielectric Subwavelength Gratings

Subwavelength gratings describe structures with periods smaller than the operating wavelength.[105,106] For periods much smaller than the wavelength, the grating behaves like a homogenous material, *c.f.* effective medium theory,[97] with often no observable diffraction. Such structures can be tuned for different purposes such as antireflecting structures,[107] narrow-band filters,[105] polarizing components and phase plates.[108,109] Antireflective surfaces can be designed as surface-relief gratings (*e.g.* triangular)[110] to accommodate step-wise to the refractive index of the two surrounding materials,[107,111,112] similar to the naturally existing "moth eye".[113] Further, the birefringence of the structures can be utilized for phase plates and polarization components and filters.[108,109] Current research in this field involve the development of thin lenses,[58] spectropolarimeter[114] or wave controllers.[54] Due to this "artifical" control of light and the specific design of the nanostructures, such research is often related to the field of metamaterials.[47] Finally, subwavelength gratings can be used for guided-mode resonant filters.[115,116] The fabrication of subwavelength gratings in the visible range requires sophisticated fabrication techniques, which became readily available in the past few decades.[106] Besides, the research on geometrically more complex structures was accompanied by the development of appropriate modeling tools,[105] *e.g.* rigorous coupled-wave analysis (see Chapter 2.3.3).[110]

The dielectric subwavelength structures used throughout the thesis (Chapter 3 - 6) have similarities to above mentioned ones. Similar to guided-mode resonant filters, light shows an in-plane propagation (Chapter 3, 4). Besides, the birefrigent property of gratings is exploited for high contrast filters (Chapter 5, 6). But compared to before mentioned examples, the usage of metal and the corresponding plasmon resonances, strongly supports or even enables the proposed optical effect. Examples based on plasmonics are given in Chapter 2.2.1.

Grating Anomalies

The reflection or transmission spectra of gratings can show rapid variations in intensity at certain wavelengths.[17] Such so-called Wood anomalies can be classified into two distinct types. Type (1) is related to the disappearance of a diffracted order, while type (2) is related to a resonance phenomena. Both will be discussed in the following.

(1) The first type of anomaly refers to the disappearance of a higher order diffraction order. There, a diffracted order changes from evanescent to propagating.[117,118] This leads to an abrupt redistribution of energy.[87] This type of anomaly, we refer to as Wood Rayleigh anomaly (WR) can occur for periodic dielectric[119] or metallic scatters.[17] The WR can be generally described at the spectral position where a diffracted mode propagates tangentially to the grating surface (into the plane of the grating). This occurs when $\sin \theta_m = \pm 1$ (see grating equation 2.1). Hence, for a grating with period p, light at an incidence angle of θ' with wavelength λ'_R

$$m\lambda'_R = p(1 \pm \sin(\theta'))$$
(2.3)

passes off in the mth order.[18] In this case the grating is surrounded by air towards the incident beam.[117]

If the grating is "embedded" (surrounded) with another material than air, *i.e.* the refractive index $n_{surr} \neq 1$, the formula from above still is valid, but λ' and θ' are within the surrounding material. To formulate the position of the WR for light incident from air onto the embedded structure, we have to do following substitutions $\lambda'_R = \lambda_R/n_{surr}$ and $\sin(\theta') = \sin\theta/n_{surr}$. This leads to following equation:

$$m\lambda_R = p(n_{surr} \pm \sin(\theta))$$
(2.4)

where light with wavelength λ_R (in air) passes off in the mth order.[19] With an incident angle θ (in air) and a period p. The order m indicates the diffraction order, while the sign indicates the direction of the mode passing off.[19]

(2) The other type of anomaly is caused by a resonance phenomena.[117] One of the most well-known example is related to surface excitation effects.[120] E.g. a charge density oscillation (*c.f.* plasmons) can be supported at the dielectric metal interface, leading to a decrease of diffraction efficiency of the grating.[87] This can be seen as a propagating "waveguide mode" or "excitation of a surface wave along the grating", for which resonance conditions must be fulfilled (*e.g.* appropriate angle, wavelength or polarization of incident light).[117,121] Apart from metallic gratings, they can also occur in dielectric periodic structures, *e.g.* such as in waveguide couplers or photonic crystals.[119,122–125]

The two types of resonances may occur separated or almost overlapping, depending on the type of structure.[117] Interaction of these two types of anomalies can be observed as Fano-like line shapes,[22] including a sharp change in intensity (*e.g.* see Chapter 3 and 4). While later can be well described by the formalism developed by Rayleigh (first type of anomaly),[18] the embracing Fano-like line shape indicates the co-existence of both anomalies. More information is given in Chapter 3.2.3.

a)   b)   c)
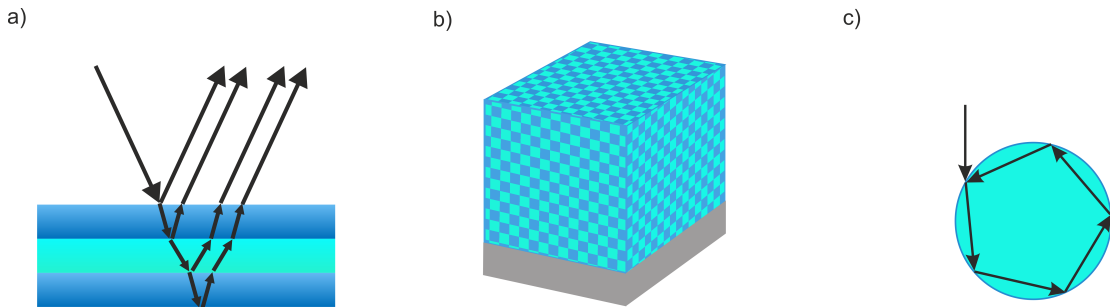
Figure 2.3 – Scheme of a (a) multilayer structure, (b) photonic crystal and (c) dielectric nanoparticle.

2.1.2 Thin Films and Multilayers

One of the simplest structural color effects is caused by thin film interference. It occurs when light is reflected by the upper and lower boundary of a thin film. Depending on the thickness and effective refractive index of the thin film, the reflected light can interfere constructively or destructively, leading to either high reflection or transmission, respectively.[3,86] The interference condition also depends on the refractive indices of the enclosing layers, the incident wavelength and the angle of incidence.[5] A high reflectivity of the layers can form standing waves, so-called Fabry-Pérot resonances.[3] Some of the most prominent examples are the iridescent colors of soap-bubbles or oil films.[126] A stack of alternating dielectric thin films with distinct refractive indices,

see Figure 2.3a, can narrow the resonance condition. Such multilayers enable high quality filters or mirrors,[127] which are commercially available, or can be used for anti-reflective coatings.[128] Since the interference effect depends on the optical path length, the spectral response strongly changes with the incident angle. Recently, a higher angle-stability was achieved by structures similar to the *Morpho butterfly*,[9] or by using highly absorbing dielectric coatings on metal substrates.[126,129]

2.1.3   Photonic Crystals

The concept of photonic crystals can be seen as the generalization of dielectric multilayers, by basically treating an infinite number of periodically arranged elements.[130] Here the propagation of photons through the photonic crystal can be treated similar to the propagation of electrons in a semiconductor crystal.[16] Hence, by solving the Maxwell's equations the optical modes can be determined. Consequently, it is possible to obtain a frequency range for which the propagation of light is forbidden inside the photonic crystal. This frequency range is called "photonic bandgap".[131,132] Photonic crystals can be 1 to 3 dimensional, in increasing order of the fabrication complexity.[133] A representative scheme of a 3D photonic crystal is depicted in Figure 2.3b. Naturally occurring photonic crystals, such as *e.g.* opals, have been an inspiration for research.[130,134]

2.1.4   Nanowires and Nanoparticles

Appropriate tuning of shape and dimensions of dielectric nanostructures, *e.g.* nanowires, allows resonant interaction with light. Light is trapped within the "cylindrical cavity-antenna" leading to radius-dependent mode excitations and subsequent scattering of light at the resonant wavelengths by the individual nanowires,[135,136] see Figure 2.3c. This can be related to Mie resonances or whispering-gallery modes.[75,137] Resonating dielectric nanoparticles can offer an interplay between electric and magnetic resonances, increasing the order of tunability.[138]

2.2   Plasmonic Color Substrates

Here I will give an overview of the most prominent plasmonic color substrates, briefly describing the main physical effects and optical properties. This includes mainly lithographically patterned periodic structures; plasmonic nanoparticles will be mentioned in Section 2.2.8. The following discussion will be limited to the visible range. For other spectral ranges, similar concepts could

be applied, whereas the plasmonic materials or structures need to be changed accordingly. More details about the occurring resonant effects can be found in the given references, the subsequent chapters or other review papers on plasmonic color generation.[74,75,139–141]

The plasmonic structures can be categorized in different ways; depending on the optical effect, the underlying resonances or the geometry of the structure. Other important parameters include the possible color range and contrast, the up-scalability (large-scale fabrication), the spatial resolution (dimensional confinement), the viewing angle stability, the polarization dependency and mode of operation (transmission/ reflection). In the following I will categorize the plasmonic colors by the structural geometry, see Figure 2.4. Often the structure itself defines the present resonances and possible color generation. The structures consist of one (Figure 2.4a-c) or two (d-f) functional metallic layers, which are often used in transmission (a-e) or reflection (a, d-f) mode, respectively. A higher structural symmetry (in dimensions) decreases the polarization sensitivity (top to bottom). By trend, the fabrication complexity increases from 1D periodic structures with one metal layer to 2D periodic structures with two metal layers (from top left to bottom right). Ultimately, these properties strongly affect the suitable field of use; geometrically related structures are often used for similar applications. Examples include anti-counterfeiting (Figure 2.4a, b, d-f), polarization sensitive display technologies (a, b, d, and e) or polarization-independent filters for complementary metal-oxide-semiconductor (CMOS) applications (c). A more detailed overview of such properties is given in Table 2.1. Most of the presented structures utilize aluminum or silver due to the abundance and low cost of these materials, whereas first realizations were made with gold.[46] More details about plasmonic materials are given in Section 2.3.4.

Alternatively, the evolution of plasmonic color substrates can be put into its historical context. Grating structures (1D periodic) are used since decades for optical effects, forming an important backbone of the photonic industry.[118] Novel fabrication techniques enable manufacturing of such structures with feature sizes far below the wavelength[84,142] preventing diffractive effects in the visible. In contrast, metallic layers at this length scale can show localized surface plasmon resonances (LSPR) leading to color generation. A representative comparison is given in Figure 2.1.

2.2.1 Subwavelength Gratings

Metallic subwavelength gratings are periodic structures with alternating dielectric and metallic layers, see Figure 2.4a. Here I only refer to 1D periodic structures,[76,125,143–151] which are in-
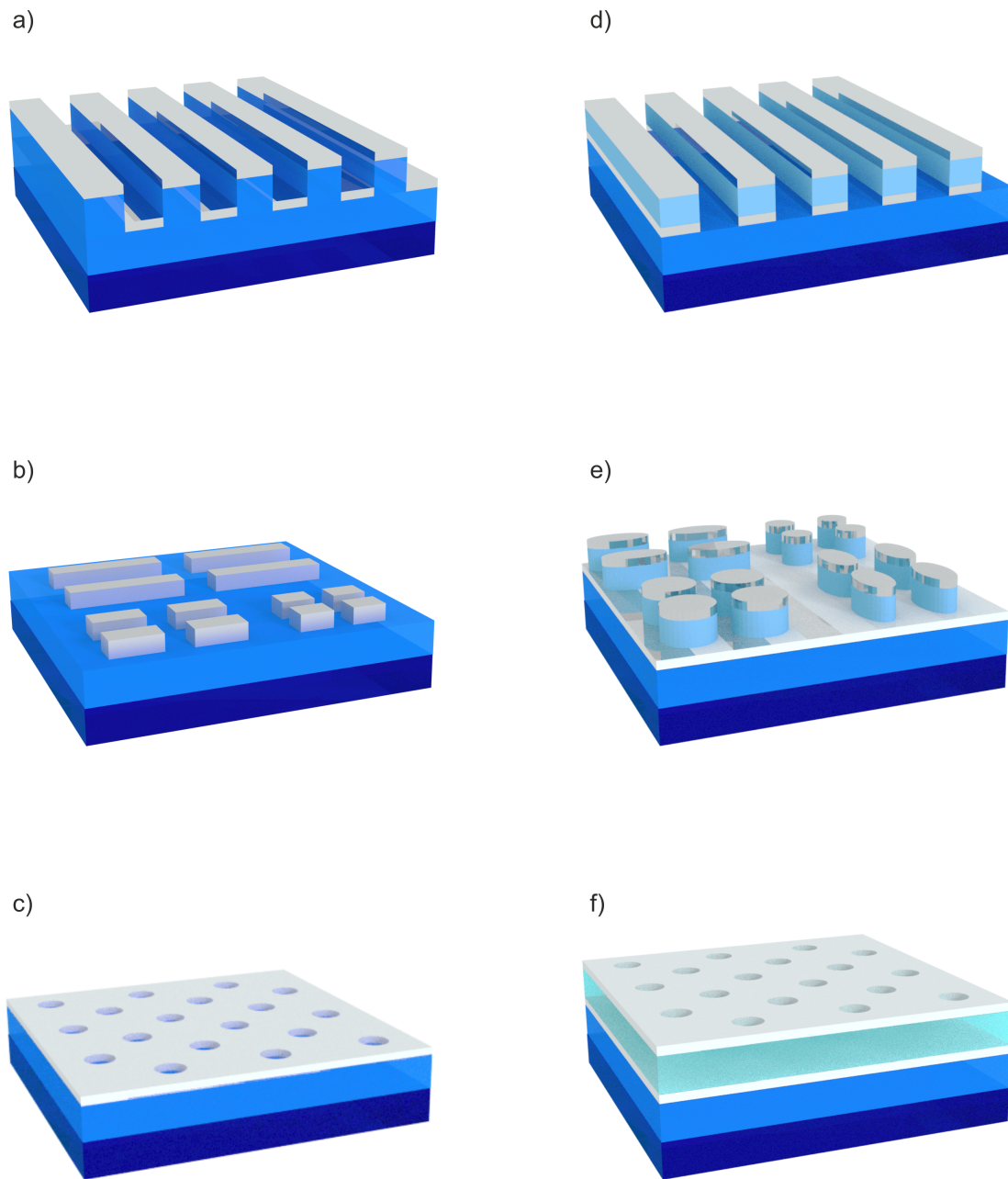
Figure 2.4 – This image depicts schematically the most typical types of periodic plasmonic nanostructures used for color generation. This includes (a) subwavelength gratings, (b) nanoantenna arrays, (c) aperture arrays, (d) MIM gratings, (e) antenna backreflectors and (f) aperture backreflectors. White: metal, dark blue: carrier, *e.g.* glass, light blue: dielectric substrate, pale blue (d-f): other dielectric material. The dimensions (width, length) of the features are ∼ 50-300 nm, the thickness of metal can be between ∼ 5 nm and several mm's (reflector).

Table 2.1 – Overview of properties of different structural colors, see Figure 2.4.

Structural Design*	Physical effects[1]	Properties (+pros/ -cons)	Mode of operation[2]	Polarization-sensitivity	Viewing-angle dependence	Spatial resolution	Fabrication[3]	Applications[4]	References[5]
subwavelength gratings	LSPR, diff., FP	+vivid (diff.+LSPR) -low geo. tunability	R,T	strickly	dep. on p	limited	NIL EBL, LIL	OptSec, pol., CMOS displ.	76,125,143–151 asym.:79,152
nano-antennas	LSPR, diff.	+active tunability +vivid (diff.+LSPR) -low coverage	rather T R (low)	both	random → indep.	high	EBL	display CMOS pol.	153–158 random:159
aperture arrays	EOT, SPP, LSPR	+good filter -tunability	mostly T	seldom	possible	high	EBL, FIB	CMOS, DatSto, imaging	cross:160 Ag:23,161,162 Al:163–171
MIM gratings	MIMR phot. mode SPP	+active tunability -fabrication	R,T	strictly	possible	limited	NIL, FIB	OptSec, displ., imaging	80,172,173
antenna backreflectors	MIMR, LSPR, EOT	+high resolution +high control -saturation	mostly R	possible	dep. on p	high	EBL	OptSec, DatSto	46,174–177 asym.:178,179 MIM:180–183 MIM asy.184
hole backreflectors	MIMR, SPP, el. dipole	+perfect absorption -fabrication -saturation	R	no	yes	high	FIB	OptSec, DatSto	185,186

* An overview of the different structural designs can be seen in Figure 2.4.

[1] LSPR: Localized surface plasmon resonance, SPP: Surface plasmon polariton, MIMR: metal-insulator-metal resonance, EOT: extraordinary optical transmission, diff.: diffraction, FP: Fabry-Pérot, phot. mode: photonic mode, el. dipole: electric dipole

[2] R: Reflection, T: Transmission,

[3] EBL: Electron–beam lithography, FIB: Focused ion beam lithography, NIL: Nanoimprint lithography, LIL: laser interference lithography

[4] OptSec: Optical security, CMOS: Complementary metal–oxide–semiconductor, disp.: Display, pol.: polarizers, DatSto: Data storage

[5] Ag: silver, Al: aluminum, asym.: asymmetric, cross: cross like structures

This table makes no claim to completeness but is instead intended to give a trend of the field by providing some examples.

trinsically polarization-sensitive for direct use as wire grid polarizers.[145] 2D periodic structures are addressed in Section 2.2.5 (antenna backreflectors). Furthermore, metallic subwavelength gratings are often strongly related to diffractive gratings (see chapter 2.1.1). Depending on the period, metallic subwavelength gratings are dominated by diffractive (*e.g.* period of 440 nm)[118,152] or plasmonic effects (*e.g.* period of 180 nm)[75,148] or combinations thereof.[24,150] Arising from the experiments performed by Wood[17] (see Chapter 2.1.1), considerable work was done within this field to use metallic gratings to control the optical properties of reflected or transmitted light. In particular, such gratings have been designed to study and exploit the Wood anomaly,[125,143,144] surface polaritons[187] or to couple electronic to photonic modes,[125,146] more information see Chapter 2.1.1. An overview of surface plasmons on gratings and diffractive gratings with the corresponding fabrication techniques is given by *H. Raether*[188] and *E. G. Loewen* and *E. Popov*,[118] respectively. Research based mainly on pure dielectric subwavelength gratings is given in Chapter 2.1.1. Appropriate tuning of the period can lead to angle-independent optical properties.[148] Deposition of a metallic layer on top of the grating under a certain angle leads to a geometrical asymmetry, rendering distinct optical appearances depending on the direction of observation.[79,152] Such easily recognizable features can be highly attractive for optical security applications.[90] One of the main strengths of subwavelength gratings is their ease of fabrication. Replication of a master structure and subsequent metal evaporation can be sufficient.[79,150–152] This makes them very attractive for a wide range of industrial applications.[81]

2.2.2 Nanoantenna Arrays

A nanoantenna array is often a periodic arrangement of metallic patches or disks exhibiting localized surface plasmon resonances (LSPR), which can be used in transmission[153–158] or sometimes in reflection,[159] see Figure 2.4b. Nanoantennas can be designed to be polarization-sensitive, by distinct dimension (*e.g.* length and width), rendering high chromaticity.[153–155] In particular this is interesting for *e.g.* polarimeter[153] and display applications.[154] Symmetric structures lead to polarization-insensitive filtering.[156–159] A random distribution of nanodisks can lead to angle-insensitive filtering properties,[158] which generally is not assured in the other cases. Such structures are often fabricated with electron-beam lithography (EBL) and subsequent lift-off, limited to small scale and high cost.

2.2.3 Aperture Arrays

An aperture array is a metal film pierced with apertures (holes) where light can pass through, see Figure 2.4c. The optical effect will be referred to extraordinary optical transmission (EOT).[23] In contrast to the previous structures, aperture arrays do not "subtract" light at the resonance, but rather allow light to propagate through the aperture at the resonance.[161] This makes them highly attractive for CMOS applications,[163,166,169,170] similar to RGB (red green blue) filters. Therefore, most of the recent research on aperture arrays is focused on the use of CMOS compatible materials, such as aluminum, and the optimization of the filters towards camera applications.[163–165,167,168,171] Besides these mostly polarization-insensitive hole arrays, angle-independent and symmetric[162] or asymmetric[160] cross-apertures have been designed. The role of Wood anomalies has also been studied in cylindric holes in a chromium layer.[189] Fabrication often includes EBL or focused ion beam (FIB), which generally limit the up-scalability.

2.2.4 MIM Gratings

MIM gratings are structures consisting of metal-insulator-metal (MIM) stacks, see Figure 2.4d. They support resonant modes at the metallic-insulator interface or between the interfaces,[172] which will be referred to MIM resonances. The structural confinement and interaction of such modes enable well-defined, polarization-dependent resonances. The spectral position of the resonances can be tuned by various geometrical parameters such as the period,[173] duty cycle or thickness of insulator,[172] but also the refractive index of the dielectric.[172] The filtering structures can act as a polarizers, potentially to be used for displays.[173] Reflective substrates are often used for anti-counterfeiting applications.[80] Depending on the period, MIM gratings are sensitive to the viewing angle. Up-scalability of the fabrication depends on the complexity of the structures.

2.2.5 Antenna Backreflectors

Antenna backreflector structures are composed of dielectric posts holding a resonant antenna structure above a backreflector, see Figure 2.4e. The backreflector can either be a continuous metal film (MIM like structure)[180,181,183,184] or a layer with apertures (located below antenna structure).[46,174–179] Antenna backreflector structures belong to the most prominent types for color generation.[46] Besides their high spatial resolution, beyond 100'000 dots per inch (dpi),[46,182] they can have a wide range of resonances covering the entire visible range. Often these structures are fabricated with EBL,[46] limiting the up-scalability, but also replication of a master

structure[177] and laser printing of plasmonic aluminum nanodisks[182] have been demonstrated. Besides the more common symmetric and polarization-insensitive nanodisks,[46] polarization sensitive ellipses[179] or nanorods[178,184] have been developed. Controlling the polarization allows "plasmonic hologram" generation.[179,184] Due to the metallic backreflector most substrates are working in reflection. A wide range of materials including gold, silver and aluminum are used. The plasmonic material often defines the dimensions and periods required for visible color filtering. In reverse, these parameters define the dependency of the optical effect on the viewing angle.

2.2.6 Aperture Backreflectors

Instead of placing antennas over a uniform backreflector (as in Figure 2.4e), an aperture structure can be used instead, see Figure 2.4f. This can lead to nearly "perfect light absorption" enabled by a high broadband reflectivity with nearly "unity absorption" at the resonance.[185,186] Such structures are supposed to show high spatial resolution and angle-insensitive light absorption.[185] This could make them a valuable tool for optical security or data storage applications. To date, fabrication is done by FIB.

2.2.7 Other Lithographically Defined Structures

Besides the described structures of Figure 2.4 alternative structures exist; Plasmonic colors can be formed by patterning pure metallic surfaces *via* EBL or FIB.[190–195] They can have similar color generating properties as the structures mentioned before (Figure 2.1a-f), but due to the pure metallic structure they are more suited for coloration of coins[194] and other metal finishes.[195] Because of the generally high broadband reflection of metals, it remains challenging to fabricate high contrast colors though.[195] "Resistless nanoimprint" in metal could be used for up-scaling.[196] Furthermore, protection of the metal against, *e.g.* oxidation has to be considered. Annular apertures made out of gold show tunable transmission depending on the gap width.[197] Patterned amorphous silicon on aluminum allows angle-insensitive reflection of light, tunable *via* the period and width of the silicon.[198] The use of "conjugate twin-phase modulation" and a plasmonic absorber allows generation of vivid and reversible colors.[199]

2.2.8 Colloidal Nanocrystals

Colloidal nanocrystals can be described as inorganic, solution-grown, nanometer-sized particles, which are stabilized by surfactants attached to their surface.[200] In contrast to most other present plasmonic structures, colloidal nanocrystals are fabricated by bottom-up approach through wet-chemical synthesis, enabling high-throughput production of complex, three-dimensional color generating nanostructures.[74] A wide range of gold, silver and aluminum nanoparticles in various shapes[201–203] and more recently core-shell,[204] branched[205] or bimetallic nanostructures[206] have been investigated. Generally, they enable a very sensitive resonance tunability (*via* size, geometry, material or synthesis) over the complete visible range. "Dewetting" of metal films into nanoparticles at high temperature can sensitively define their shape and resonance condition.[207] Moreover, it was demonstrated that gold-silica nanocups with a geometrical asymmetry show angle- and spectral-dependent scattering properties.[208] Recently, silver nanocubes were developed, which form perfect absorbers in the visible and near-infrared, when placed on a metal surface with a dielectric spacer.[60] Although colloidal nanoparticles offer a wide range of possibilities, incorporation in solid-state devices as well as a precise placement at the nanoscale remains challenging.[209] Recent approaches guide the nanoparticles to certain locations for further self-assembly[209,210] or attach them to macrostructures, *e.g.* DNA strands.[211,212] The colored glass windows of churches are representations of such nanoparticles,[12] which also nicely illustrate the durability of plasmonic color substrates.[75]

2.3 Design & Fabrication of Plasmonic Structures

This section gives a brief overview of the state-of-the-art of fabrication methods as well as the fabrication process used at CSEM. It also briefly compares some simulation tools to model plasmonic substrates and different plasmonic materials.

2.3.1 State-of-the-art Fabrication Methods

In the past years the fabrication of nanostructures has greatly evolved in terms of resolution, availability and cost.[85] The quality of the nanostructures strongly defines the "purity" and strength of the plasmon resonance, therefore best practice fabrication conditions are essential.[213] There are several review articles about nanofabrication.[84,142,214] Here I will focus on some advancements with respect to large-area and low cost.

Besides serial writing of master structures with electron-beam lithography (EBL) or focused

ion beam lithography (FIB), laser interference lithography (LIL) has been demonstrated as versatile and adaptive method for parallel fabrication of high quality nanostructures on a large area.[163,215–219] Nanoimprint lithography (NIL) turned out to be a powerful method for high throughput patterning.[220,221] Furthermore, template stripping of metals can be used to obtain "ultrasmooth" metal surfaces,[222–224] which was recently also integrated into roll-to-roll processes.[225] Finally, the roll-to-roll techniques for nanofabrication were improved in replication area and throughput.[226,227] Other recent developments include transfer printing onto flexible polymers,[228,229] direct laser writing lithography,[230,231] colloidal nanolithography,[232] direct imprint of metal structures,[196,233–235] laser printing of metallic nanostructures[182,236,237] or inkjet printing.[238–241]

2.3.2 Fabrication Process at CSEM

To realize applications based on plasmonic substrates, it is essential to rely on fabrication tools which are large-scale, cost-efficient and viable in an industrial environment. To be cost-efficient, it should be assured that a high number of replications can be achieved by utilizing the same complex master structure, *e.g.* more than $500'000$ replications demonstrated by CSEM[i]. To that end, simple structures can be combined into a complex one. This procedure clearly differs from the commonly used EBL technique; a complex combination of structures can be created directly during a single writing process. But creating a new or a copy of the pattern generally requires the re-use of EBL.

Figure 2.5 shows a general process flow for the fabrication of plasmonic substrates used in this thesis, which is in-line with industrial large-scale manufacturing. First, the properties of the structure and optical effect have to be modeled (see Section 2.3.3). Then, a periodic structure has to be created by a large-scale process. Therefore, laser interference lithography is an ideal candidate, more details see Chapter 3. Homogeneous subwavelength structures with a seamless surface of $1 \; m^2$ or more can be fabricated (*e.g.* Temicon[ii]). Nowadays some photonic companies offer a selection of cost-efficient pre-patterned e-beam substrates (*e.g.* Philips[iii]). Either way the periodic photoresist pattern has to be transferred into the underlying substrate. Depending on the geometry, appropriate tuning of a protective layer (*e.g.* chromium) or the etching parameters can be utilized to tune the shape and depth of the transferred pattern. A negative copy of the structure in nickel can be grown by a galvanic process. A nickel master is flexible, ensuring a

---

[i]`http://www.csem.ch`, accessed 17.11.2016

[ii]see `http://www.temicon.com/en/`, accessed 17.11.2016

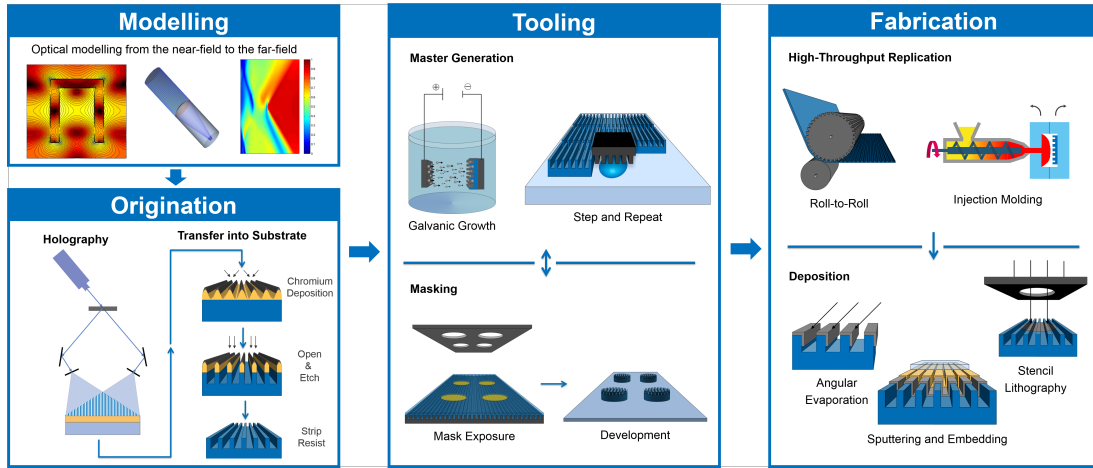[iii]see `http://www.innovationservices.philips.com`, accessed 17.11.2016

Figure 2.5 – This scheme gives an overview of the required steps for the fabrication of plasmonic structures, as used throughout the thesis.[242] It consists of the modeling of the structure (top left), the origination of a master structure with holography (bottom left), the fabrication of a nickel shim master (optionally with masking) and replication of the nickel shim (middle), an optional high-throughput replication (for large-scale production) followed by the modification of the structure with metal and dielectric (right).

simplified and secure demolding process, while being relatively hard and durable. Replication itself can be done by hot embossing or UV molding, which are both standard in industry. A more complex master structure can be created by combining distinct periodic master structures with the use of photomasks (see Figure 2.5 middle). The area of the master structure can be increased by repetitive replications of a small structure in a step-and-repeat process. A subsequently grown nickel shim can be wrapped around a roll for roll-to-roll manufacturing. Alternatively, it can be used as an insert tool for injection molding. Roll-to-roll and injection molding allow the fabrication of a large quantity at high speed.[243] Physical vapour deposition of metal can lead to individual and well-defined plasmonic nanostructures. Alternatively, sputtering can be utilized for homogeneous plasmonic films. Stencil lithography or patterned photoresist can be used to deposit metal only on certain parts of the structure. Such processes can be valuable, but due to the additional fabrication step, they are more expensive and increase the complexity of manufacturing. Finally, the plasmonic substrate can be embedded with a polymer or sol-gel to protect it against abrasion or oxidation and prevent reverse engineering.

The presented process is the basis for the fabrication of the plasmonic substrates (samples including plasmonic structures) throughout the thesis. Details about the individual fabrication parameters are given in the corresponding chapters.
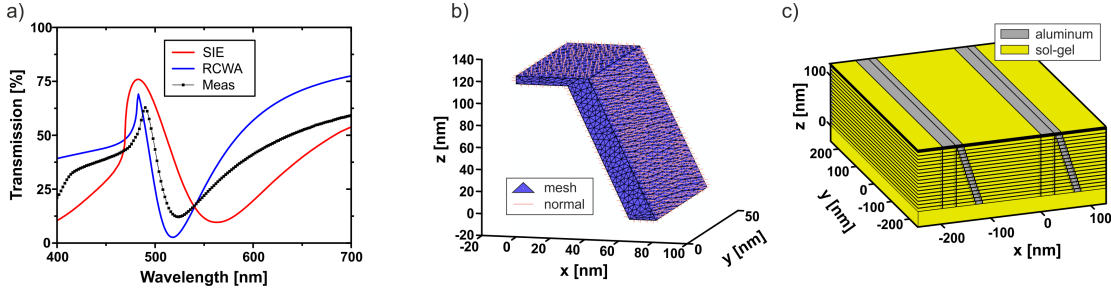
Figure 2.6 – (a) Transmission spectra calculated with SIE and RCWA and compared to the measurement. (b) Mesh of a single structure consisting out of triangles used for the calculation with SIE. (c) Corresponding periodic structure sliced in layers for RCWA.

2.3.3 Numerical Simulations

Appropriate numerical simulation tools are essential for the research and development in the field of nanophotonics. They are used to predict optical behavior of certain structures or to evaluate optimal geometric parameters for desired optical properties. Most problems in the field of plasmonic structural colors can be solved numerically by discretizing the Maxwell's equation. [244] The solution can give information about the optical far-field and near-field; *e.g.* the transmission, reflection, absorption, diffractive orders, phase or near-field enhancement. The differential method utilizes a differential form of the Maxwell's equation. The most popular representative of this method is the finite differences in time domain (FDTD). [245,246] It discretized the Maxwell's equation in time and space using finite differences. [244] As a result, the electromagnetic field can be computed at all time in space. Besides the large variety of problems, which can be solved by FDTD, it has limitations for solving periodic systems. [244] Another popular differential method is finite elements (FEM). [247] Surface integral equation method (SIE) solves the Maxwell's equation in integral form *via* transformation with the Green's function. [248,249] Discretization can be be done on the nanostructure itself, more specifically on the surface boundaries of a piecewise homogeneous material. [244] SIE is a very versatile method since it can solve the far- and near-field of individual or periodic structures. Unfortunately, both FDTD and SIE require significant computation time and memory. Rigorous coupled wave analysis (RCWA) is an alternative method, which is highly efficient to calculate the optical properties of the far-field. The Fourier-space method obtains the solution by "analyzing the diffraction of an electromagnetic wave" incident on a periodic structure. [110,250] The structure itself has to be built up as staircase approximation. More details about the simulation methods can be found in Gallinet *et al.* [244]

Figure 2.6a shows a far-field transmission spectra of the plasmonic structure given in Chapter 3, see Figure 3.2. The measurement is compared to the simulation performed with SIE

and RCWA. The corresponding mesh and layered structure, respectively, which were used for the simulations are given in Figure 2.6b,c. Whereas the simulations show a similar spectral shape as the measurement, it can be observed that there is a certain mismatch between the simulation methods. This could be caused by the different solving algorithm of the approximative simulation tools. Finally, it is important to note that structures are never fabricated as perfect as assumed in the model (*e.g.* non-perfect edges, roughness). In the following chapters, I will use RCWA and SIE to model the optical properties (RCWA: far-field, SIE: near-field, far-field, phase) of the plasmonic nanostructures.

2.3.4 Plasmonic Materials

Plasmons are described as the collective oscillations of free electron gas. This requires a negative real dielectric constant of the material. According to the Drude model, this is satisfied if the plasma frequency of the material is higher than the operation frequency.[251] This reduces the suitable materials mostly to metals; typically the noble metals gold, silver and copper but also aluminum and magnesium can be used. The strength of polarization induced by an external electric field is described by the real part of the dielectric constant, while the optical losses present in the material are related to the imaginary part.[252] Losses are associated with interband transitions (occurring at high frequencies), lattice vibrations or the scattering of conduction electrons by defects.[251,253] The scattering induced losses can be reduced by improving the quality (*e.g.* smoothness) of the plasmonic structure.[213] The other losses are intrinsic properties of the plasmonic material, which can not be avoided.[253] To improve the optical properties, currently there is great interest in alternative plasmonic materials such as metallic alloys (*e.g.* Au-Cd), semiconductors (*e.g.* ITO), transition metal nitrides (*e.g.* TiN) and graphene.[70,251,254,255] In contrast, such loss mechanism and the associated heating of the structures could be exploited for appropriate applications, *e.g.* heat assisted magnetic recording.[256] Until now, the most utilized plasmonic materials are gold and silver due to their low losses. Especially its chemical stability made gold the material of choice for biological applications. Silver as well as aluminum oxidize rapidly in ambient conditions. While aluminum forms a self-protecting oxide layer,[257] silver has to be embedded in a material to avoid further oxidation.[255] From a practical point-of-view, gold is too expensive for many applications. Aluminum is one of the most abundant materials, making it suitable for cost-efficient applications.[258] Currently there is great interest in CMOS compatible,[259] refractory,[260,261] phase change[262] or hydride materials.[263]

3 Color Rendering Plasmonic Aluminum Substrates with Angular Symmetry Breaking
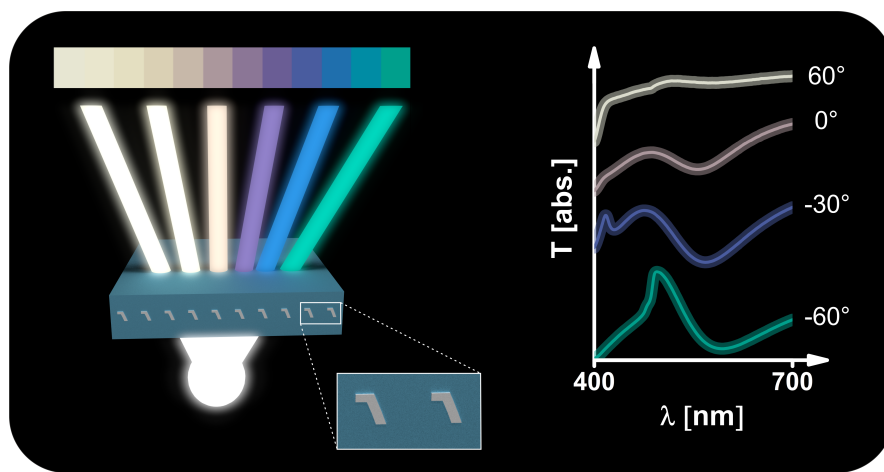
I fabricated and characterized large-area plasmonic substrates that feature asymmetric periodic nanostructures made of aluminum. Strong coupling between localized and propagating surface plasmon resonances leads to characteristic Fano line shapes with tunable spectral positions and widths. Distinctive colors spanning the entire visible spectrum are generated by tuning the system parameters, such as the period and the length of the aluminum structures. Moreover, the asymmetry of the aluminum structures gives rise to a color rendering effect with strong symmetry breaking; colors are observed only from one side of the surface normal. Using a combination of immersed laser interference lithography and nanoimprint lithography, the color rendering structures can be fabricated on areas many inches in size. I foresee applications in anticounterfeiting, photovoltaics, sensing, displays, and optical security.

This chapter is "adapted with permission from L. Duempelmann, D. Casari, A. Luu-Dinh, B. Gallinet, & L. Novotny; Color Rendering Plasmonic Aluminum Substrates with Angular Symmetry Breaking. *ACS Nano* **9** (12), 12383–12391 (2015). Copyright 2016 American Chemical Society."

3.1   Introduction

Research in the field of plasmonic color substrates has often emphasized angle stable color generation, often differing from diffractive effects;[46,155,173,174,177,264] Angle-dependent and iridescent color effects are often undesired, thus avoided with appropriate design.[148,265] While some applications, *e.g.* display or cameras, require such angle-independent optical effects,[154,266] other's utilize strong color rendering only for predefined observation directions.[81,267,268] Here, I demonstrate a strong symmetry broken color rendering effect, for which a plasmonic sample generates colors only when viewed from one side of the surface normal. Such kind of optical effects can be easily checked by a non-trained user without special equipment, therefore is strongly desired in optical security applications.[79,81,268] Furthermore such structures can be incorporated in bulk material, preventing easy replication of the structure.[90,269]

To date, most of the color rendering substrates have been fabricated using gold or silver, mostly because of their high plasma frequency and low losses,[46,76,180,270] but the high cost of these noble metals hinders the broad integration into practical applications. Aluminum is a versatile alternative (see Section 2.3.4). Although structural colors based on aluminum have been shown recently,[155,174,177,179,264] demonstrations have been made with expensive techniques and are limited to small patterned areas.[214]

Here I develop a color rendering substrate composed of an array of tilted aluminum nanowires that possess a broken symmetry with respect to the surface normal of the substrate. Due to the broken symmetry, the substrate exhibits strong color rendering only in one tilt direction, that is, the substrate looks colorful from one angle of observation whereas it appears colorless from the opposite angle of observation. This distinctive asymmetry originates from the angle-dependence of surface plasmon excitation coupled with the tilted geometry of the nanowires. The interaction of surface plasmons with propagating modes gives rise to distinct spectral resonances. A wide range of the RGB color spectrum is obtained by fine-tuning the fabrication steps. The symmetry breaking, color rendering substrates can be fabricated on a large-scale, with high-throughput and at low cost.

3.2 Results

Fabrication of aluminum plasmonic nanostructures in an up-scalable and cost-effective manner is a key element for sophisticated realization of applications based on plasmonics. In the following a detailed description of the proposed large-scale fabrication method is provided. Further the concept of structural colors permitting angular symmetry breaking effect based on this kind of structures is shown. After in-sights of the physical effects, a concrete realization of the optical effect is provided.

3.2.1 Fabrication Method

The proposed fabrication method is compatible with standard industrial roll-to-roll process[226] and is illustrated in Figure 3.1. It involves immersed laser interference lithography for the fabrication of periodic nanoscale pattern (see Section 2.3.1). These patterns are subsequently used as a template for nanoimprint lithography. Evaporation with aluminum from an oblique angle generates asymmetric plasmonic structures and subsequent embedding with a polymer provides protection and enables the use at ambient conditions. Most of the nanofabrication techniques used in today's research laboratories are either slow or very expensive (*e.g.* serial fabrication methods such as ion beam or e-beam lithography[271,272] for master fabrication or immersed lithography for reproduction in chip technology[273]). Moreover these techniques are often limited to a small area ($\sim$ 100 x 100 μm^2)[46,174,264] or require stitching techniques of the master structure to obtain large-area coverage. Laser interference lithography, on the other hand, is a parallel technique that can cover several square cm's.[216] Additionally the depth and duty cycle of the periodic nanostructures can be tuned during the fabrication process. Unfortunately the fabrication of nanostructures with periods below $\sim$ 250 nm[274] often requires the use of ultraviolet (UV) lasers ($<$ 400 nm) and optics, which are more expensive and difficult to handle. To be in-line with parallel and potentially up-scalable fabrication methods, I use immersed laser interference lithography[275] (Figure 3.1a) in which a prism with high refractive index is placed onto the photoresist covered by an index matching immersion liquid. This technique not only reduces the wavelength by the index of refraction n_{prism}, but it also increases the angle of incidence due to refraction at the prism surfaces (see Figure 3.1a). The formula is given by[275]

$$ p = \frac{\lambda}{2n_{prism}\sin\{\beta - \sin^{-1}(\sin(\beta - \delta)/n_{prism})\}} \qquad , \qquad (3.1) $$

where δ is the incident angle in air (to the normal), β is the prism angle (at the side close

to the sample) and n_{prism} the refractive index of the prism. The period of the pattern caused by the interference of the two beams can be reduced by a factor ~ 2 compared to conventional laser interference lithography,[180,275] *e.g.* a period ~ 160 nm can be obtained with a 441.6 nm laser. In particular negative photoresist was exposed with a 441.6 nm laser at an incident angle $\delta = 30.1°$ onto an equilateral prism ($\beta = 60°$, $n_{prism} = 1.64$). A subsequent development gives rise to a sinusoidal pattern with period $p \sim 197$ nm. Transfer of the periodic pattern into glass is achieved *via* angle evaporation of chromium (as etching stop layer) onto the photoresist and subsequent etching into photoresist and borosilicate glass (Figure 3.1b-d, see also Section 2.3.2). By tuning the process parameters, the period, depth, shape (rectangular or trapezoidal) and duty cycle (ratio of width of the ridge to period) of the resulting nanostructures can be tailored. To further enhance the sustainability of the template a replication in Nickel can be fabricated through a galvanic process.
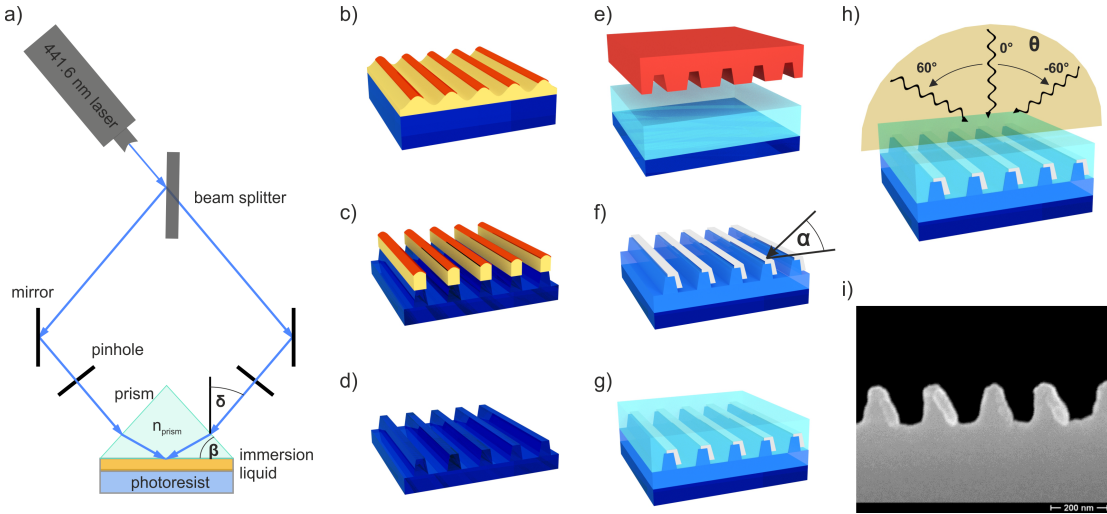

Figure 3.1 – Fabrication scheme including: (a) immersed laser interference lithography, (b) angular evaporation of chromium, etching into (c) the photoresist and the underlying glass substrate to (d) generate the master. (e) Nanoimprint lithography with the master, (f) angular evaporation (at an angle α) of aluminum and (g) subsequent embedding. (h) Measurement conditions with p-polarized light under the angle θ (in air) and (i) SEM image of a fabricated sample prior embedding.

Following the fabrication of a master by immersed laser interference lithography, nanoimprint lithography[84,180,221,226] is used to replicate the periodic nanostructures into a UV curable polymer, see Figure 3.1e. After replication, aluminum is evaporated from a well-defined angle α onto the replicated nanostructures (Figure 3.1f) *via* an electron beam physical vapor deposition process. Hereby the outer layer of aluminum forms a self-protective oxide layer of around 2-3 nm.[257] Simulations show that this oxide layer has a diminishing effect on the optical properties

but can lead to a slight red-shift. Figure 3.1i shows a scanning electron microscope (SEM) image of a fabricated sample. Finally, the samples are embedded in UV curable polymer (Figure 3.1g) to protect the aluminum nanowires against abrasion caused by ambient use. The transmission spectra of the samples were measured on a rotation stage with a photospectrometer. Figure 3.1h shows the transmission of p-polarized light incident at an angle of $-60 < \theta < 60°$ (in air) with respect to the surface normal. Negative angles are those that are in the same direction as the metal evaporation.

3.2.2 Geometrical Influence on the Optical Effect

The evaporation of aluminum from an inclined angle leads to deposition at the slope and the top of the underlying nanostructures, which results in a symmetry broken geometry and gives rise to an optical anisotropy and asymmetry. This subwavelength lamella-like structure has the unique property of being indiscernible among certain angles, directions, respectively. This can not be achieved with in-plane, flat or even bulky structures, showing *e.g.* directional emission,[276] coupler[277] or light scattering.[208] A discussion about different types of structures can be found in Section 2.2. Moreover, its asymmetric tilt geometry shows not only angle- but also direction-dependent excitation efficiencies. The theoretical effect of structural asymmetry has been reported in the literature,[278] whereas mainly variation of the structure and not change of measurement conditions, such as the incident angle, led to a shift of the resonance. Moreover fabrication of such structures would be very challenging. The asymmetrical geometry can also be exploited for enhancing nonlinear effects, such as sum-frequency or second-harmonic generation.[279,280] To optimize the transmission asymmetry I have performed a detailed study of the system parameters. The aluminum layer has been varied in the range of 5-30 nm to ensure high transmission values, while the period has been fixed at 197 nm to minimize diffraction effects in the visible range. I have also varied the evaporation angle, defining the ratio and area of aluminum deposited on the side and the top of the underlying nanostructures. Other parameters are the depth, duty cycle and slope angle of the nanostructures, which can be defined during the fabrication process.

3.2.3 Angle-Dependent Transmission indicating Strong-Coupling

Figure 3.2 shows the transmission spectra of a plasmonic substrate with a certain geometry (will be discussed later) excited by p-polarized light under different incident angles θ. Experimental measurements are compared with simulations done with the rigorous coupled-wave analysis
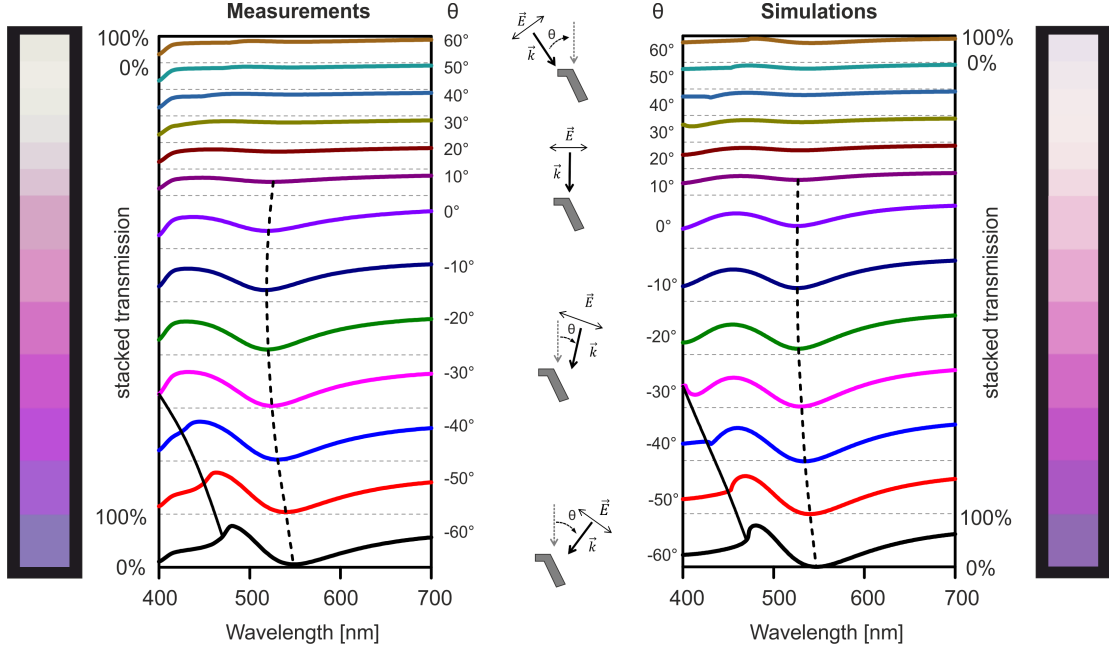
Figure 3.2 – Transmission spectra for different angles of incidence for p-polarized light. Measurements are shown on the left and simulations on the right. The sketches in the middle illustrate the configuration in terms of the electric field E, the wavevector k and the angle θ. The Wood-Rayleigh anomaly (bold line, position adapted to transmission value) and plasmon resonance (dashed, position at minimum) appear at around $-10°$ and shift to the red when increasing the angle to $-60°$ (in air). Observed colors at the corresponding angles are given at the side of the graphs.

(RCWA),[250] see Section 2.3.3. For negative angles a pronounced spectral feature is observed, whereas for positive angles the transmission remains relatively flat. The pronounced spectral features observed at negative angles are the result of two optical effects, the Wood-Rayleigh anomaly (WR) and a localized surface plasmon resonance (LSPR). The Wood-Rayleigh anomaly (bold line Figure 3.2, more details see Chapter 2.1.1) is a spectral signature of a propagating resonance (PR) in a periodic nanostructure and refers to the disappearance of higher-order propagating modes (see Formula 2.4, Chapter 2.1.1). For the +1st order this gives

$$\lambda_R = p(\sin(\theta) + n_{surr}) \qquad , \tag{3.2}$$

where p is the period of the structures, n_{surr} the refractive index of the homogeneous surrounding medium and θ the angle of incidence in air.[17,19] While the angle-dependent excitation of a PR gives rise to enhanced transmission, the excitation of a LSPR leads to a transmission dip. The LSPR depends sensitively on the geometry; the efficiency of excitation is strongly angle-dependent but not the spectral position. At high negative tilt angles strong coupling between the PR and the broad resonant LSPR results in a narrow and dispersive feature char-

acterized by an asymmetric Fano-like line shape.[121,281,282] The individual resonances can not be distinguished anymore. I will refer the resonance induced by the coupled mode as propagating surface plasmon resonance (PSPR). Further information about the coupling are given in Chapter 3.2.7. The coupled resonant system has similarities to selective suppression of transmission or perfectly absorbing structures.[264,283] As an intrinsic property of the plasmon resonance, the PSPR is excited by p-polarized light arising only for angles $\theta < -30°$.

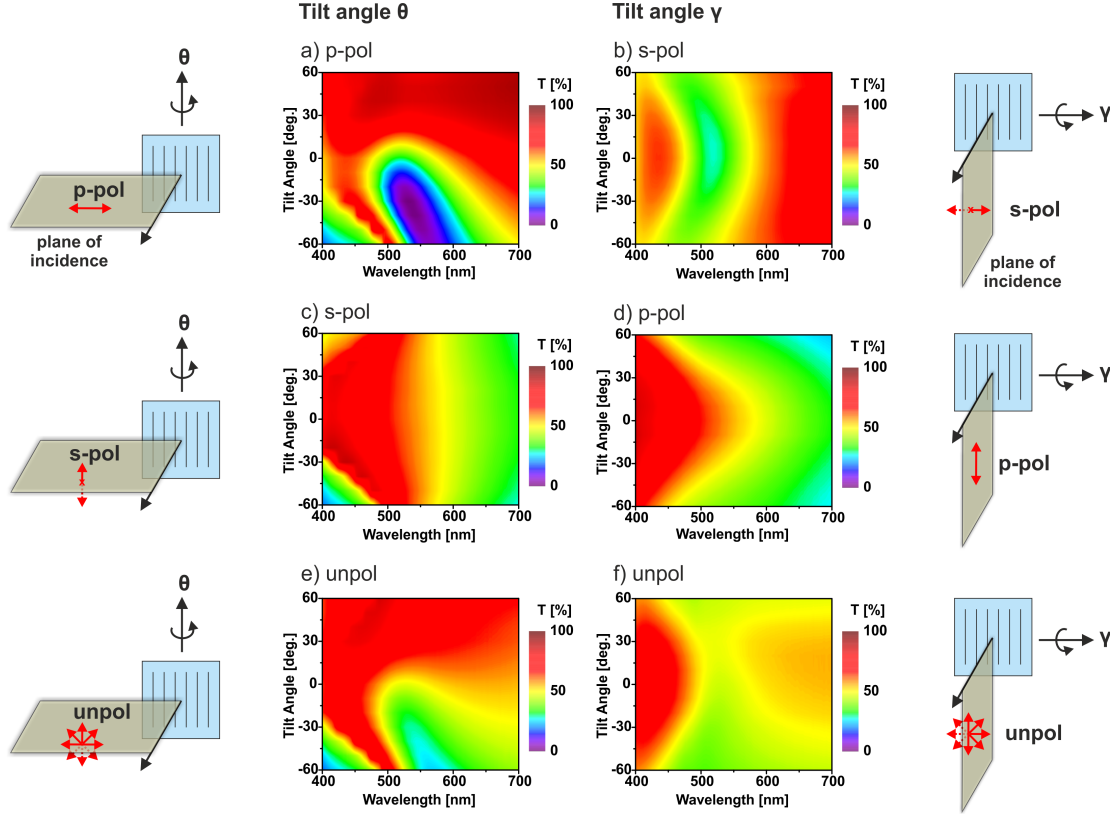**Figure 3.3** – Angular transmission spectra with p-polarized (a,d), s-polarized (b,c) and unpolarized light (e,f) upon the tilt angle θ (perpendicular) and the tilt angle γ (along the periodic nanostructures) respectively are shown. The spectra are normalized to a glass substrate. The schemes next to graphs illustrate the plane of incidence, the tilt angle and polarization.[i]

3.2.4 Polarization and Rotation Dependent Angular Transmission

For further characterization the influence of the polarization and the tilt angle on the optical properties are studied. Figure 3.3 shows the angular transmission spectra of the sample from Figure 3.2 upon p-polarized (Figures 3.3a,d), s-polarized (Figures 3.3b,c) and unpolarized light

---

[i]The illustration of the polarization and angle of Figure 3.3 is similar to the one of Figure 5.3. Here the focus is more on the tilt angle, therefore Figure 3.3 is divided in the angles θ and γ.

(Figures 3.3e,f) among the tilt angle θ and γ of the sample. p-polarized light is within the plane of incidence, s-polarized light is perpendicular to it. Tilting the sample perpendicular to the lines of the nanostructures is indicated by the angle θ, whereas the angle γ describes a tilt along the periodic nanostructures. As before described the plasmons are excited for p-polarized light for a tilted incidence θ perpendicular to the periodic nanostructures (Figure 3.3a). In Figure 3.3c, upon s-polarized light the aluminum nanolamellas show transmission spectra with a maximum following the Wood anomaly, which confirms that no surface plasmons are excited in the nanolamellas. On the other hand tilting the sample along the nanostructures, angle γ, does not show strong optical features. p-polarized (Figure 3.3d) light shows a broadband response of the aluminum nanowires with a slight angle-dependency. Similar for s-polarized light where a high transmission is observed (Figure 3.3b). More importantly, for usage in ambient conditions the proposed optical effect also has to be visible in unpolarized light. Figure 3.3e,f show clearly that the main optical feature, the distinct signature of the plasmons with its asymmetric angle-dependent feature, is so dominant in p-polarized light that it clearly appears also for unpolarized light. This strong angle-induced asymmetry leads to the appearance of a color effect only in one of the four directions even in unpolarized light. An equivalent angle-dependent behavior for the excitation of plasmonic structures has been studied in symmetric system.[81,284,285]
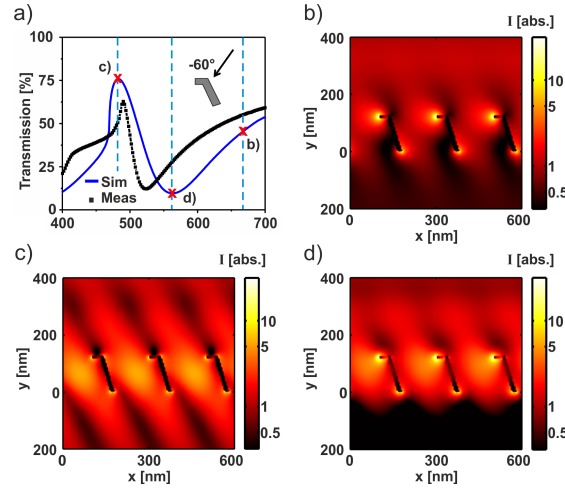
Figure 3.4 – Calculated electric field distributions for an angle of incidence of $\theta = -60°$ (in air). (a) Far-field transmission spectrum calculated (line) and measured (dots). (c) Near-field evaluated at the transmission peak ($\lambda_c = 483$ nm) showing no regions of high intensity. (d) On the other hand, strongly enhanced fields at the tips (up to 72x) and between the nanowires (up to 4x) are observed near the plasmon resonance ($\lambda_d = 562$ nm). (b) For wavelengths beyond the plasmon resonance ($\lambda_b = 675$ nm) strongly enhanced fields are only observed at the extremities of the metal structures.

3.2.5 Near-field Intensity Distribution

To further investigate the physical nature of the PSPR electromagnetic field simulations using the surface integral equation method (SIE)[249] were performed, see Section 2.3.3. Figure 3.4 shows the calculated electric fields for an angle of incidence of $\theta = -60°$. The transmission spectrum shown in Figure 3.4a features a peak of high transmission that is caused by the interference of the incident light with the zeroth and first order diffracted fields. These fields are of nearly equal intensity and mainly show near-field enhancement between nanowires, see Figure 3.4c. The transmission drops for longer wavelengths and reaches a minimum at $\lambda_d = 562$ nm. The strong decrease in transmission is caused by the excitation of LSPRs of individual nanowires, which is associated with strong near-field enhancement at the tips and between the nanowires (Figure 3.4d) leading to an increased in-plane absorption. For even higher wavelengths LSPRs are no longer efficiently excited and the transmission increases again. The field enhancement decreases between the nanowires and at the tips from ~4x to ~1.3x and ~72x to ~61x respectively (Figure 3.4b).

3.2.6 Geometrical Influence on the Resonance

The spectral position of the PSPR (at a given angle) is determined by the geometry of the plasmonic nanostructure (length, tilt and shape) and the duty cycle and period of the underlying nanostructures. The calculated transmission and absorption spectrum for varying period and varying length is shown in Figures 3.5a,b and 3.5c,d respectively. In Figure 3.5a,b the length of the nanowires (126 nm) is fixed, whereas in Figure 3.5c,d I keep the period (197 nm) constant (see also Figure 3.6), each at an angle of incidence of $\theta = -60°$. Regions of low transmission (blue areas) are associated with high absorption or in-plane propagation due to LSPR excitation (up to ~95%), see Figure 3.5b,d. Hence, the incident field is not transmitted nor reflected. With this spectral tunability of the PSPR the complete visible color range can be represented. In particular change of the period shifts the color effect, whereas modification of the length influences the spectral shape and contrast of the color. For increasing period diffractive effects attribute to the total transmission. In that case, an optical color effect could be similar but is no longer a pure zero order effect. This relates to optical effects achieved with diffractive gratings (see Section 2.1.1). The length of the nanowires can be easily tuned *via* the evaporation angle of the metal. The additional evaporation on top of the nanostructures leads to a slight color appearance mainly at normal incident, but can be controlled with the duty cycle of the nanostructures. Figure 3.5e-g show comparisons of theory and experiment for different geometries (length of 74,

126 and 137 nm, width about 15 nm). The agreement between theory and experiment is very good.
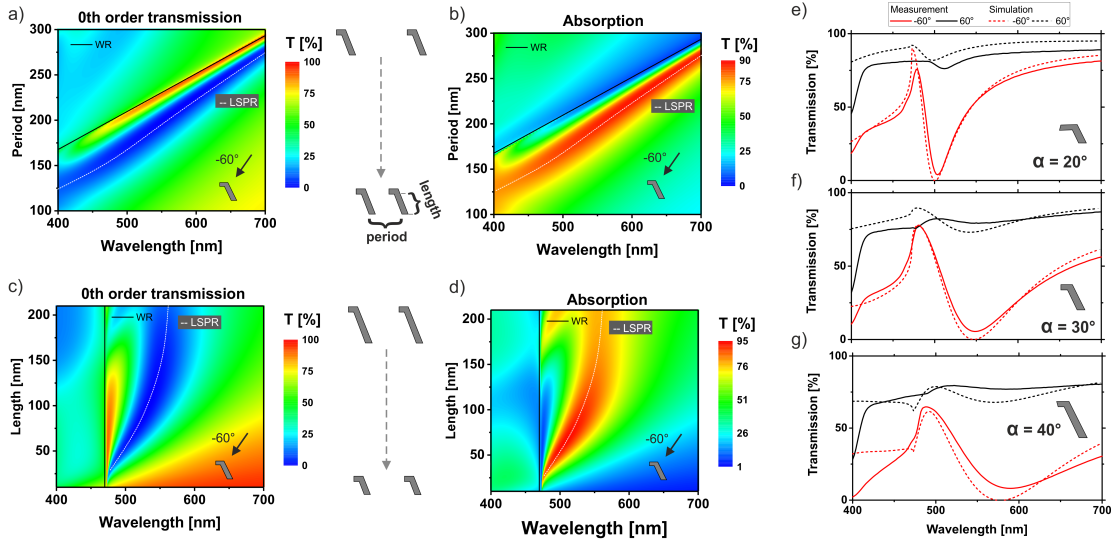

Figure 3.5 – Simulated transmission, absorption spectra as a function of (a,b) period and (c,d) length of the plasmonic structures, respectively. The angle of incidence is $\theta = -60°$. The transmission is lowest where the absorption due to excitation of LSPRs is highest. (e-g) Comparison of theory and experiment for three different structures generated by different evaporation angles (bold). The sketches represent the geometrical differences.

3.2.7 Strong Coupling of Modes

The transmission properties of the plasmonic filter can be described by the interference of the two modes, the diffractive mode characterized by the WR and the localized surface plasmon resonance (LSPR). Such concepts have been shown in similar coupled systems.[146,189,282,286–288] To interact, the modes have to be spectrally and spatially proximate. Classically, such an interaction of modes can be illustrated by two coupled oscillators;[286,288] A conceptual scheme is given in Figure 3.6a. Coupling of the modes leads to the formation of a new coupled mode (bonding and antibonding).[146,287,289] Figure 3.6b is a conceptual figure showing the spectral signature of the original modes without interaction. The spectral position of the pure LSPR (of the periodic array) is mainly governed by the length of the nanostructures (see Figure 3.5). Additionally, an increase of the period would lead to a redshift, because charges of identical signs are further separated. The illustration in Figure 3.6b should highlight that without interaction the modes would spectrally cross each other.[146,286] In contrast, an avoided level crossing of the WR and the LSPR is observed if they strongly couple. This can be seen in Figure 3.6c, where the coupled mode clearly display these anti-crossing characteristics. Such an anti-crossing can

33

be seen as a signature of strong coupling between the WR and the LSPR.[16,286] Overall the position of the PSPR is determined by a maximum in absorption (minimum transmission),[287] which is an indication of the excitation of plasmons.

The strength of mode coupling, and therefore the transmission properties, can be altered by changing the spectral separation between the individual modes. Figure 3.6d-f shows the transmission spectra of the structure upon a tilt angle of −60° for different lengths of the structure. As illustrated in Figure 3.5, the LSPR (indicated at the minimum position) shifts to lower wavelengths for shorter structures. Consequently, the spectral position of the modes approach each other. Figure 3.6d-f clearly show that by changing the position of the LSPR (by length), the type of interaction and anti-crossing properties change. *E.g.* longer nanostructures could include more electrons contributing to radiative damping. Similarly, the spectral position of the WR can be altered. Figure 3.6g-i shows the structures of Figure 3.6d-f at a tilt angle of 0°. In this case, the position of the WR moves towards higher periods (see Section 2.1.1). Due to the decrease of tilt angle, the excitation efficiency of the LSPR is not as strong as with a tilt angle of −60°, leading to an overall higher transmission specifically for larger periods. A lower excitation efficiency and therefore a reduced strength of the LSPR would change the interaction between the WR and LSPR. In Figure 3.6h-i, in particular at a period of ∼ 300 nm, the modes show a crossing like behavior. This could be an indication that the reduced strength of the LSPR leads to a decrease of the coupling strength; the modes can spectrally cross. To further elaborate on the degree of coupling, the parameters of the coupled resonance, such as the losses or width, have to be evaluated and compared.[287,290] However this is beyond the scope of this thesis. The additional lines in Figure 3.6g-i could be related to higher order LSPR modes.

3.2.8 Large-Scale Realization

Figure 3.7b-d depicts the measured colors (converted with CIE 1931 xyY color space)[291] of the samples characterized in Figure 3.5e-g under different viewing angles θ and γ (see scheme in Figure 3.7a). All samples show a distinct color at negative angles whereas at positive angles color neutrality is observed. Because of the angle-dependence of the PSPR an angular color shift is observed. Colors appear in yellow to red (at evaporation angle 20°, b), red over green to purple (at 30°, c) and blue to green (at 40°, d). At normal incidence, only weak colors are observed. The color almost does not change for different viewing angles γ. Figure 3.7e shows photographs of a glass substrate illuminated by unpolarized diffuse daylight. It contains four patches (2 x 2 cm) of the same periodic nanostructures. Evaporation of aluminum onto
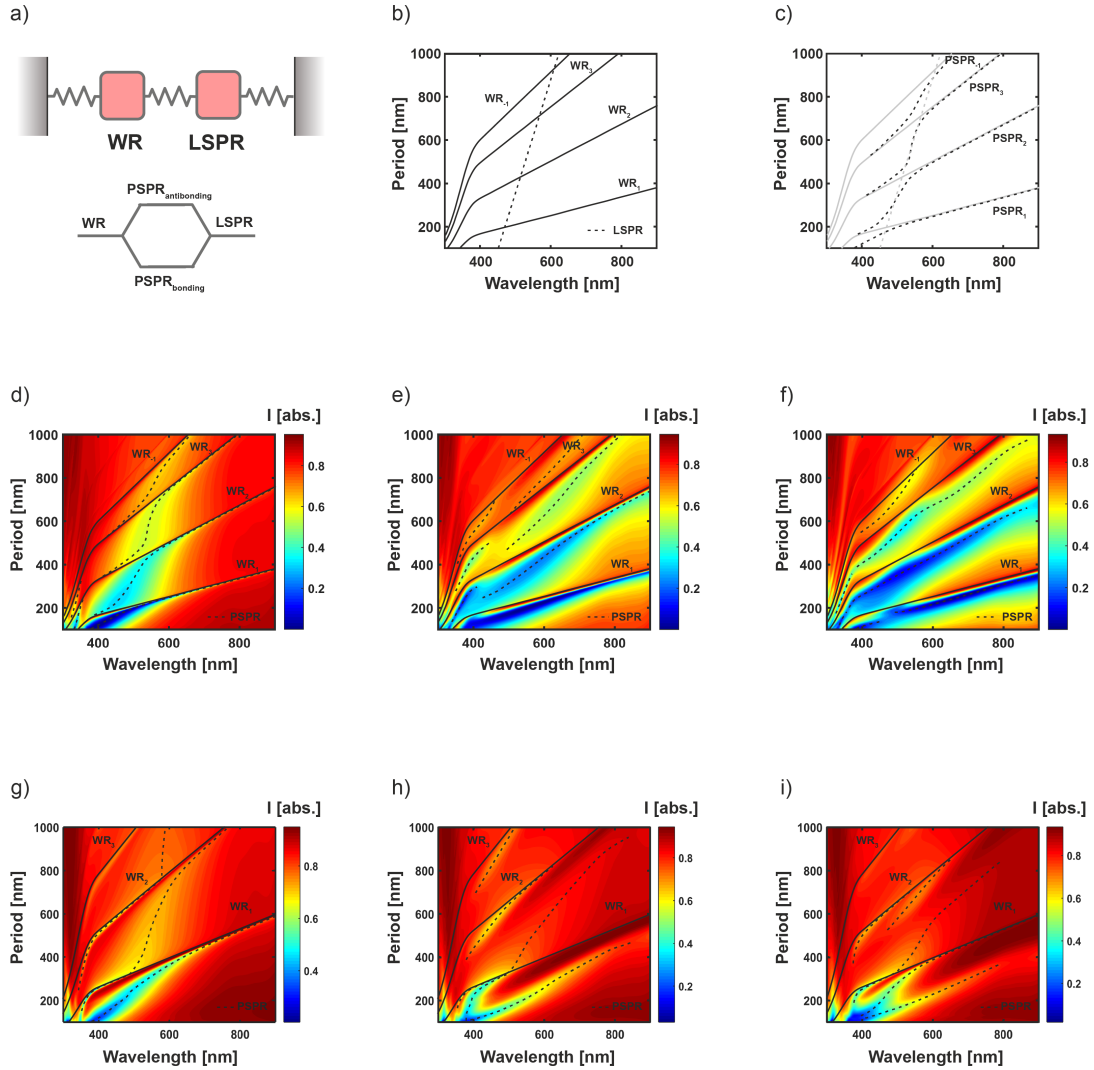
Figure 3.6 – (a) Schematic model of the coupling between the PR and the LSPR, illustrated by two coupled mechanical oscillators. The coupled mode (PSPR) can emerge as bonding and antibonding mode. (b) Conceptual figure, in the absence of interaction between the WR and LSPR. (c) Spectral signatures extracted from the simulations of (d) including the two individual modes of (b) in gray as guide to the eye. The PSPR highlights the coupled mode. Simulated spectra of the total transmission (all orders) of the periodic nanostructures with varying period at tilt angle of $-60°$ (d-f) and $0°$ (g-i). The lengths of the nanostructure is (d,g) 53nm, (e,h) 126nm and (f,i) 210nm. Spectral signatures of the WR (for different orders, see Chapter 2.1.1) and the PSPR (indicated at the minimum position) for varying periods.

Figure 3.7 – (b-d) Measured colors of the samples characterized in Figure 3.5e-g for different evaporation angles (bold) and different viewin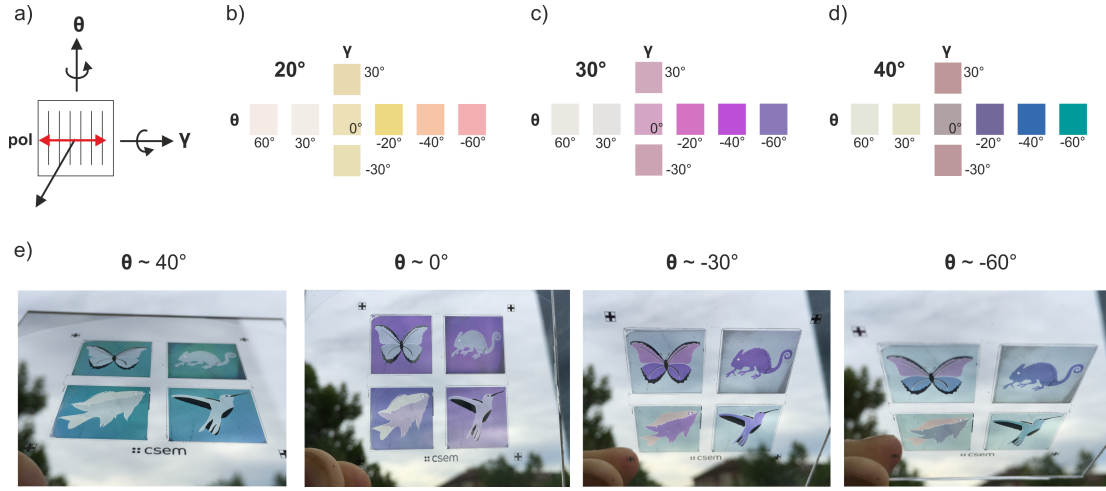g angles θ and γ at fixed polarization (red) defined in sketch (a). Colors mainly appear at negative angles θ. (e) Glass substrate with four different sample areas (2 cm x 2 cm) created by the evaporation angles 20°, 30° and 40°. Photographs were taken in front of a cloudy sky and with unpolarized light.

different photoresist masks allows patterning the substrate in distinct colors by changing the evaporation angle and direction. The pattern was chosen such that each patch contains one animal utilizing structural colors in nature;[6] a *morpho* butterfly (evaporation angle 30° top, 40° bottom), a *chameleon* (40°), a *damselfish* (20° top, 30° bottom) and a *hummingbird* (40°). The background of the animals was evaporated at an angle of 40° from the other direction. Furthermore the wings and outline of the *hummingbird* and *morpho* butterfly respectively were evaporated (30 nm) onto the glass substrate before replication of the periodic nanostructures; they appear as shiny, nontransparent areas. At negative angles the animals appear in the colors yellow, pink and blue/green, depending on the tilt angle. The background appears in blue and green at steep angles but in the opposite direction. This color switching increases the appearance of the color and enhances attractiveness of the device. The color inhomogeneity of the structures fabricated at the same evaporation angle is mostly caused by the angular spread of the image for the observer. Additionally, the finite distance to the evaporation source leads to slight variation along the sample. This can be improved with a more distant source, which would be straightforward in roll-to-roll fabrication. At normal incidence a slight color appears which is mainly caused by the non-resonant polarization appearing blueish. This on the other hand can help to increase visibility of the colors at higher angles, since generally in unpolarized light the contrast of the plasmonic color decreases.

For a more visible representation of the obtained colors, Figure 3.8 shows a CIE color

plot containing the samples of Figure 3.7b-d. The white triangle displays the standard RGB color space (sRGB). Simply by changing the evaporation angle a wide range of this color space can be covered.
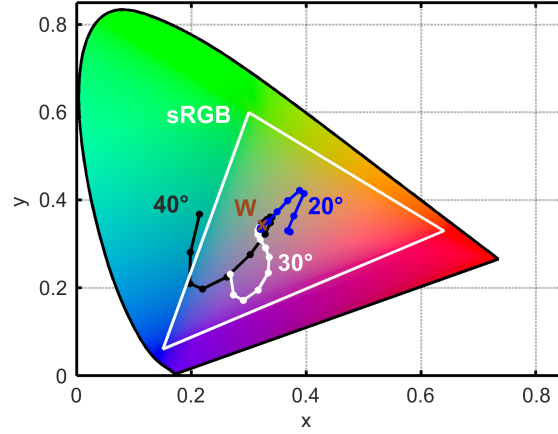

Figure 3.8 – CIE color plot containing the measured samples of Figure 3.7b-d with evaporation angles 20°, 30° and 40°. The single data points are represented as dots. Varying colors are obtained for negative tilt angles, whereas positive tilt angles are located around white (W) for the different samples. The white triangle indicates the standard RGB color range.

3.3 Discussion

Besides changing the evaporation angle, the colors can be varied by the period, the nanostructures profile which lead to different geometrical shape of the aluminum nanolamellas (see Figure 3.5) or by the orientation of the underlying structures or lamellas. These enable practical large-scale fabrication of complex angular variable color images. While intense colors are obtained at negative angles, the colors at normal incidence are faint. They can, however, be enhanced by a larger duty cycle. A complex master structure containing pixels of such different nanostructures can enable fabrication of an optically very complex and appealing structure fabricated at only one fixed evaporation angle.

The asymmetrical color rendering effect fabricated and analyzed in this work has attractive applications in visual authentication allowing securing documents and goods (anticounterfeiting), so called optical security. Besides this specific studied geometry, perfect oblique metallic nanolamellas as well as nanolamellas with minor geometrical variations can be designed to generate such highly asymmetric optical behavior. Simulations show a strong dependence of the resonance condition on the surrounding media. If the resonance is broad enough, this can be used to tune the color appearance. More information are given in Chapter 4. On the

other hand relative narrow resonance dips (*e.g.* FWHM $\sim$40 nm, λ_R=746 nm, period 300 nm, see Figure 3.6) accompanied by a strong intensity change ($\sim$5%-80% with p-polarized light) could be of great interest for refractive index change-based sensing applications. Finally, the strong absorption of light in the plane of the nanolamellas (see Figure 3.4), can find use in thin-film photovoltaics. The active material would need to be placed between the nanowires where absorption is highest.

In contrast to diffractive gratings (such as blazed gratings) where the obtained color is solely governed by the grating equation, the proposed effect is based on zero order transmission. Zero order effects do not require a certain viewing angle or change rapidly with the illumination angle: this enables clear visibility in diffuse daylight or poor light conditions, which is often not possible with higher order optical effects (see Section 2.1.1). Furthermore, transmission or reflection efficiencies can be higher, since light does not dissipate into higher diffraction orders. Specifically in this case the efficiency and the plasmon excitation can be accurately controlled. This leads to a strong suppression of the optical effect in one tilt direction, which would be very challenging to achieve with diffractive gratings. Besides aluminum other material such as silver, gold or copper could be used to generate an equivalent effect at larger wavelengths (such as near-infrared and beyond).

3.4 Conclusion

In summary, symmetry breaking structural colors based on tilted aluminum plasmonic nanowires is demonstrated. High transmission $\sim$80% and high absorption $\sim$90% is observed in selected frequency ranges, leading to strong color rendering even for unpolarized light. Immersed laser interference lithography allows to fabricate periodic subwavelength features on a large-scale and enables tunability of the geometrical parameters during the fabrication process. Symmetry breaking colors are generated by evaporating aluminum from oblique angles onto the fabricated nanostructures, leading to tilted nanowires. This asymmetric geometry allows plasmon resonances to be excited by light incident from one side only. Strong and narrow absorption bands are generated by strong coupling between propagating resonances and plasmon resonances, giving rise to characteristic Fano line shapes. The strength of the coupling depends on the angle of incidence and the spectral positions of the individual resonances. While the period affects mainly the propagating resonance, the length of the aluminum nanolamellas defines the plasmon resonance. The resulting Fano dip can be tuned over the complete visible spectrum, giving rise to distinctive structural colors that range from red to blue and depend on the observation angle.

3.5   Experimental Details

Fabrication

Immersed laser interference lithography was done with a HeCd laser (441.6 nm) on a damped table. A prism (n_{prism} = 1.64 at 435.8 nm, F2 glass) was placed onto the photoresist covered by an index matching immersion liquid (n_{liquid} = 1.59 at 435.8 nm, from Cargille, BK7 immersion liquid). The final device shown in Figure 3.7 was made by fourfold replication (each square) of the master structure. Subsequently a protecting photoresist was exposed through distinct photomasks to evaporate aluminum at different angles (20°, 30° and 40°) and directions for the different pattern. The photographs were done in unpolarized light in front of a cloudy sky.

Characterization

The angle-dependent measurements were done with a Perkin Elmer spectrometer (Lambda 9). Zero order transmission was directly measured with and without a Glenn-Thomson polarizer between the sample and the light source. The sample was fixed onto a manual rotation stage and measured every 10° for both tilt angle configurations (polar and azimuthal). The size of the illumination spot was about 3x5 mm, the measured samples were about 2x2 cm. The measured transmission values were transferred into RGB values (D65 illuminant) with a home-made MATLAB script (version 2015).

Computations

Far-field computations were done with RCWA from 400-700 nm, in 0.5 nm steps. Zero order transmission computations were done for varying incidence angles (from -60° to 60°, 10° step) or varying period (from 100 nm to 300 nm, 0.5 nm step) and length (10 nm to 220 nm, 0.5 nm step). The near-field simulations were done with SIE.[249] First a far-field zero order transmission spectrum was computed (400 nm to 700 nm, 0.5 nm step), then a near-field map of the structure at the indicated points (see Figure 3.4) was done (precision of 0.5 nm). The intensity is plotted logarithmically.

4 Color Control of Plasmonic Substrates with Inkjet Printing
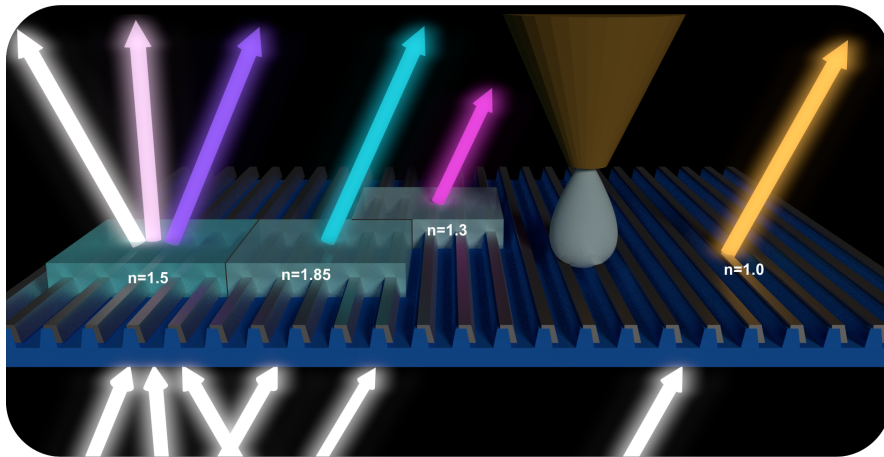
Here a versatile method for modifying the optical properties of plasmonic substrates by inkjet printing of commercially available, transparent inks with various refractive indices is presented. This large-scale and cost-efficient process is demonstrated on tilted aluminum nanolamellas, see Chapter 3. They show vivid and bright colors based on a Fano resonance, which is highly susceptible to the surrounding material. Further, color rendering is strongly angle-dependent and asymmetric.

4.1 Introduction

To date, replication of microscopic pattern consisting of nanostructures often require a lithographically defined master structure, which is complex and expensive to fabricate (*e.g.* e-beam) and can not be adapted in a simple manner.[84] On the other hand, conventional inkjet printing techniques offer customized color generation and therefore are one of the most common processes in the graphic industry.[292] Typical coloration is based on chemical dyes or pigments, which are prone to photobleaching and smearing when coming into contact with water or grease.[2] Novel techniques allow printing of *e.g.* quantum dot[293] or nanoparticles.[238] Although such color generating structures can be printed below the diffraction limit,[240] the used inks can be difficult to obtain or have limited lifetime. In addition, such techniques are often severely limited in printing speed,[240] require special dispensing techniques[238] or accurate control over the thickness of the dispensed material.[239] Finally, the color appearance is either stable (quantum dot)[293] or iridescent (interference).[239]

Here, an approach for customizing the optical appearance of plasmonic substrates *via* inkjet printing is presented. Plasmonic substrates are used as a cost-efficient, adaptable and versatile basis, while inkjet printing allows the pixelwise control over the resulting colors. A standard desktop printer without modifications is used to dispense transparent and commercially available inks with different refractive indices (RI-ink). In particular, plasmonic substrates consisting out of tilted aluminum nanolamellas are used, see Chapter 3. The optical appearance is based on a Fano resonance, which is strongly modified by the RI, enabling printed pixels with an ink-dependent color effect. Further, the structures show an angle-dependent and asymmetric color appearance, which can be varied by the viewing angle.

4.2 Results and Discussion

4.2.1 General Principle

Figure 4.1 shows the process scheme for inkjet printing on plasmonic substrates. The plasmonic substrate is fabricated by replication of a periodic pattern into UV-curable sol-gel, as described
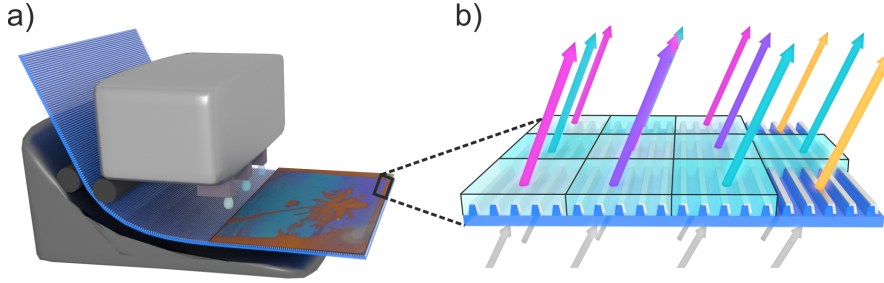
Figure 4.1 – Fabrication scheme including: (a) inkjet printing of transparent RI-inks onto the plasmonic substrate. (b) Scheme of the pixelized color generation under tilted illumination.

in Chapter 3. Subsequently aluminum is evaporated at an oblique angle. In contrast, the replication is done on a PET foil to ensure flexibility of the substrate. Finally, inkjet printing of transparent RI-inks onto the uniform plasmonic foil locally alters the plasmon resonance, which gives each pixel a distinct optical appearance, see Figure 4.1. Due to the geometrical asymmetry, the optical appearance is pronounced at a tilt angle. Optionally, to circumvent abrasion, an additional low RI material with high viscosity can be applied for protection *via* spin coating. This only slightly affects the optical properties of the already dispensed inks, as further depicted in Figure 4.3.

4.2.2 Geometrical Influence onto the Resonance

The aluminum nanolamellas reveal a characteristic Fano-like line shape that originates from strong coupling between a localized surface plasmon resonance (LSPR) and a propagating resonance (PR), see Chapter 3. Figure 4.2 shows the transmission of the structure at an incidence angle $\theta = -60°$. While the LSPR is a feature of the geometry of the individual plasmonic resonators (*e.g.* tunable *via* evaporation angle, see Chapter 3), the PR is influenced by their periodic arrangement. Both resonances are susceptible to the RI of the surrounding,[16] see Figure 4.2. While the RI of the surrounding coating (n_{coat}) can be varied by inkjet printing (RI-ink), the RI of the supporting substrate (n_{sub}) remains constant (see schemes Figure 4.2). A spectral signature of the PR is the Wood-Rayleigh anomaly (WR),[18] see Chapter 3. The position can be calculated by $\lambda_R = p(\sin(\theta) + n)$,[294] with the period p and the refractive index n of the media. The presence of two dielectric materials, leads to a WR_{coat} of the coating and a WR_{sub} of the substrate (solid and dashed black line in Figure 4.2).

The spectral position of the LSPR depends on the ratio of n_{coat} to n_{sub} (filling ratio) in the plane of the plasmonic structures (see schemes, Figure 4.2d). While the spectral position of the LSPR changes nearly 290 nm per refractive index unit (RIU) for structures surrounded
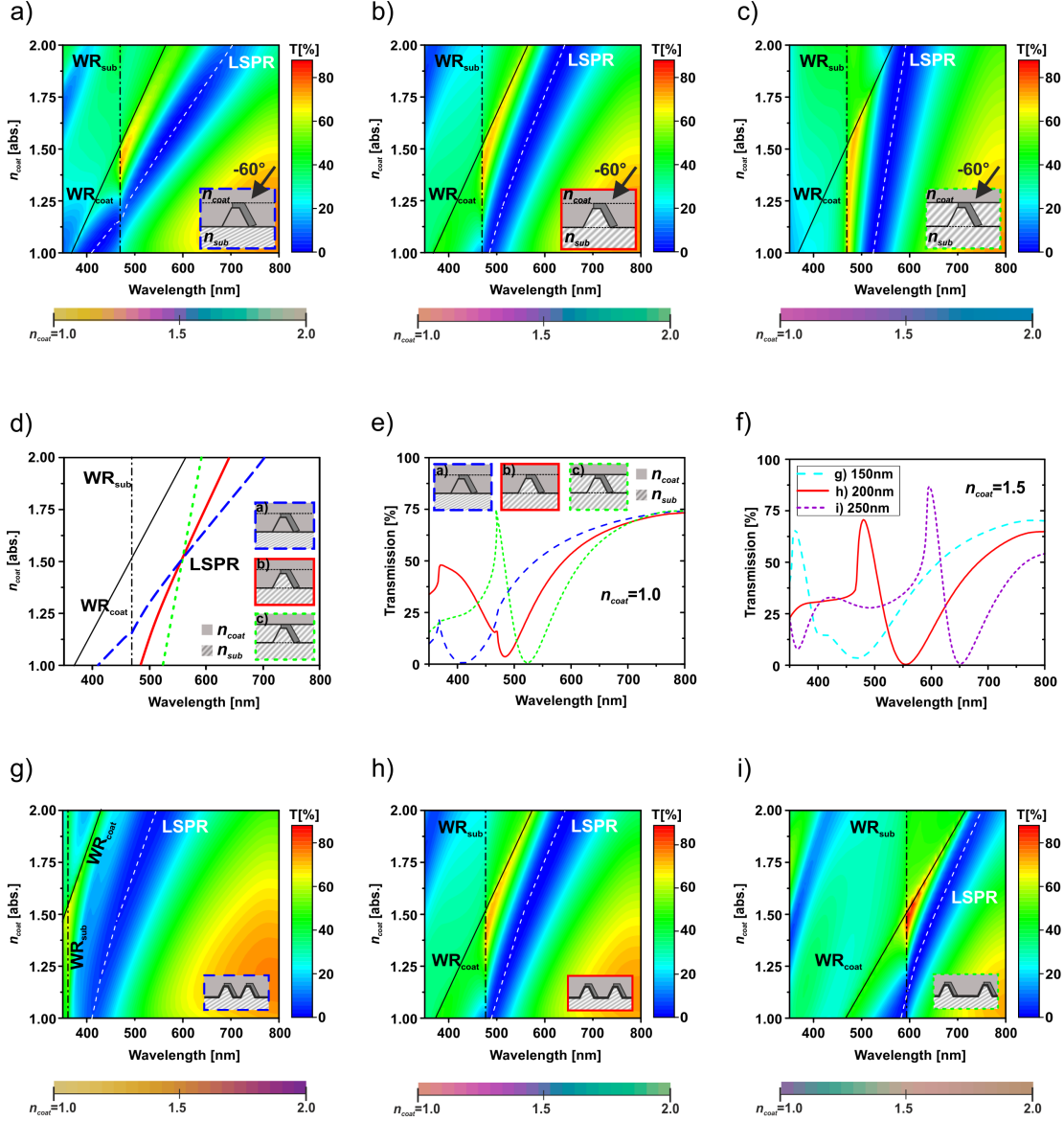
Figure 4.2 – Simulated transmission spectra as a function of n_{coat} at θ=-60°. (a-c) varying percentage of n_{coat} compared to the layer with (a) $\sim$ 91 %, (b) $\sim$ 64 % and (c) 0 %. The corresponding position of the LSPRs are compared in (d). (e) shows the spectra of (a-c) at $n_{coat} = 1.0$. (g-i) varying period of the structure with (g) p=150 nm, (h) p=200 nm and (i) p=250 nm. (f) shows the spectra of (g-i) at $n_{coat} = 1.5$.

by mainly n_{coat} (blue, Figure 4.2a), it shifts only ~ 70 nm/RIU for structures surrounded by mainly n_{sub} (green, Figure 4.2c). Ultimately there is a trade-off between color shifting capability (see Figure 4.2d) and ease of fabrication. A geometry with a relatively high susceptibility of ~ 160 nm/RIU (red, Figure 4.2b) was used, which remains reasonably easy to fabricate (same structure as in Chapter 3). The strong dependence of the LSPR on n_{coat} can be explained with a high near-field enhancement between the nanolamellas (see Chapter 3), enhancing the interaction with the enclosed material. This is likely linked to the in-plane propagation of the PR (see Figure 3.4).

In conclusion, both spectral features respond to the RI of the surrounding. While the position of the LSPR can be modified by the filling factor (Figure 4.2d), the position of the WR is altered by the period (Figure 4.2g-i, *cf.* Figure 3.5) and the incident angle θ (Figure 4.3). Close proximity of the two resonances can lead to a Fano-like line shape by strong coupling (see Figure 4.2e,f). A spectral shift (*e.g.* induced by different RI) of such a pronounced resonance leads to a great color change and therefore distinct perception, in contrast to broad resonances. For the proposed tilted structures such strong coupling in particular is the case at an incidence angle of $\theta = -60°$, see Figures 4.2 and 4.3.

4.2.3 Angle- and Refractive Index-Dependent Transmission

Figure 4.3 shows the angle-dependent transmission plots for the plasmonic substrates bearing different n_{coat}. With steeper angle (towards $0°$), the WR's (WR_{coat}: gray cross, WR_{sub}: dashed line) shift to the blue (see equation before). Additionally, the strength of the LSPR (orange plus) decreases with increasing angles due to the tilt of the plasmonic structure. These effects lead to a flattening of the Fano-like line shape, hence, to an asymmetric color generation (see color bars), also reported in Chapter 3. Finally, as discussed for Figure 4.2, the RI of the coating strongly changes the position and shape of the coupled resonances, leading to distinct color generation (color bars) at negative angles. The agreement between measurements and simulation is very good.

4.2.4 Color Generation and Mixing Capabilities

The RI- and angle-dependence is further depicted in Figure 4.4a,b. The transmitted color is computed (n_{coat}=1.0-2.0, white lines) and measured (different RI-inks, black cross) for $\theta = -60°$ and $+40°$. At positive angles, almost perfect color neutrality (w) is observed, whereas at negative angles distinct vivid colors are visible. The circular arrangement indicates the wide range of
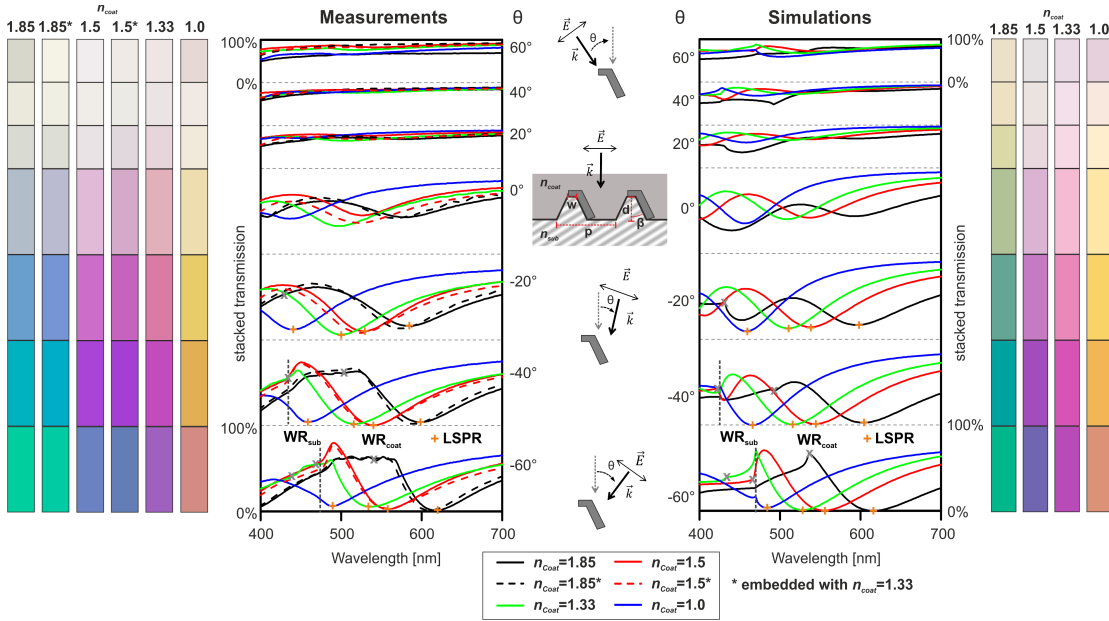
Figure 4.3 – Transmission spectra of TM-polarized light for different angles θ and RI-inks (colored lines). The * indicates the already printed RI-inks which were finally embedded with a RI-ink of n_{coat}=1.33. Measurements are shown on the left and simulations on the right. Observed colors at the corresponding angles are given on the side of the graphs. The sketches in the middle illustrate the configuration in terms of the electric field E, the wavevector k and the angle θ. The scheme in the middle illustrates the geometry of the structure, with p=200 nm, d=120 nm, w=35.5 nm, β=18° and thickness of Al=13 nm.

colors available with the presented method, even exceeding the CMYK color range. Besides the measured four colors (crosses), more colors can be obtained by printing adjacent pixels with distinct RI-inks. This color mixing is similar to pigment mixing with a commercial inkjet printer. Figure 4.4c-f illustrates the mixing capabilities of colors with different RI-inks. Figure 4.4c shows the simulated color generation of increasing the ratio of $n_{coat} = 1.00$ to $n_{coat} = 1.85$. This can be realized by printing $n_{coat} = 1.85$ several times, measurements see Figure 4.4d. Such mixing can be done with basically any kind of RI-inks present on the white line. Figure 4.4e,f illustrates the potential mixing of the 4 demonstrated basic colors (crosses) including color bars. Alternatively, it is possible to generate the colors along the circle, by using inks with the appropriate RI or actual mixing of RI-inks. The latter would strongly enhance the range of possible colors, which can be printed with only two inks of very low and very high RI.

4.2.5 Large-Scale Realization

The used plasmonic structures are ideal candidates for the asymmetric and RI-dependent color generation due to the tilt of the nanolamellas arranged on a small structural support. Nev-
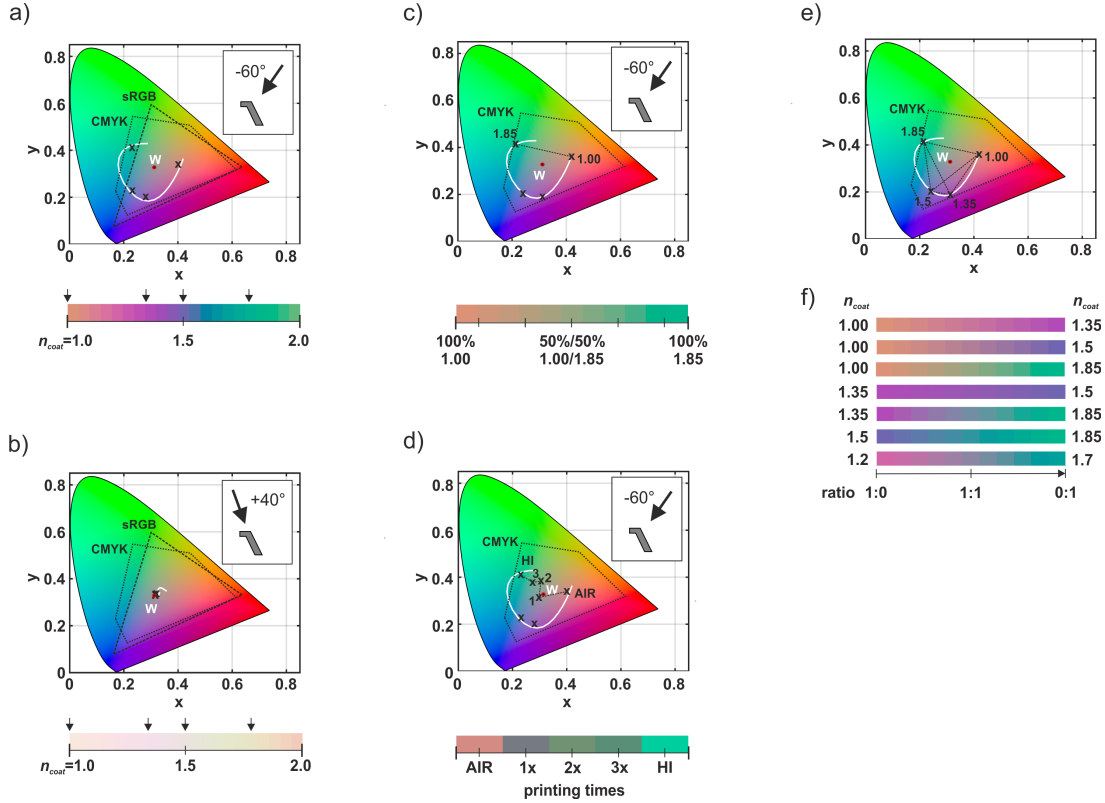
Figure 4.4 – (a,b) CIE color plots for $\theta = -60°, +40°$ with $n_{coat} = 1.0 - 2.0$ (white line, color bar below). The measured samples (black cross, arrow) and the CMYK, sRGB color ranges are indicated. (c) Simulated mixing of $n_{coat} = 1.0$ and $n_{coat} = 1.85$ at $\theta = -60°$. (d) experimental realization of (c) by multiple printing of $n_{coat} = 1.85$ (indicated as crosses). (e) Simulated mixing of RI-inks with (f) corresponding color bars. The sRGB color range is indicated by the dashed triangle.

ertheless, the proposed method could be applied for a large variety of plasmonic structures. To demonstrate this, non-ideal, but relatively cost-efficient and readily available nanostructures were used and replicated, see Figure 4.5d. After angular evaporation of aluminum, an image with different RI-inks was inkjet printed. Clearly, the image and its different colors are only visible upon one tilt direction (Figure 4.5a,b), highlighting the optical symmetry breaking effect, see Chapter 3. Such hidden features are highly attractive for optical security applications. Further, a bending of the foil leads to color generation only in parts of the sample (Figure 4.5c). The optical appearance is only governed by light directly transmitting through the sample, so-called zero order. This enables use in diffuse light (*e.g.* cloudy sky). In contrast, diffractive structures would lead to an overlay of light from different parts of the sample, creating a faint or unclear image, see Chapter 2.1.1. Furthermore, the colors could rapidly change with viewing angle. This makes a clear recognition of the optical image more difficult. In contrast, Figure 4.5c shows that
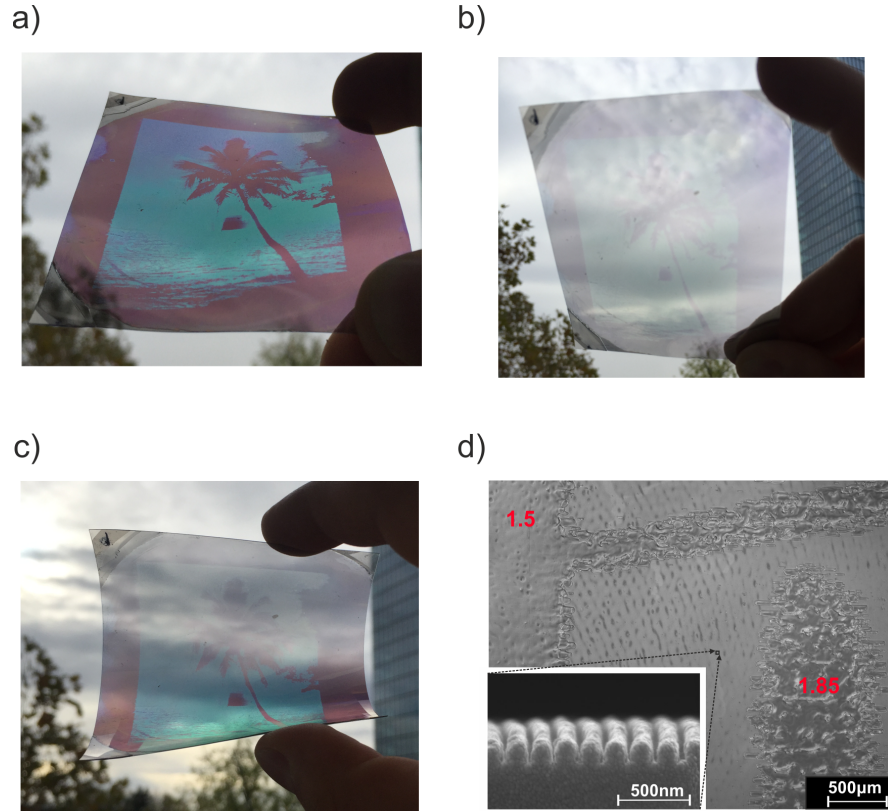
Figure 4.5 – (a-c) Images of a fabricated sample (5x6 cm) at different viewing angles with color generation only upon certain tilt angles. Photographs were taken in front of a cloudy sky and with unpolarized light. (d) SEM of replicated nanostructure (bottom left) and light microscope image of a inkjet printed sample. The numbers indicate the RI of the ink.

bending of the sample shows a relatively constant color (for the same tilt direction, *e.g.* bottom or top part). Finally, it is important to note that the plasmon resonance is only excited with TM-polarized light; With TE-polarized light almost no optical features are observed, see Figure 3.3. Since the plasmon resonance is so pronounced, color generation is clearly visible even in unpolarized light. Besides, the thin layer of aluminum shows high transmission values allowing bright and vivid colors.

4.3   Conclusion

A wide range of vivid and bright colors achieved with inkjet printed plasmonic structures is demonstrated. While uniform aluminum plasmonic substrates can be fabricated in a cost-efficient roll-to-roll compatible process, inkjet printing enables their customized modification. In contrast, in Chapter 3 distinct color generation is achieved by different evaporation angles,

leading to distinct geometries of the plasmonic structures. Such additionally required fabrications steps are not desired in large-scale manufacturing. Compared to conventional dyes or other inkjet printing techniques *e.g.* quantum dots, plasmonic colors can show variable and novel optical appearances. Such customized and variable optical effects are highly desired in applications, such as optical security[81,268] or decorative elements, but also for *e.g.* camera applications.[72] Besides transmission, such printable color generation is also observed in reflection. Finally, the flexibility of the plasmonic foil offers exciting opportunities for novel applications.[295]

A greater palette of colors can be achieved by printing adjacent colored pixels, *in-situ* mixing of different refractive index inks or by extending the range of available inks and plasmonic substrates. Simulations showed that the utilized resonances and corresponding printed inks could be adapted to be active in other spectral regimes, *e.g.* near-infrared (see Figure 3.6). Further, alternative plasmonic structures (*e.g.* nanodisks[46]) with distinct optical effects,[75] could be customized with the proposed method. Using inkjet printers with a smaller dispensing volume, *e.g.* NanoDrip,[293] could strongly increase the spatial resolution of the plasmonic color printing. Finally, the fabricated structures are non-organic and can be well protected, therefore are not subject to abrasion, oxidation, smearing or UV degradation, such as conventional colors.[180]

4.4 Experimental

Fabrication

More details about fabrication of the plasmonic substrates are given in Chapter 3. Aluminum (8 nm) was evaporated with an electron beam evaporator. A commercially available inkjet printer (Epson, WF-2010) was used to dispense commercial inks with $n=1.85$ and $n=1.5$. Further an ink with $n=1.33$ was spin coated. The final device shown in Figure 4.5 was made by replication of a readily available nanostructures (5x6 cm, period: 180 nm, duty cycle: 0.5, rectangular profile) and printing a sunset image (Andrew Mandemaker/CC BY-SA 2.5) with a resolution of 600 dpi. The photos were taken in unpolarized light in front of a cloudy sky.

Characterization

The transmission measurements were done with a spectrometer (Perkin Elmer, Lambda 9) and a Glenn-Thomson polarizer. The illumination spot was about 3x5 mm. A home-made Matlab script (version 2015) was used to transfer the measured transmission values into RGB values.

Computations

Computations were done with rigorous coupled-wave analysis (RCWA), [250] , see Section 2.3.3, in the range of 400-700 nm, in 2 nm steps. The angle of the zero order transmission was varied from from $-60°$ to $60°$ with $20°$ steps and varying refractive index of n=1.00 to 2.00, in 0.05 steps. For simplification, a refractive index constant over all wavelengths $(n(\lambda) = n)$ is assumed. A CIE color plot (CIE 1931 color space) [291] including the range of sRGB (standard: IEC 61966-2-1:1999) and CMYK (profile: U.S. Web Coated SWOP v2) was used to plot the simulated color values.

5 Fourfold Color Filter Based on Plasmonic Phase Retarder
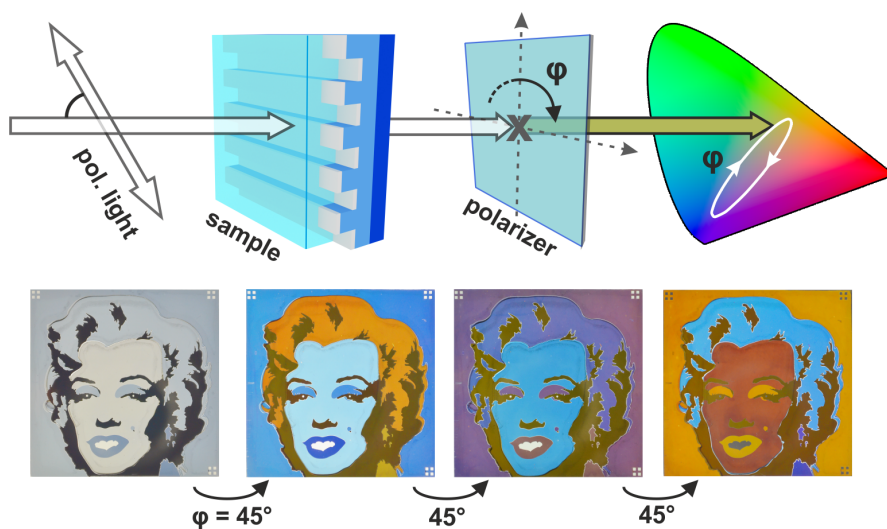
I present a plasmonic color filter based on periodic subwavelength silver nanowires, capable of changing the output color by simple rotation of a polarizer. The effect is enabled by a wavelength-dependent phase shift near the plasmon resonance, giving rise to a wavelength-dependent rotation of the incident polarization. Subsequent rotation of an analyzing polarizer leads to an output of four distinct colors (*e.g.* yellow, blue, purple and red) and combinations thereof. The plasmon resonance itself can be tuned throughout the visible spectral region by proper choice of fabrication parameters.

5.1   Introduction

The wide tunability of plasmonic filter substrates over the whole visible range makes them well suited for display technologies or imaging applications,[76,147,153,264,270,296,297] where in particular the control of polarization is essential. Devices controlling the polarization state, *e.g.* wave retarders, are realized by using birefringent materials (*e.g.* mica),[298] liquid crystals or, more recently, diffraction gratings.[299] Phase retardation is caused by different propagation speeds along the crystal axes and requires a certain thickness of the crystal. In contrast, wave retarders based on thin plasmonic or metasurface substrates can induce a phase shift at the resonance of the structure or the surface itself leading to a control of the output polarization.[62,63,300–302] This principle has recently also been utilized for metasurface holograms.[63,184] The origin of this polarization control is that the excitation of localized surface plasmon resonances (LSPR) depends intrinsically on the polarization of the incident light.[303] This polarization sensitivity was exploited for stereo view in reflection[179] and spectrally tunable transmission filters.[153] Switching between states is enabled by changing the polarization of the incident light with a passive polarizer or an integrated tunable layer (such as an electrically tunable liquid crystal).[304]

Novel display technologies and CMOS sensors show a great need for compact optical filters capable of actively changing the output color[147,153,304–306] or polarization[307] and being able to act as photodetectors.[297] Existing filters are often bulky, limited in the acting region, or costly and not integratable in high-throughput fabrication processes. Transmissive filters based on plasmonics are interesting candidates due to their compactness and color tunability,[46,76,147,173,174,264] even on flexible substrates.[177] Until now they were often limited to a specific range of colors and suffer from fabrication complexity (*e.g.* utilize focused ion beam (FIB)[76,173]), see Section 2.2. On the other hand, plasmonic phase retarders show great potential in shaping the incident polarization,[308] but are often designed to be independent of wavelength (achromatic) or active only in the infrared or microwave range.[298,299]

Here I introduce a plasmonic phase retarder (PPR) that performs fourfold color filtering in the visible spectral range. The substrate altering the polarization of the incident light consists of a periodic array of silver nanowires. This structure supports localized surface plasmon resonances (LSPR) capable of inducing a strong phase shift for one polarization setting. As

a result, the rotation of an analyzing colorless polarizer gives rise to four distinct colors and their combinations. The geometry is optimized to make the optical effect independent of the tilt angle,[148,265] enabling use in ambient light conditions. The structures have been fabricated with an up-scalable and cost-effective process and are designed to be resistant to wear.

5.2 Results

5.2.1 Fabrication
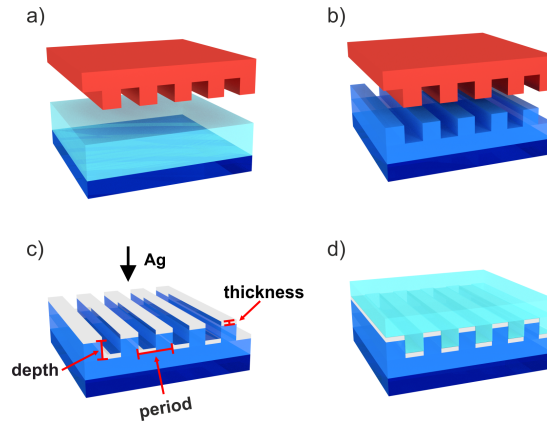
Figure 5.1 – Fabrication of plasmonic silver nanowires. The process includes (a) replication of a master structure in sol-gel, (b) demolding of replicated structure, (c) evaporation of silver, and (d) final embedding. (c) illustrates the parameters of the structure such as period, depth and thickness of metal.

Subwavelength silver nanowires are fabricated by nanoimprint lithography and standard metal evaporation, see Figure 5.1a-c. The parameters of the nanostructures (period: 160 nm, depth: 70 nm), such as the period and depth, were optimized to decrease the angle- and orientation-dependence of the generated color and to tune the localized surface plasmon resonance (LSPR) into the visible. The thickness of the silver nanowires also influences the position of the LSPR and was chosen to be in the range of 10-30 nm. With lower thickness the resonance disappears and with higher thickness the transmission decreases. After evaporation of silver the sample is embedded in UV-curable polymer providing protection for ambient use, see Figure 5.1d.

---

[i]The illustration of the polarization and angle of Figure 5.2 is similar to the one of Figure 3.3. Here the focus is more on rotation of the sample in comparison to the observer.
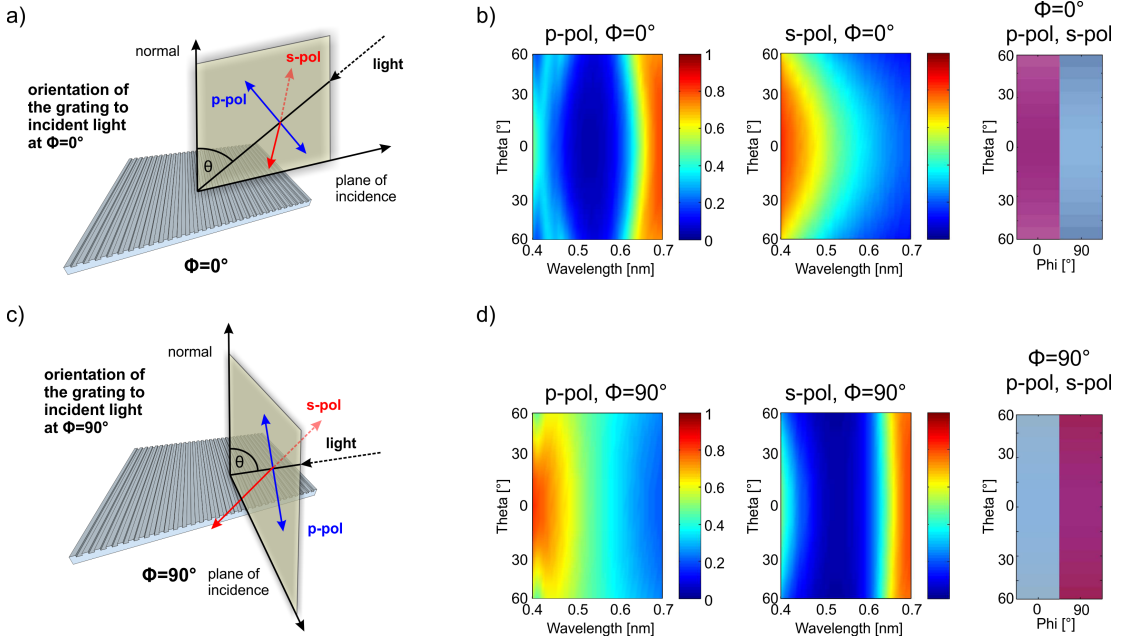
Figure 5.2 – (a) Scheme of the measurement setup with the incident tilt angle θ, the plane of incidence, the polarization s-pol and p-pol and a sample rotation angle of $\Phi = 0°$. (b) Simulated transmission map of the sample upon different angles with the corresponding color. The angle-dependency is weak, especially for the appearing color. (c,d) correspondingly with $\Phi = 90°$.[i]

5.2.2   Angle-stable Transmission

Figure 5.2a shows a scheme of different possible incident angles onto the sample. The tilt angle is indicated by θ, whereas Φ defines the rotation angle of the sample compared to the normal. Likewise an observer could view the sample from a different viewing direction (corresponding to a different Φ). To have the highest angle- and direction independent color generation, the transmission should be stable along the tilt angles for both orientations of the structure. In the following (Figures 5.2-5.6) I will refer to a structure with a period of 160 nm, a depth of 70 nm and a thickness of silver of 30 nm. Figure 5.2b shows the simulated transmission plot of this structure upon different tilt and rotation angles. The observed colors are indicated on the right side. Polarized light with the electric field within the plane of incidence is called p-polarized light (p-pol), while the perpendicular case is called s-pol (s-polarized). In other literature, p-pol and s-pol are referred to transverse-magnetic (TM) and transverse-electric (TE), respectively. For varying tilt angle the spectra remain relatively constant; accordingly the observed colors only show minor variance. Applying a polarizer onto the sample simultaneously creates p-pol and s-pol when considering the plane of incidence at rotation angles $\Phi = 0°$ and $\Phi = 90°$ (or *vice versa*). In other words, at normal incidence ($\theta = 0$) p-pol at $\Phi = 0°$ and s-pol at $\Phi = 90°$

can be considered as identical. This is not the case at a tilt angle ($\theta \neq 0$), when the sample is viewed perpendicular ($\Phi = 0°$) or parallel ($\Phi = 90°$) to the periodic nanostructures. The geometrical parameters of the sample are chosen to show a high angle-independence for both orientations of the sample. Consequently the same (or similar) color can be observed when viewing the sample from different tilt angles and directions (corresponds to sample rotation). Therefore it is sufficient to describe the transmission property only with the rotation angle of the polarizer (φ). For the following the sample will be described at a rotation angle of $\Phi = 0°$.

5.2.3 General Principle

Figure 5.3a illustrates the working principle of the plasmonic phase retarder (PPR) consisting of periodically aligned subwavelength silver nanowires. Linearly polarized visible light is incident on the PPR perpendicular (p-pol) or parallel (s-pol) to the nanowires. The corresponding measured transmission spectra are shown in Figure 5.3b. A localized surface plasmon resonance (LSPR) is excited in p-pol leading to a resonant dip (at λ_R) in the spectra. The spectrum of s-pol light is broadband with no sharp resonances. The spectrum of mixed-pol (superposition of p-pol and s-pol) is relatively flat and corresponds to the average of the p-pol and s-pol spectra. This is similar to a spectrum obtained by unpolarized light, but with slightly lower intensity.

To generate distinct colors I set the input polarizer to $\varphi_1 = 45°$ (diagonally polarized) and add an additional polarizer with settings $\varphi_2 = 0°, 45°, 90°$, and $135°$ to the output of the PPR. The resulting four transmission spectra are shown in Figure 5.3d. For $\varphi_2 = 0°$ and $\varphi_2 = 90°$ I obtain spectra similar to s-pol and p-pol in Figure 5.3a, respectively, but with an intensity decreased by $1/\sqrt{2}$. In contrary, the spectra for $\varphi_2 = 45°$ and $\varphi_2 = 135°$ clearly differ from the transmission spectrum of the PPR with mixed input state (Figure 5.3b), which is an indication of birefringence (like liquid crystals). This wavelength-dependent birefringence leads to a rotation of the incident polarization, such that the transmission through the analyzing polarizer is enhanced or weakened as a function of the wavelength, depending on the polarization angle. Since a strong spectral change is observed near the plasmon resonance λ_R, I conclude that the plasmonic resonance (excited by p-pol) is the main reason for the wavelength-dependent rotation of the phase. As illustrated in Figure 5.3c, a phase shift of p-pol causes the in-phase peak intensity (I_{max}) to change direction (see * below and † above the resonance, respectively), giving rise to four distinct spectra (see Figure 5.3d) and combinations thereof. The rapid phase change near the plasmon resonance can be described by a harmonic oscillator model: the sharper the resonance is, the faster the phase changes and the more rapid is the transition between the
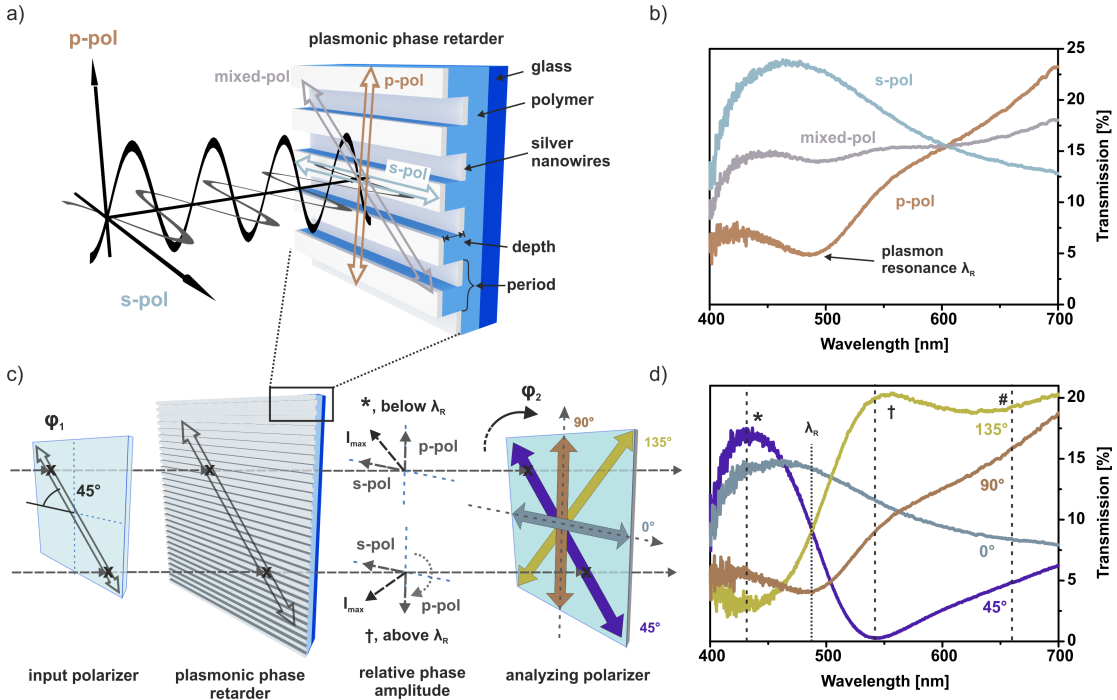
Figure 5.3 – Basic principle of the plasmonic phase retarder (PPR) and its application as color filter. (a) Sketch of the PPR prior embedding, displaying the orientation of s-, p- and mixed-polarized light. (b) Measured transmission spectra for s-pol, p-pol and mixed-pol. (c) Color filter based on the PPR with diagonally-polarized incident light ($\varphi_1 = 45°$) and a variable analyzing polarizer. For p-pol input, the phase shift near the plasmon resonance λ_R (see sketch) leads to an angular change of the peak intensity (I_{max}). Distinct colors are generated after passing through the analyzing polarizer (d). The spectra and states are shown in terms of the measured RGB colors.

diagonal states ($\varphi_2 = 45°$ and $135°$). Consequently, the contrast of these states is considerably stronger than the contrast of the pure s-pol and p-pol states. The color values used in Figure 5.3b,d have been extracted from measurements. I multiplied the lightness values (L) by 1.5 (in HSL color space) to increase visibility. This can be seen as an increase of the illumination source, leading to greater lightness of the colors.

5.2.4 Plasmonic Phase Shift

Figure 5.4 shows measured transmission spectra for different settings of the input polarization ($\varphi_1 = 0°$, $45°$, $90°$, and $135°$) and as a function of the output polarization angle ($0° < \varphi_2 < 360°$, in steps of $1°$). For $\varphi_1 = 0°$ and $90°$ the maxima of the s-pol state (at $\varphi_2 = 0°$) and p-pol state (at $\varphi_2 = 90°$) are clearly visible (Figure 5.3b). For both the s-pol and the p-pol states, the transmission is blocked if the analyzing polarizer is at a right angle to the incident
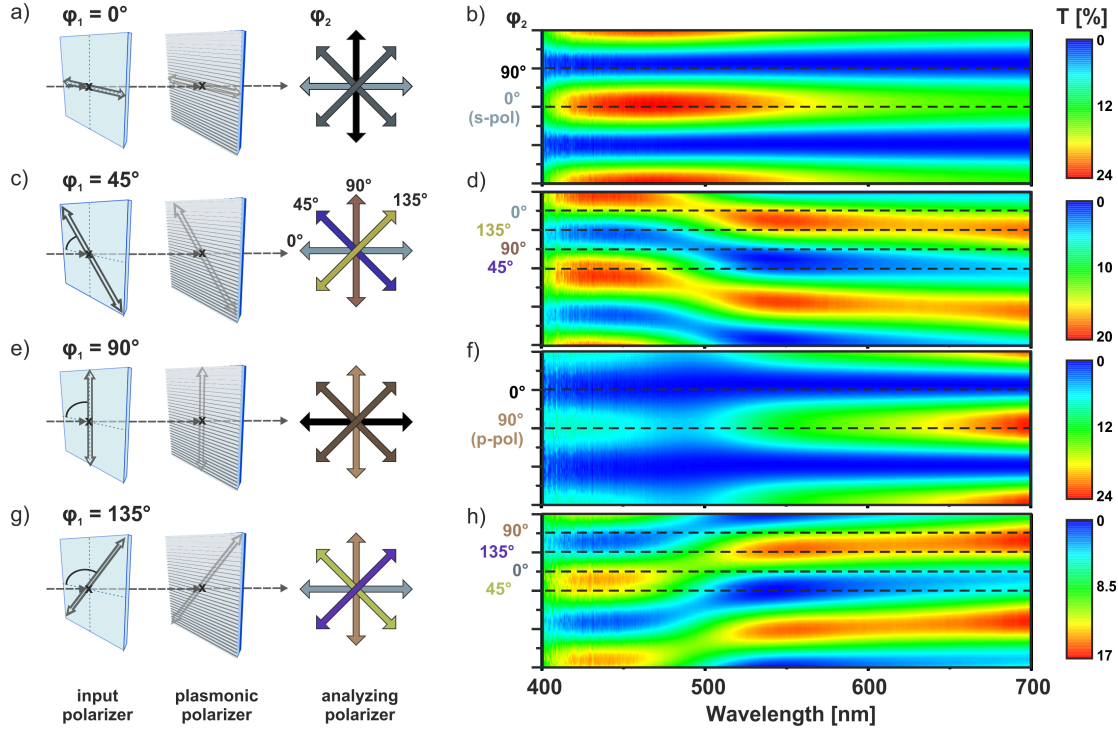
Figure 5.4 – Transmission spectra as a function of polarization angles. (left) Measurement schemes for different angles of the incident polarizer (φ_1) and the analyzing polarizer (φ_2), each output arrow is colored in the observed color (as in Figure 5.3d). (right) Corresponding transmission plots for rotation of the analyzing polarizer ($0° < \varphi_2 < 360°$, $1°$ steps).

polarization. Accordingly, if $\varphi_1 = \varphi_2$, the transmission is at a maximum, and if $\varphi_1 = \varphi_2 + 90°$, the transmission is zero (see Figure 5.4b,f). This trivial configuration can be described with two polarizers and a color filter in between. The situation is more intricate for diagonal input polarization ($\varphi_1 = 45°$ and $135°$). Here, s-pol and p-pol acquire a different phase shift that depends on the wavelength. The polarization state after the PPR is therefore elliptical and the orientation of the ellipse is a function of wavelength. Very different colors are therefore obtained for different settings of the analyzing polarizer (φ_2). Figure 5.4d,h show that the transmission spectra sensitively depend on the setting of φ_2. The total intensities are conserved but the maxima shift as φ_2 is varied. This is a clear indication of a phase shift. Similar results were observed for other plasmonic resonant systems.[300] The phase shift is responsible for the observation of four distinct output colors in the diagonal case ($\varphi_1 = 45°$ and $135°$); only one color is observed for each s-pol and p-pol ($\varphi_1 = 0°$ and $90°$).

The transmission spectra shown in Figure 5.4 can be described with the knowledge of the polarization states and the phase information, which can be formulated in terms of Jones Matrices.[309] The field transmitted through input polarizer, PPR, and analyzing polarizer is

$$E(\varphi_1, \varphi_2) = \begin{bmatrix} \cos^2 \varphi_2 & \sin \varphi_2 \cos \varphi_2 \\ \sin \varphi_2 \cos \varphi_2 & \sin^2 \varphi_2 \end{bmatrix} \begin{bmatrix} E_s e^{i\psi_s} & 0 \\ 0 & E_p e^{i\psi_p} \end{bmatrix} \begin{bmatrix} \cos \varphi_1 \\ \sin \varphi_1 \end{bmatrix} \quad (5.1)$$

$$\underbrace{\hspace{4cm}}_{\text{analyzing polarizer}} \quad \underbrace{\hspace{3cm}}_{\text{PPR}} \quad \underbrace{\hspace{1.5cm}}_{\text{input pol.}}$$

E_s and E_p are the field amplitudes of the s-pol and p-pol states, respectively, and ψ_s and ψ_p are the corresponding phases. The square modulus $|E|^2$ is proportional to the transmitted intensity and becomes

$$|E(\varphi_1, \varphi_2)|^2 = \{(E_s \cos \varphi_1 \cos \varphi_2 \cos \psi_s + E_p \sin \varphi_1 \sin \varphi_2 \cos \psi_p)^2$$
$$+ (E_s \cos \varphi_1 \cos \varphi_2 \sin \psi_s + E_p \sin \varphi_1 \sin \varphi_2 \sin \psi_p)^2\} \quad (5.2)$$

This formula describes all the measured states in Figure 5.4 and requires only the intensity of the incident polarized light and the corresponding phase shift caused by the PPR. For $\varphi_1 = 0°$ or 90°, the two orthogonal states s-pol and p-pol are obtained; whereas for $\varphi_1 = 45°$ or 135°, there are four different states due to the phases ψ_s and ψ_p.

5.2.5   Computation of the Phase

To understand the origin of the phase variations I performed electromagnetic field calculations using the surface integral equation method (SIE),[249] see Section 2.3.3. Figure 5.5a displays the simulated transmission spectra for s-pol and p-pol input states. The calculated spectra reproduce the measurements (Figure 5.3b), although the overall intensity is a factor of 3 lower in the measurements. The optical properties of silver can strongly suffer from gas or water residues during the evaporation process.[213] Further, silver "is susceptible to dewetting and grain-boundary pinning".[213] Smooth surfaces can be achieved using high evaporation rates and high vacuum conditions. However, the used vacuum is limited to $5 \cdot 10^{-6}$ mbar, and the evaporation rates cannot be increased without sacrificing process control. Nevertheless, both parameters can be optimized in the future. For example, I observed a transmission increase of ~15% when increasing the evaporation rates from 3 to 30 $\mathring{A}/s$. This increase caused only a small shift of the spectra and consequently the same color was observed. Therefore, the fabrication conditions are not critical for achieving the color effects described here; they mainly affect the overall transmission. It should be noted that absorption of the UV-curable polymer in the blue leads to a decrease of the transmission for wavelengths shorter than ~430 nm, see Figure 5.3b,d.
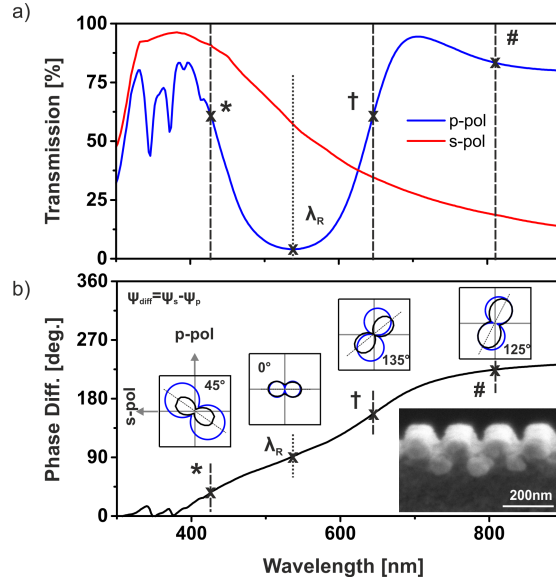
Figure 5.5 – Theoretical analysis of the plasmonic color filter. (a) Calculated transmission spectra for s-pol and p-pol. (b) Corresponding phase difference between s-pol and p-pol. The insets indicate the angle-dependent intensity distribution of the output (as a function of φ_2, *cf.* Figure 5.3c,d). The SEM image shows the fabricated structure prior embedding.

With the help of SIE one can determine the optical parameters, that is, the amplitudes E_s, E_p, and the phases ψ_p and ψ_s. These parameters can also be determined by fitting Equation 5.2 to the measured transmission spectra (Figure 5.4). As shown in Figure 5.5b, the calculated phase difference $\psi_{diff} = \psi_p - \psi_s$ shows a pronounced increase ($\sim 180°$) near the plasmon resonance. The insets in Figure 5.5b show the transmitted intensity as a function of the output angle φ_2 for wavelengths below (*), at (λ_R), above (†), and far above (#) the plasmon resonance. The blue curves are calculations and the black curves are measurements (intensity multiplied by 3). A slight deviation between theory and measurement is observed just above the resonance (†), which is caused by a slightly broader LSPR resonance in the simulations. The angles in the insets indicate the angles for which the measured transmitted intensity is highest.

5.2.6 Near-field Intensity and Charge Distribution

To further investigate the provenance of the phase shift, I calculated the electromagnetic near-field and electric charge distribution for different wavelengths (Figure 5.6). Below the resonance (*) the electric field is localized near the upper layer of nanowires, as well as between the nanowires; it appears as if the light "funnels" through the nanowires (Figure 5.6a). In this regime the wavelength is too short to resonantly excite plasmons on the nanowires. At the
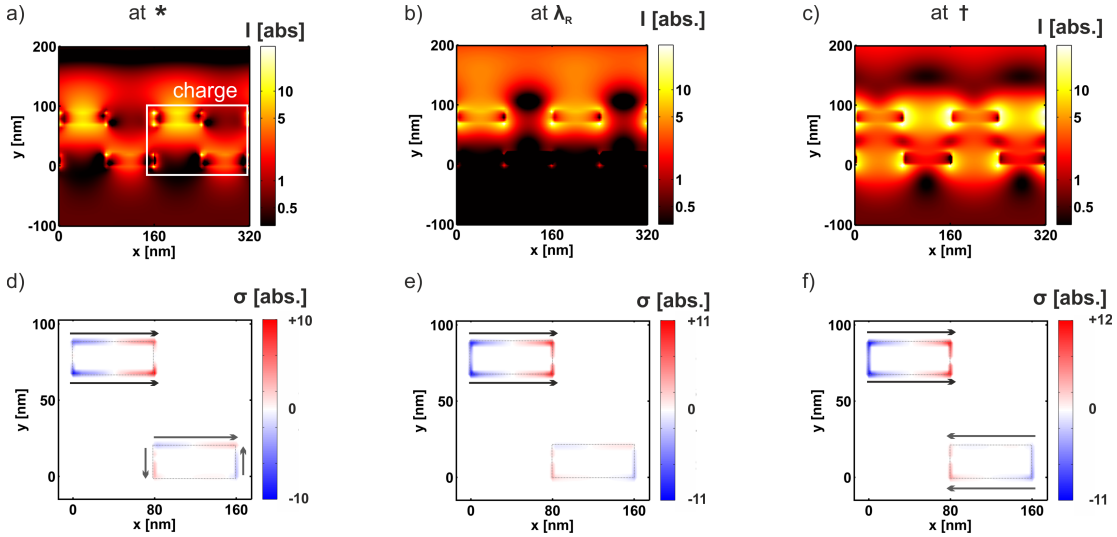
Figure 5.6 – (a-c) show the near-field and charge density respectively of the nanowires at the points indicated in Figure 5.5a,b. The black arrows indicate the direction of the electron flow at a given time. The black dashed lines outline the geometry of the simulated structure.

LSPR wavelength (λ_R) most light is reflected by the upper layer of nanowires (Figure 5.6b). At even longer wavelengths (†), the resonance condition is no longer fulfilled and the transmission increases (Figure 5.6c). The computations show that the LSPR moves the region of highest field enhancement from inside the nanowires to in-between the nanowires. Correspondingly, the distribution of charge shows a sign change (see Figure 5.6d-f). Below the resonance a high charge density is present within the upper layer of nanowires, with the black arrows indicating the direction at a given time. At resonance a high charge density is present mainly in the upper layer, consistent with the near-field enhancement. Beyond the resonance the charge density of the upper and lower layer of nanowires are opposing each other. Overall the calculated electromagnetic near-field and the electric charge distribution both show a clear change around the plasmon resonance. Similar effects near LSPR's have been reported in the literature before. [278,301]

5.2.7 Geometrical Influence on the Resonance

In a next step, I studied the influence of geometric parameters, such as the etching depth (vertical separation between nanowire layers) and the thickness of the nanowires. Figure 5.7a,b show the corresponding simulated transmission plots for p-polarized light. These simulations were carried out using rigorous coupled-wave analysis (RCWA), [250] see Section 2.3.3. The lines in Figure 5.7a show the location of two modes, one being the LSPR (dashed) and a second (dot-dashed) that depends on the in-plane interaction between the nanowires. This second mode shifts to higher

energy for decreasing depth, which is an indication for a quadruple mode. For depths larger than 90 nm, the two layers of nanowires are sufficiently separated, and their interaction can be neglected. Experimentally I have verified this effect with nanostructures having a depth of 70 and 90 nm. Combining the effects of different silver nanowire thicknesses (see Figure 5.7b) with different nanostructures depths yields a wide range of distinct colors, spanning the complete visible range excited by s-pol and p-pol light (see Figure 5.7c).
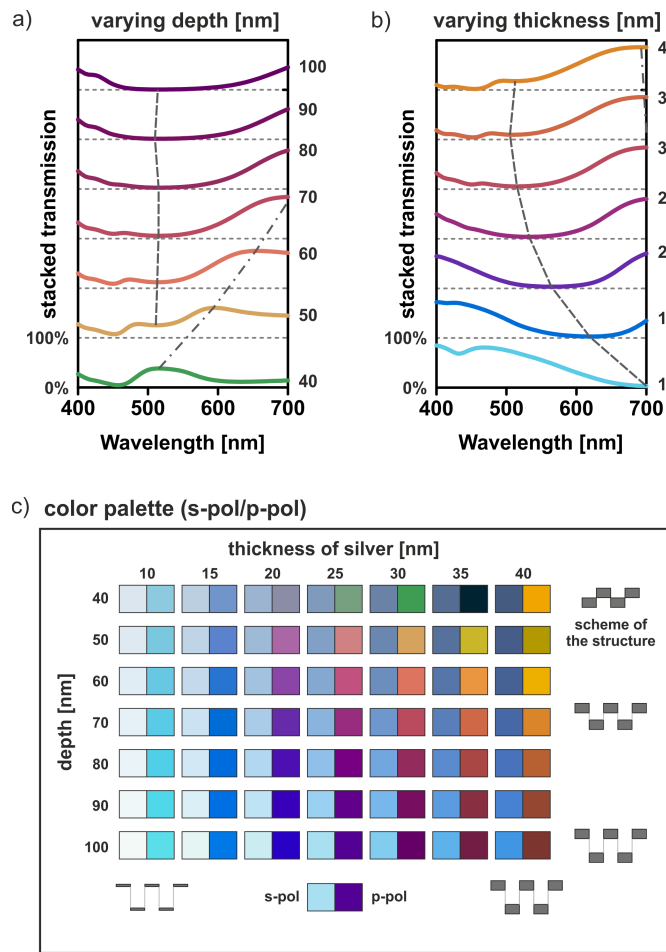
Figure 5.7 – Calculated transmission spectra for p-polarized light and for (a) different periodic nanostructures depths (using 30 nm silver) and (b) different silver thicknesses (using a depth of 70 nm). The LSPR (dashed) mainly depends on the thickness of the silver, whereas a second mode (dot-dashed) is mainly influenced by the nanostructure depth. (c) Simulated color map of s-pol and p-pol colors for varying depth and silver thickness. The illustrations qualitatively indicate the arrangements. The spectra and color palette are colored in the computed transmission color.

5.2.8 Large-Scale Realization and Color Generation

Figure 5.8a,b shows images of Marilyn Monroe ("Marilyn Diptych" by Andi Warhole, 1962) and an exemplary CIE xyY color plot (CIE 1931 color space).[291] This Marilyn Monroe image was one of the first commercial large-scale productions of art made by silkscreen. The images in Figure 5.8a were recorded with a diagonal input polarizer (*cf.* Figure 5.3c) and different settings of the output polarizer. The CIE color plot, displaying sample of Figure 5.3, shows four distinct states and intermediate colors (bold line), with 0° and 90° denoting s-pol and p-pol, respectively (Figure 5.8b). The intermediate colors (45° and 135°) show a very strong contrast. These appear in Figure 5.8a as purple/dark blue and orange/yellow. The colors span a wide range of the standard RGB color space (sRGB). The photomask that I used to generate the image has five regions, corresponding to different evaporation thicknesses (see Figure 5.8c; face∼15 nm, background∼20 nm, hair∼26 nm, lips∼30 nm and black parts∼80 nm. To further enhance the optical appearance an analyzing polarizer was designed with two opposing regions (Figure 5.8c). Finally Figure 5.8d,e shows the influence of the proposed phase shift on the color effect. Here the same sample as in Figure 5.8a,b is utilized, but there is no additional analyzing polarizer as described in Figure 5.3a. Clearly the color generation for the individual images is not as distinct and the high contrast colors are missing (see CIE plot). This confirms the significance of the phase shift for high contrast and vivid color generation.

5.3 Discussion

The color appearance depends mainly on two parameters: the spectra of the s-pol and p-pol states defining the basic colors (Figure 5.7c) and the spectral position of the LSPR, defining the intersection between the two intermediate spectra (Figure 5.3c). By appropriate choice of the nanowire geometry these parameters can be tuned to yield the ellipse in the CIE xyY color plot shown in Figure 5.8b. The size of the ellipse determines the contrast of the colors. For the geometry used in this chapter, the contrast is highest when the LSPR is located in the middle of the visible spectrum ($\lambda \sim 450 - 550$ nm); This was best fulfilled with using silver. Other materials are interesting as well and yield different basic colors. I also fabricated samples with gold and aluminum and varied the thicknesses of these nanowires. Using the measurement configuration of Figure 5.3c four distinct colors are obtained; but often for the human eye, they do not show a strong contrast. Nevertheless, these materials are interesting to potentially increase the color palette, for example, green by using gold. Evaporation of different materials
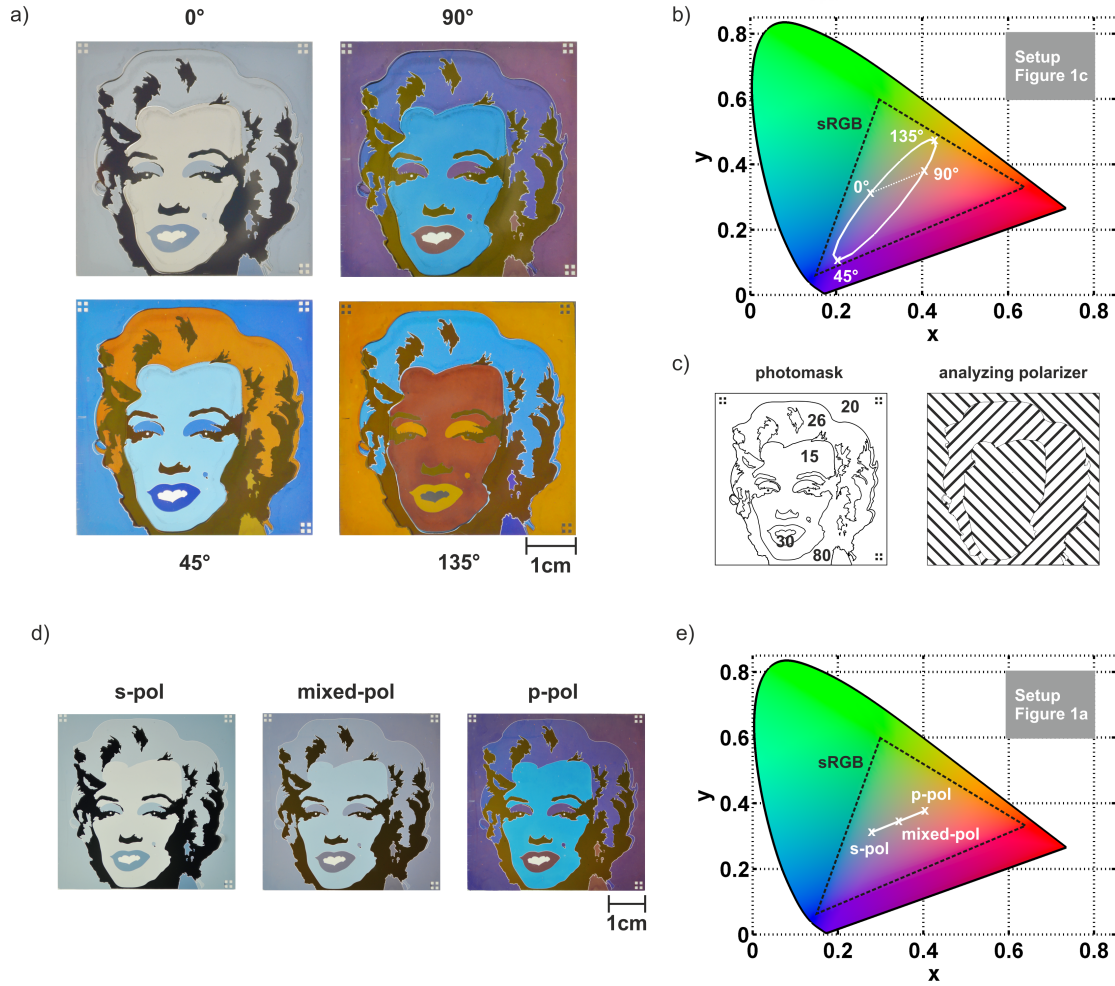
Figure 5.8 – Color rendering and image formation. (a) Images of Marylin Monroe for four different analyzing polarizer settings (angle φ_2 is indicated) by using the measurement scheme of Figure 5.3c (diagonal input polarization). (b) Corresponding measured colors are displayed in a CIE color plot. (c) Illustration of the mask consisting of five regions for different silver thicknesses and the analyzing polarizer. (d) Images and (e) color plot of the sample used for (a,b), but by utilizing the measurement setup of Figure 5.3a. Derived from Original Artwork by Andy Warhol ©, The Andy Warhol Foundation for the Visual Arts, Inc. / 2015, ProLitteris, Zurich.

onto periodic nanostructures can lead to an optical color filter spanning the complete visible spectrum.

Overall the proposed silver nanowires (period: 160 nm, depth: 70 nm, silver: 10-30 nm) and the configuration shown in Figure 5.8c were used for the following reasons. First, silver exhibits a pronounced resonance in the visible spectrum. Second, the geometry is simple, enabling large-scale fabrication and no implications for roll-to-roll manufacturing, see Section 2.3.2. Third, the fabricated structures are embedded, enabling use in ambient conditions. And fourth, a period of 160-180 nm shows a largely angle-independent behavior. Therefore, tilting the sample (up to $\sim 60°$) in any direction renders the same color appearance (see Figure 5.2), which is essential for usage in diffuse or poor light conditions. Consequently, this property of the proposed zero order effect clearly differs from analog diffractive grating effects, see Section 2.1.1. Finally the utilized phase shift enables high contrast colors.

5.4 Conclusion

In summary, a fourfold plasmonic color filter based on periodic silver nanowires is presented. By rotation of an analyzing polarizer four distinct output colors and their intermediate states can be displayed. The wavelength-dependent transmission through the polarizer is a feature of the phase retardation of the plasmonic substrate. The underlying phase shift is induced by the plasmon resonance and results in high contrast colors. The palette of appearing colors can be enhanced by appropriate tuning of the fabrication process leading to geometrical variance of the nanowires. Angle- and orientation stability of the transmitted color is granted by choosing an appropriate period of the nanowires enabling easy use in even diffuse light conditions. The complete fabrication process can be integrated in a large-scale roll-to-roll process; the final device is designed such that it can be used at ambient conditions. Additionally, polarized light sources such as displays or smart phones can act as output polarizers enabling multiple and practical applications. Extending the nanowire based structures to 2D periodic structures, permitting two plasmon resonances simultaneously, can further increase the contrast of the observed colors,[179,300] see Section 2.2. Aside from active color filtering, *e.g.* for polarizing screens,[297] these structures could potentially be used as a valuable resource for security applications,[63,268] magneto-optic retarders (chromatic waveplates),[310] polarizing detectors (*e.g.* polarization microscopy)[153] and sensing applications (*e.g.* refractive-index changes).[83]

5.5 Experimental Details

Fabrication

A periodic photoresist structure (4.7 cm x 4.7 cm) with a period of 160 nm and a duty cycle of 0.5 was obtained from e-beam lithography. Subsequently a nickel shim was grown through a galvanic process to serve as a master structure (160 nm period, 70 nm depth). Replication was done in a UV curable polymer onto a glass substrate. After the curing process, 10-40 nm of silver was thermally evaporated onto the sample at $5 \cdot 10^{-6}$ mbar and 3 $\mathring{A}/s$. Subsequently the structure was embedding with the UV curable polymer and a glass substrate.

Characterization

The transmission measurements were done with an Ocean Optics spectrometer (HR4000CG) with the sample fixed after a Glenn-Thomson polarizer and the light source. A secondary polarizer was fixed on an automatic rotation stage for the transmission spectra (Figure 5.4). A Perkin Elmer spectrometer (Lambda 9) was used to determine the transmission spectra for different tilt angles. The size of the illumination spot was each about 3x3 mm, the measured samples were about 4.7 cm x 4.7 cm. The measured transmission values were transferred into RGB values (D65 illuminant) with a home-made MATLAB (version 2015) script.

Computations

Near-field computations with the corresponding phase and charge density information were done with SIE.[249] First far-field zero order transmission spectra were computed (300 nm to 900 nm, 0.5 nm step). The corresponding phase of the two polarized states and the difference could be evaluated directly. Secondly near-field maps of the structure (see Figure 5.6) at the indicated wavelengths (see Figure 5.5) were done (precision of 0.5 nm). The intensity is plotted logarithmically. Third the charge density of the structure at the indicated wavelengths and at a given time was computed. Far-field computations were done with RCWA from 400-700 nm, in 0.5 nm steps for p-polarized light (see Figure 5.7). Computations were done for different depths of the structure (40-100 nm), different thicknesses of the silver (10-40 nm), different periods (not shown) and different materials (not shown).

Artwork Sample

An original artwork by Andy Warhol was used to create a simplified model of Marilyn Monroe. This served as a basis for several photomasks. Each outline depicted in Figure 5.8c shows a region with different silver thicknesses. Evaporation was done subsequently after exposure of

64

the photoresist through the mask in a mask aligner (MA/BA6, SUSS MicroTec). Finally the substrate was embedded and an analyzing polarizer was designed as proposed in Figure 5.8c. The photographs were done with a digital single-lens reflex camera (DSLR) and by placing the sample onto the analyzing polarizer. Subsequent rotation of a polarizer led to the four distinct images.

6 Multispectral Imaging with Tunable Plasmonic Filters
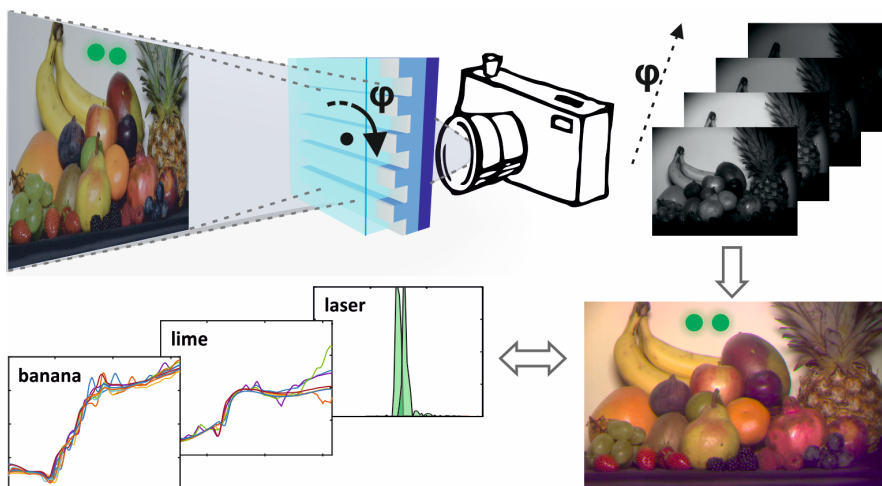
I present an angle-insensitive, miniaturized and integratable filtering system based on plasmonic substrates for multispectral imaging. Active tunability of the plasmonic filter allows color recording, estimation of unknown spectra and determination of spectral singularities, *e.g.* laser lines, while exploiting the full spatial resolution of a B/W conventional camera. Compared to other multispectral imaging systems, the plasmonic filtering system can be placed in front of an existing imaging system *e.g.* including lenses, supporting a cost-efficient fabrication and integration. Additionally, it is characterized by high angular acceptance, which I demonstrate by imaging with a field-of-view of $\sim 50°$. Further the number of non-pixelated broadband filters could be varied in situ for faster imaging or higher quality, compared to systems with a fixed number of channels.

This chapter is "adapted with permission from L. Duempelmann, B. Gallinet, & L. Novotny; Multispectral Imaging with Tunable Plasmonic Filters. *ACS Photonics* **4** (2), 236-241 (2017). Copyright 2017 American Chemical Society."

6.1   Introduction

Currently the demand for imaging systems providing spectral analysis is strongly increasing.[72,311] Recent markets include remote sensing,[312] food monitoring,[313,314] medical monitoring[315,316] or art conservation.[317] A diversity of instruments with unique performance is already available.[i] Each of these techniques has its advantages and drawbacks, providing solutions mostly for niche applications. Important performance characteristics are the spectral, spatial and temporal resolution. The field-of-view (FOV) defines the angular range that can be recorded by the camera. Finally the bulkiness, handling and expense are practical characteristics that strongly limit the range of applications.

The recording of the hyper- (>10 bands) or multispectral data can be done by spectral scanning (*e.g.* tunable filters[318] or liquid crystal tunable filters[319]) or spatial scanning (*e.g.* gratings[87]), see Figure 6.1a,b. This often requires bulky and heavy parts or significant volume for spectral filtering. Alternatively the spectral data can be recorded instantaneously (snapshot),[320] at the expense of spectral or spatial resolution (*e.g.* multispectral filter array[321,322] or filtered lenslet array[323]), see Figure 6.1c. Such systems are typically part of an imaging system (see gray box) and cannot be integrated into or combined with other existing systems. Furthermore, these "snapshot systems" often make use of interferometric filters that strongly depend on the incident angle, thereby reducing the FOV.[320,322,324] Also, the spectral resolution depends on the number of pixels or lines with different spectral filtering properties (filter array), which leads to increased complexity and cost of fabrication.[318,320,322] On the other hand, spectral imaging systems based on liquid crystal tunable filters and filtered lenslet arrays are often complex, sensitive and expensive.[319,323]

There is great demand for miniaturized, cost-efficient, and integratable multispectral imaging systems.[72,325] Such systems can be realized, for example, with tunable broadband filters with angle-insensitive transmission properties.[326,327] Recently systems based on colloidal quantum dots,[326] vertical silicon nanowires[328] and plasmonics filter patches[166,173,327] were presented. Generally in these realizations each pixel is addressed by a single filter, which limits the

---

[i]*e.g.* the research institute IMEC (imec.be) developing hyperspectral imaging cameras or the Swiss startup Gamaya (gamaya.com) utilizing hyperspectral cameras for remote sensing. Accessed 04.01.2017
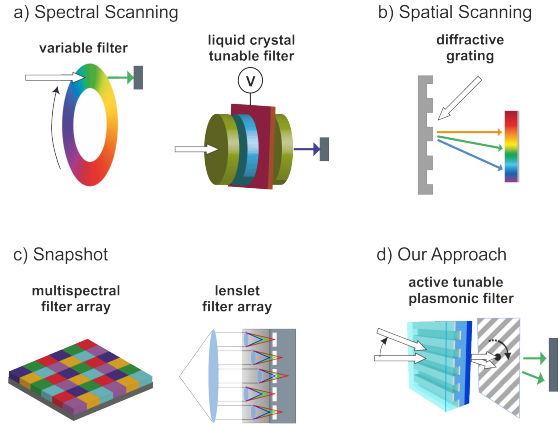
Figure 6.1 – Overview of current methods for multi- and hyperspectral imaging: (a) spectral scanning while acquiring images, (b) spatial scanning (line- or point-wise) while recording spectra and (c) obtaining an image with spectral information in a single snapshot. (d) Shows a scheme of the active tunable plasmonic filter, indicating the angle-stability, compactness of tuning and adaptability to imaging systems (gray box).

spatial resolution and increases the fabrication complexity.

Here a plasmonic multispectral imaging (PMSI) system based on active tunable plasmonic filters (TPF) is presented. These filters can be used as add-ons to existing commercial imaging systems (*e.g.* B/W or RGB camera). The working principle of TPFs is similar to variable filters, with the difference that the filter properties can be tuned by the polarization and not the structure itself (see Figure 6.1d). This leads to higher compactness and lower fabrication costs. Furthermore it is designed to be nearly completely angle-insensitive in all directions, enabling a high FOV of $\sim 50°$. The thickness of the plasmonic filters is in the range of a few micrometers, making them attractive for miniaturized systems. Furthermore, the filters are lightweight and robust. Similar plasmonic filters often suffer from structural and fabrication complexity, angle-sensitivity and limited active tunability.[147,153,306] They also maintain the full spatial resolution and are cost-efficient, which sets them apart from snapshot systems. Compared to spectral estimation using RGB cameras no prior knowledge of the spectral reflectance or analysis of training samples is required.[324,329]
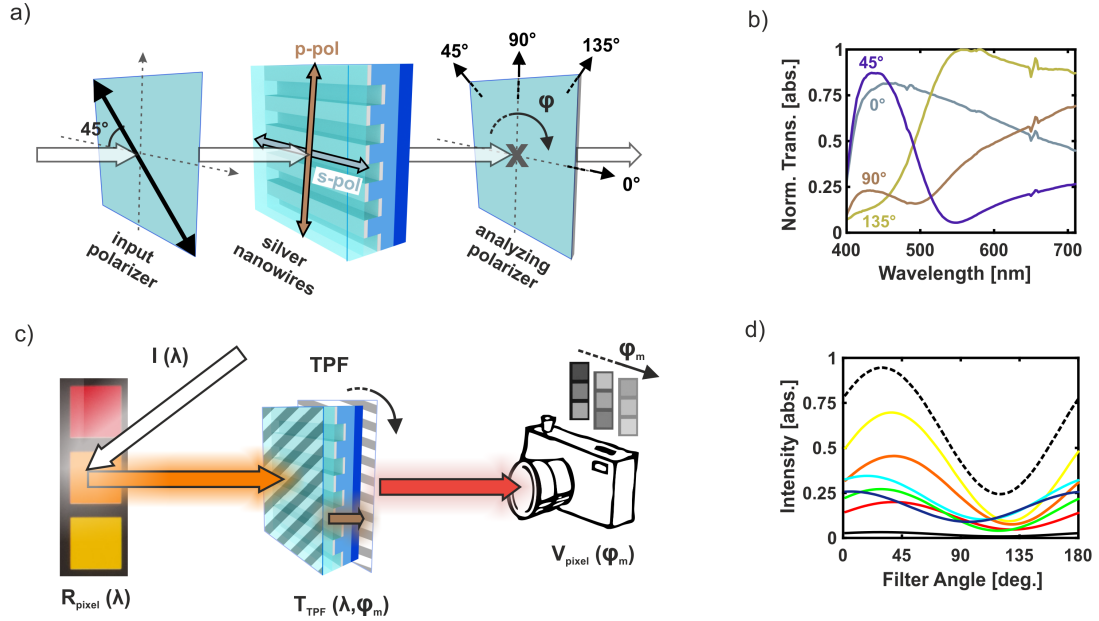
Figure 6.2 – (a) Operating principle of active tunable plasmonic filters (TPFs). Diagonally polarized light passes through the plasmonic structure as s- and p-polarized light and is then analyzed by rotation of a subsequent polarizer (angle in bold). (b) Normalized transmission spectra of the TPF illustrated in (a). (c) Plasmonic multispectral imaging (PMSI). An illuminant (I) is reflected by a target (R_{pixel}). The reflected light passes through the TPF at an angle (φ_m) and is recorded by a camera that renders an intensity image (V_{pixel}). The colored arrows indicate the chromatic change of light. (d) The intensity of different colored patches (indicated by their real colors, white is dashed) of a ColorChecker (V_{pixel}) at different filter angles (φ_m).

6.2 Results and Discussion

6.2.1 Operation Principle

The TPF was fabricated as described in Chapter 5. The nanostructures have a period of 160 nm, a depth of 70 nm and a thin layer of silver of 30 nm. A fabrication scheme is shown in Figure 5.1. The plasmonic substrate is finally placed between two polarizers; an input polarizer fixed at 45° to the silver nanowires and an analyzing polarizer which can be rotated, see Figure 6.2a. Light transmitted through the input polarizer can be described as a combination of s- and p-polarized light incident on the sample (field of incidence perpendicular to the nanowire lines). The p-polarized light excites a plasmon resonance, at which a wavelength-dependent phase shift is induced (see Chapter 5). Rotation of the subsequent analyzing polarizer (angles bold) leads to four main transmission spectra with a cross-over at the plasmon resonance and angular combinations thereof (see Figure 6.2b), more information in Chapter 5. The TPF has π-rotation symmetry and its transmission, $T_{TPF}(\lambda, \varphi)$, depends on the rotation angle φ of the

polarizer. The number of angle settings $\varphi_1, \cdots, \varphi_m, \cdots, \varphi_M$ defines the number of filters M.

6.2.2 Spectral Reconstruction
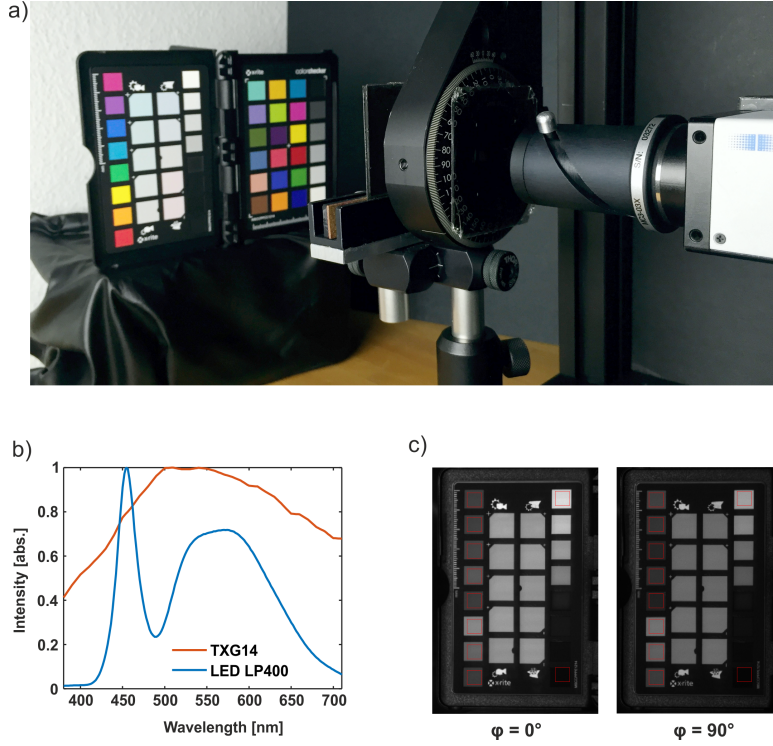
Figure 6.3 – (a) Photo of the PMSI including the B/W camera, the lens system, the variable polarizer mounted on a rotation stage, the plasmonic substrate with a fixed polarizer and the color checker board, from right to left. (b) Spectra of the LED light source (LP400) and the sensitivity of the B/W camera (TXG14). (c) Intensity images of the color checker board (see (a) left side) at different rotation angles $\varphi = 0°$ and $90°$ of the variable polarizer. Measurement areas are marked with red rectangles.

A scheme of the system is shown in Figure 6.2c; a corresponding photo of the real setup is given in Figure 6.3a. A source with spectrum $I(\lambda)$ illuminates the sample to be measured. The reflected light, with intensity $R_{pixel}(\lambda)$, transmits through the TPF with $T_{TPF}(\lambda, \varphi)$, before an intensity image, $V_{pixel}(\varphi)$, is recorded by a camera with a given sensitivity $S(\lambda)$, see Figure 6.3b. Figure 6.3c shows two photos of the color checker board (Figure 6.3a, left side), which are recorded at different angles. The red rectangles highlight the area, which was used to reconstruct the color. The intensity of the image is extracted for each pixel and used to reconstruct the spectral information of the observed object, see Figure 6.2d. In the following experiments a black and white (B/W) camera is used, but the formalism is also valid for multispectral cameras that feature multiple spectral sensitivities S. To calculate the reflected spectra (reconstruction)

the continuous spectral range λ is divided into N discrete regions. The recorded intensity of each pixel (V_{pixel}) can be approximated as a discrete function of the wavelength λ_n as

$$V_{pixel}(\varphi_m) = \sum_{n=1}^{N} S(\lambda_n) \cdot I(\lambda_n) \cdot T_{TPF}(\lambda_n, \varphi_m) \cdot R_{pixel}(\lambda_n) \qquad . \qquad (6.1)$$

Every image pixel (i,j) has its own value of V_{pixel} and R_{pixel}. S, I and T_{TPF} are the same for all pixels. They depend on the wavelength λ_n and the rotation angle of the filter φ_m and need to be evaluated only once for a given illuminant. The number of discrete frequency regions (N) defines the number of unknowns when solving for $R_{pixel}(\lambda_n)$. On the other hand, the number of filters (M), expressed by the discrete rotation angles $\varphi_1 \cdots \varphi_M$, determines the number of known variables. This leads to a linear system of equations $V_{pixel}(\varphi_m) = A(\lambda_n, \varphi_m) \cdot R_{pixel}(\lambda_n)$ with M known and N unknown variables. Solving this linear equation renders the spectrum $R_{pixel}(\lambda_n)$ for every image pixel. To solve for $R_{pixel}(\lambda_n)$ the linear least-squares approximation[330] is used. It minimizes the squared Euclidean norm of

$$\min_R \frac{1}{2} \| A(\lambda_n, \varphi_m) \cdot R_{pixel}(\lambda_n) - V_{pixel}(\varphi_m) \|^2 \qquad . \qquad (6.2)$$

If the matrix $A(\lambda_n, \varphi_m)$ had full rank, meaning that all the included filters are linearly independent from each other, the system of equations could be solved completely and with high accuracy. On the other hand, if a set of filters with low rank is used the solution can become inaccurate or unstable (its values oscillate),[331] especially if the system is disturbed by perturbations (*e.g.* noise). To evaluate the linear dependence of the filters, a singular value decomposition (SVD) of the matrix $A(\lambda_n, \varphi_m)$ has been performed. It shows that the first three eigenvalues yield the strongest contribution; the corresponding eigenvectors can reproduce the system nearly entirely. Thus, most colors can be reproduced with only three filters. However, reconstruction of spectra with singular features (*e.g.* laser lines) require a larger set of filters.

6.2.3 Number of required eigenvectors for reconstruction

To give an estimate on the number of necessary eigenvectors, a given spectra $R_{original}$ can be reproduced with a certain number of corresponding eigenvectors U of T_{PTF}:[332]

$$R_{reproduced} = U \cdot U' \cdot R_{original} \qquad . \qquad (6.3)$$

Figure 6.4 shows the root mean square (RMS) of the difference between $R_{reproduced}$ and $R_{original}$ of Equation 6.3 versus the number of eigenvectors used. The eigenvectors were used in decreasing independency order. The graph clearly shows that for color patches (*e.g.* MacBeth ColorChecker) mostly 3 eigenvectors is sufficient to achieve a small RMS, whereas for laser lines, especially the ones located further away from the plasmon resonance ($\sim$490 nm) a higher number of eigenvectors is required. Overall such a system should include as many eigenvectors as necessary, without losing spectral reproducibility, but also as little as possible to decrease complexity and speed of the solving algorithm. For comparison reasons, all spectral reconstructions were done with the same least-squares algorithm. Furthermore, for simplicity a large number of filters M greater or equal to the number of spectral regions N is taken. The results can be improved by principle component analysis[324,333] or by Wiener estimation,[329,334] which would additionally decrease the computation time. However, such optimizations are beyond the scope of this thesis. Further discussions about these methods as well as a comparison to RGB cameras are given in Section 6.2.7.
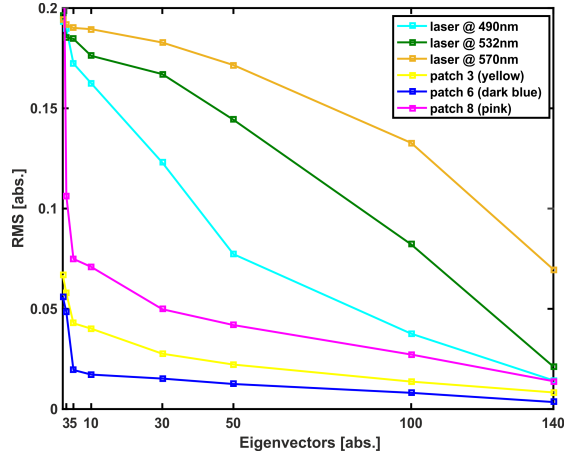
Figure 6.4 – The RMS compared to the number of eigenvectors. For colored patches the RMS decreases faster with less eigenvectors as for the laser lines, especially when the laser lines are located further away from the plasmon resonance ($\sim$490 nm).

6.2.4 Angle Dependent Measurements of Color Patches

As a test target a Macbeth ColorChecker is used. B/W images of colored patches are recorded using a commercial LED light source in combination with the PMSI. The reconstructed spectra are then compared with the spectra directly measured with a conventional spectrometer (see Figure 6.5). To analyze the FOV of the imaging system the analysis was done for tilt angles of $0°$, $15°$ and $25°$. For all these angles the reconstructed spectra reproduce the reference spectrum very
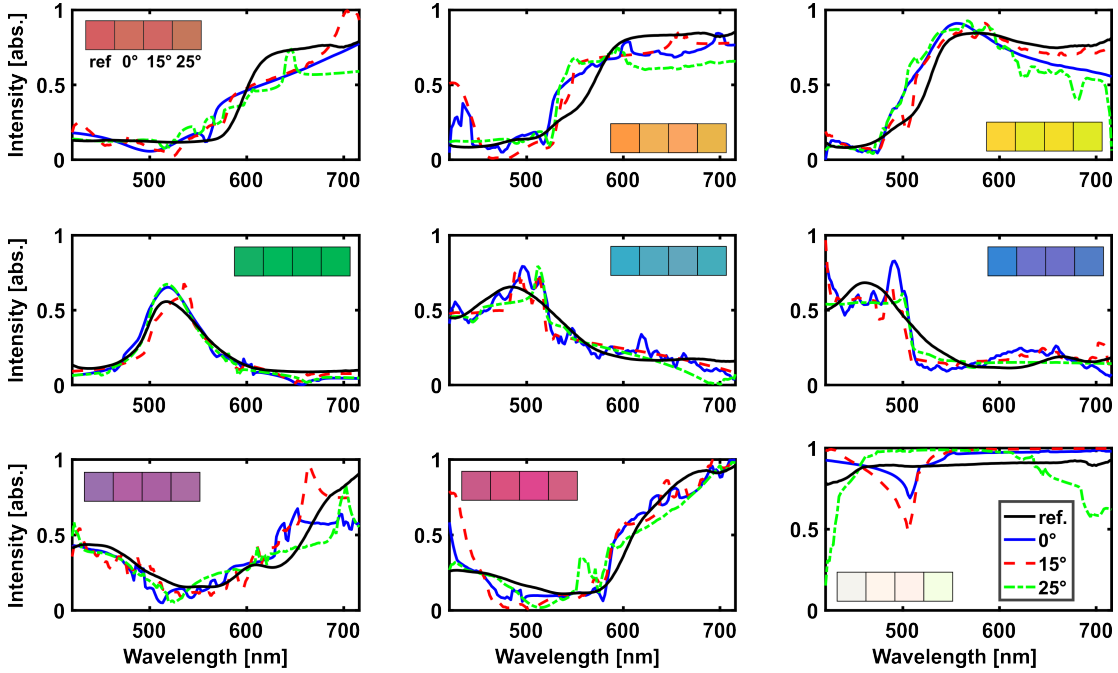
Figure 6.5 – Spectra of colored patches (Macbeth ColorChecker) recorded with a conventional spectrometer (ref.) and the PMSI using the TPF at tilt angles of 0°, 15° and 25°. The spectra are converted to colors (see insets). Here M=180, N=150.

well. The color representation (insets in Figure 6.5) is also excellent, even for large tilt angles. Residual deviations from the reference spectrum and oscillations in the spectra likely arise from the reconstruction procedure (also discussed by Bao *et al.*[326]) or from the linear dependence of the filters (see before). Overall the results indicate that the PMSI operates reliably for a wide range of angles, enabling acceptance angles of more than $\sim 50°$, which corresponds to a minimum f-number of f/1.07 (the range of conventional lenses). Table 6.1 gives an overview of the color difference (CIE ΔE 2000)[335] and corresponding RMS of the color patches at different tilt angles. Figure 6.6 shows a CIE xyY color plot (CIE 1931 color space)[291] including the angle-dependent measured colors of Figure 6.5.

6.2.5 Laser Line Measurements

To further characterize the spectral recording capabilities, the PMSI is utilized to measure laser light with different emission wavelengths. Some of the reconstructed laser lines are shown in Figure 6.7b. The reconstruction accuracy is influenced by the local minima and maxima of the filters (see Figure 6.7a), which determine the calculation of the eigenvectors of the system. This makes it possible to find a unique solution with a high spectral resolution within a certain

Table 6.1 – CIE ΔE 2000 and RMS values of the color patch measurements upon tilt angles of $0°$, $5°$ and $25°$.

Patch	CIE ΔE 2000			RMS		
	$0°$	$15°$	$25°$	$0°$	$15°$	$25°$
Red	5.1	1.5	10.9	0.1	0.1	0.12
orange	9.5	4.4	14.2	0.12	0.15	0.16
yellow	9.4	4.7	11.5	0.12	0.07	0.18
green	3.9	2	4.1	0.05	0.05	0.05
light blue	2.4	4.6	3.3	0.07	0.07	0.08
dark blue	14.1	14.8	4.5	0.11	0.09	0.06
purple	7.5	6.6	5.4	0.12	0.12	0.11
pink	3.8	5	3.5	0.09	0.15	0.1
black	3.6	3.5	4.5	0.01	0.01	0.01
white	7.2	11	8.6	0.07	0.12	0.15
Average	**6.7**	**5.8**	**7.1**	**0.09**	**0.09**	**0.1**
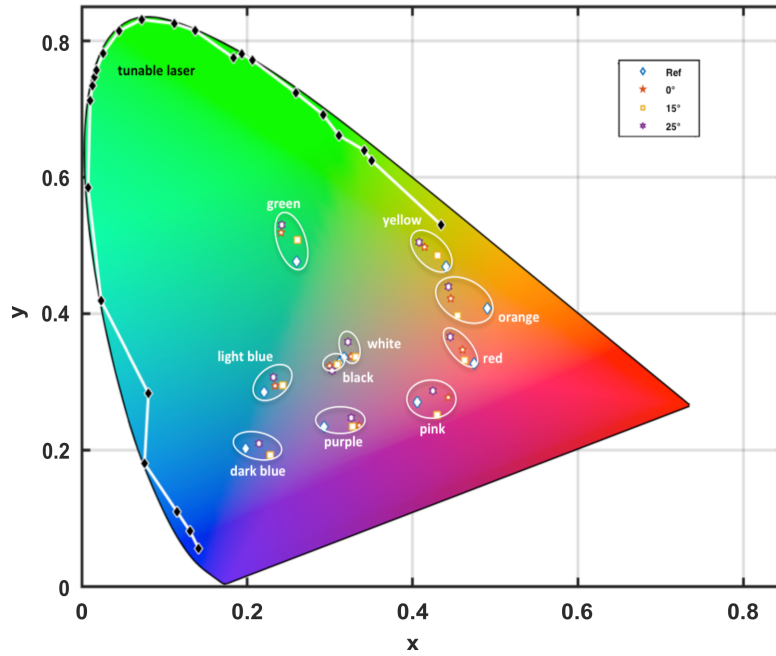
Figure 6.6 – CIE color plot including the measured samples. The white ellipse embrace each the same colored patch measured at different tilt angles including the reference. The black dots indicate the measured position of the laser, see section 6.2.5.
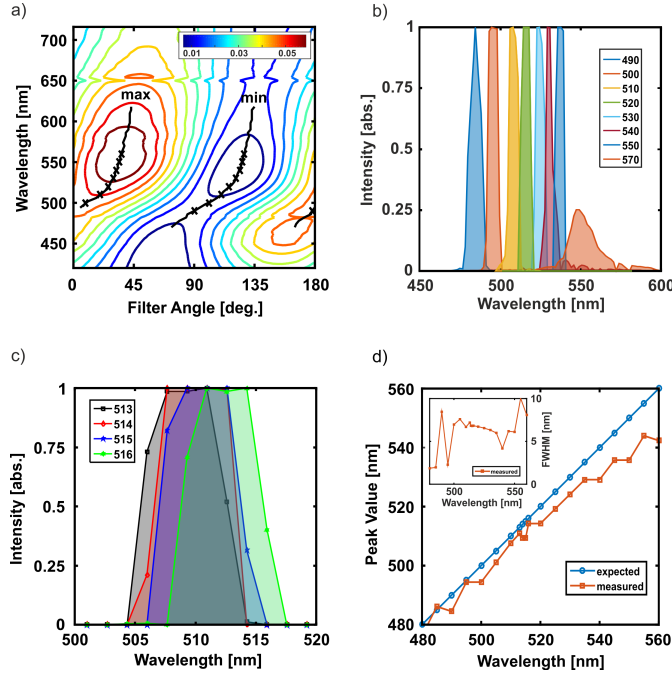
Figure 6.7 – (a) Contour plot of the transmission of the TPF multiplied with the camera sensitivity S. The black line in the plot represents the locii of minima and maxima. The crosses indicate the spectral positions of the laser lines that are measured and reconstructed in (b). (c) Spectral resolution accuracy shown for the laser lines of 513, 514, 515 and 516 nm. (d) Comparison of expected and reconstructed peak position of the laser lines (inset: corresponding FWHM). Here $M = 180$, $N = 180$.

wavelength range (*cf.* discussion on RMS, Figure 6.4). As shown in Figure 6.7c, the procedure is able to distinguish laser lines separated by 1 nm despite the fact that the filters are characterized with a spectral resolution of 2 nm. Figure 6.7d shows a comparison of the measured and expected laser peak position. The slight linear offset is likely caused by misalignment of the setup (*e.g.* polarizer position) or a wrong estimation of the sensitivity of the camera. To accurately determine the position and shape of spectral lines beyond the range of 480 nm to 570 nm, the setup (*e.g.* sensitivity of the camera or design of the filters) and algorithm (*e.g.* weighted least-squares) would have to be modified and improved. Figure 6.6 illustrates the position of the measured laser peaks in the CIE color plot.

6.2.6 Color Recording and Spectral Estimation of Object

Finally, imaging experiments are performed with the PMSI featuring a standard B/W camera (see Figure 6.8). Each pixel is assigned a spectrum $R_{pixel}(\lambda_n)$ (Figure 6.8c), which is converted to a color (Figure 6.8b). No further post-processing (*e.g.* white balance, gamma correction, etc.)
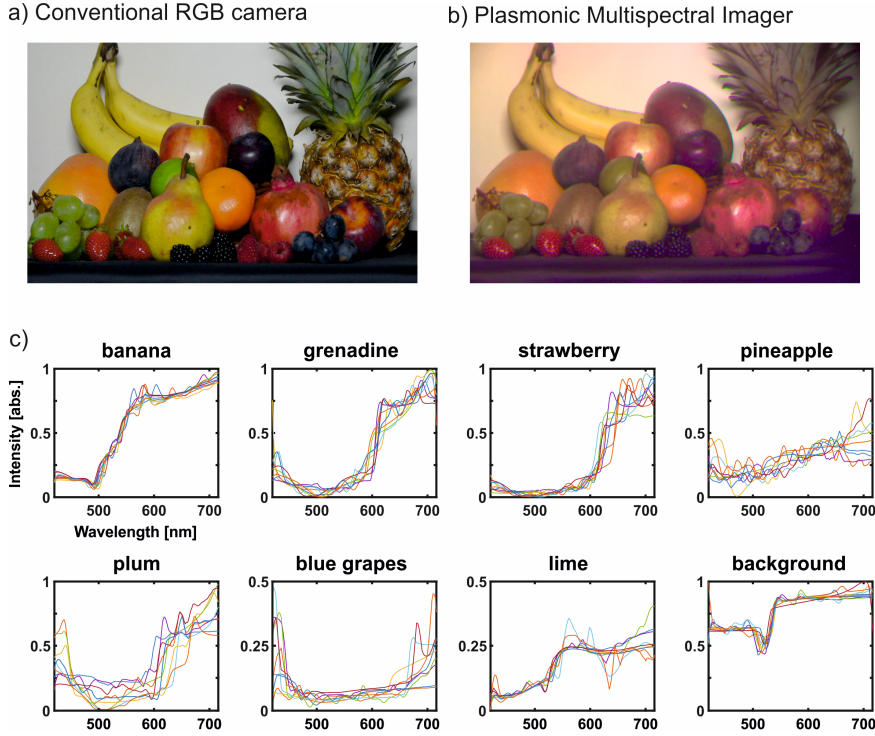
Figure 6.8 – A color image recorded by (a) a conventional RGB camera and (b) the PMSI. (c) Spectra of some of selected regions in the PMSI image. The different curves represent spectra evaluated at neighboring pixels.

is applied. While the colors of the fruits are reconstructed very well, the white background in the image features a yellowish tint, which could originate from poor estimation of the illumination source and which could be eliminated by simple calibration. To reduce the computation time, the resolution of the image was decreased by a factor 3. The spatial resolution is related to the unit cell size of the camera (here: 6.45 μm x 6.45 μm). The proposed method is based on zero order transmission and does not have color cross-talk, allowing to use smaller unit cells.[72] However, investigation of the spatial resolution limit is beyond the scope of this thesis.

6.2.7 Comparison to RGB imaging systems

Most common and cost-efficient imaging systems contain only few channels. There are several existing algorithms to estimate higher dimensional spectra out of limited data. Most of the methods require prior spectral analysis to optimize the set of filters or to more accurately reconstruct a subsampled stimulus.[324] The most popular algorithms are principle component analysis and Wiener estimation. They are based on reducing the dimension of training samples and using the eigenvectors for reconstruction[333] or constructing a transform matrix for reproduction of

training samples,[334] respectively. Such systems can be very versatile for spectral reconstruction, but unfortunately require prior knowledge about the spectral reflectance of the sample or training samples, which limits the usability and range of applications. Several improvements were made to optimize the reconstruction accuracy and time, but they are often optimized for certain problems.[329,336–339]

Overall the proposed PMSI has similarities to other multi-channel imaging system, *e.g.* RGB camera. Even though it has a high number of possible filters, it mainly consists out of 3 independent filters (eigenvectors) similar to an RGB system. This limits the resolution of the spectral reconstruction. Nevertheless more filters can be useful because: a) spectral reconstruction can be done directly and not by using an estimation algorithm (*e.g.* Wiener estimation) requiring training samples, b) depending on the measured reflection, the system is solved by distinct eigenvectors, enabling detection of *e.g.* spectral singularities (see Figure 6.4), c) they reduce random noise, leading to a more stable solution during reconstruction. Here the filters are mounted before the camera system, which in contrast to *e.g.* RGB camera enables recording of images at full spatial resolution. This enables adaptive exchange of the filter or combination with existing (multispectral) camera system to increase the number of eigenvectors. It is important to note that already 5-8 eigenvectors are sufficient to spectrally reproduce artworks or *e.g.* 1269 Munsell chips[324,331] with a relative high accuracy.
In contrast to other multispectral systems the number of filters (and recording time) can be selected actively depending on the applications (spectral vs. temporal resolution). Finally, RGB filters are designed for colorimetric measurements; the filters are separated to be linear independent and overlap for *e.g.* color filter array interpolation (so-called demosaicing).[340,341] The here proposed filters have a high spectral overlap; this could be beneficial for accurate detection of spectral features, whereas a higher number of filter could be required for accurate colorimetric measurements.

6.3 Conclusion

In summary, I present a functional multispectral imaging system based on active tunable plasmonic filters and a commercially available black/white camera. The recording of colored objects and laser lines at full spatial resolution and without prior knowledge is demonstrated. This includes an estimation of the spectra for each pixel, capable of distinguishing two laser lines separated by 1 nm. The multispectral imaging system is largely angle-insensitive, allowing to record images and spectra with a FOV of $\sim 50°$. The homogeneous and non-pixelated plasmonic filters

can be fabricated with standard roll-to-roll techniques, enabling cost-effective manufacturing for a wide range of applications.

The spectral resolution and dynamic range could by improved if a camera with multispectral arrays (*e.g.* RGB camera) were used. The number of used filters, as well as the spectral estimation algorithm, could be adapted *in situ* depending on the kind of application, *e.g.* analysis of artworks, remote sensing, etc. To cover other spectral ranges (*e.g.* infrared) one can adapt and optimize the plasmonic structures. A variety of such plasmonic structures could be designed as filter arrays to increase the spectral resolution or to use the camera in single-shot imaging mode. Besides a high FOV and low fabrication cost, such a multispectral filter array would strongly decrease the recording time. Also, the rotating polarizer can be replaced by an electrically tunable liquid crystal, which would facilitate the integration into miniaturized and lightweight systems, *e.g.* lab-on-a-chip applications. Further development of the solving algorithm can also greatly enhance the spectral resolution of the system. This could include a correction/calibration matrix, appropriate boundary conditions or databases of known substrates.

6.4 Experimental Details

Fabrication and Arrangement of the Plasmonic Tunable Filter

After fabrication of the plasmonic filter (more information see Chapter 5), a wire grid polarizer (ITOS, XP44) was glued diagonally to the nanowires onto the sample. This substrate was then fixed onto a holder just in front of an automatic rotation stage (Thorlabs, PRM1/MZ8) containing a wire grid polarizer (ITOS, XP44). Rotation of this polarizer enabled different transmission spectra of the active tunable plasmonic filter (TPF).

Measurement Setup

The TPF was characterized by direct illumination of collimated light (Dörr, LP400) and a spectrometer (Photoresearch, SpectraScan 735). A transmission spectra was recorded each 1° and calibrated by the measured light source. The maximum transmission through the used TPF was 0.064, by which the transmission spectra were normalized. For image recording, the plasmonic filter was mounted in front of a black/white camera (Baumer TXG14, silicon sensor) with configurable macro lens (Opto Engineering, MC3-03X). The setup was facing an object at a distance of about 50 cm, which was illuminated with a LED screen (Dörr, LP400). Images were recorded with a homemade LabVIEW (version 2015) script, while controlling the filter angle.

To compare the accuracy of the spectral reconstruction, the colored patches of the Macbeth ColorChecker (X-Rite) were measured with the spectrometer directly.

Reconstruction Software

The recorded images were imported in a homemade MATLAB (version 2016) script. The intensity of the pixels of interest were extracted correspondingly for each used filter angle. For analyzing the color patches an average of 100x100 pixels was taken. Additionally, the measured spectra of the TPF and light source, and the sensitivity of the camera has to be imported. For simplicity reasons a linear intensity-response behavior of the camera sensor was assumed. Then MATLAB (version 2016) was used to perform an iterative least-squares fit (command: "lsqlin", see `https://ch.mathworks.com/help/optim/ug/lsqlin.html`[ii]) with boundary conditions of a certain wavelength range scaling. The solution was limited to positive values only, with the upper boundary limiting it to physical useful values. A smoothness filter (command: "smooth", `https://ch.mathworks.com/help/curvefit/smooth.html`[iii], moving average: 5) was applied to the reconstructed spectra to reduce oscillation effects arising from the ill-condition problem. The resulting spectra were converting into RGB values (CIE 1931 color space, homemade MATLAB script), which were then plotted as color image.

Imaging Experiment

The reconstruction was done with the same parameters as the measurement of the ColorChecker. To reduce computation time of the not optimized algorithm the image was reconstructed by averaging 3x3 adjacent pixels of the recorded image leading to a final image resolution of 434x267 pixels. The sample was illuminated with the LED screen (Dörr, LP400) at a certain distance to assure homogenous illumination. An exposure time of 3 seconds was used.

Laser Measurements

A tunable laser (NKT Photonics, SuperK EXW-12) was used to illuminate a scattering white surface (Thorlabs, EDU-VS1). The images thereof were recorded and by using the same algorithm as before, the laser lines were reconstructed.

[ii]accessed 22.11.2016

[iii]accessed 22.11.2016

7 Conclusion and Outlook

7.1 Conclusion

To date only few plasmonic devices have made their way into consumer products. The limited surface area, the complex fabrication methods, the high cost of material, and the sensitivity of the structures to ambient conditions have often been hindering. To circumvent such limiting factors, the methods used in this thesis were all in compliance with large-scale and cost-efficient fabrication techniques, standard in present industrial manufacturing. Plasmonic materials were restricted to aluminum and silver to guarantee low material expenses. Finally, all plasmonic structures were embedded by a transparent coating to assure durability and stability in ambient conditions.

The development and design of the plasmonic substrates involved screening with simulation tools, proper fabrication and subsequent measurement of the optical properties. The obtained findings were incorporated into a new model and corresponding fabrication parameters to further ameliorate the optical properties of the plasmonic structures. Even though the real shape of the fabricated structure is often strongly simplified in the simulations, the optical properties could be reproduced with high accuracy, especially for aluminum. To characterize the optical properties of the plasmonic substrates, a sophisticated and fully automated measurement setup was developed. It included a rotary stage, a spectrometer and a collimated broadband light source. A similar setup was used to realize the plasmonic multispectral camera described in Chapter 6.

Ultimately, I exploited some specific applications using the fabricated plasmonic filters. The angle-sensitive and symmetry breaking filters are very versatile for optical security applications, as demonstrated in Chapter 3 4. The observed zero-order transmission, including a strong

optical resonance, allows for very good visibility even under diffuse and unpolarized light conditions. This is in strong contrast to most holograms used to date, which are based on iridescent diffractive structures. Viewing angle-stable filters, which can be varied *via* the polarization (see Chapter 5), can be outstanding for spectral imaging applications. A proof-of-concept of a plasmonic multispectral imaging system is described in Chapter 6. For a wide range of applications, straightforward and cost-efficient modification of filters is often essential. Such modifications can be done by printing inks with different refractive indices onto the plasmonic structure (see Chapter 4).

In conclusion, it has been demonstrated that these new plasmonic color filters are versatile and useful for a number of applications. Especially the ability to control and change the transmission properties *in situ* could revolutionize the field of color filters. I believe the versatility of this active control can easily compensate for the intrinsic losses of plasmonic substrates. This thesis provides an in-depth description of the underlying physical mechanism of the color filters as well as their fabrication methods. Furthermore, concrete applications based on plasmonic substrates have been demonstrated, mainly for the areas of optical security and spectral imaging. This forms a fertile basis for further development of plasmonic color filters for ready-to-use industrial applications.

7.2 Outlook

Although this thesis demonstrates the versatility of plasmonic color filters for applications, probably years will pass until the first commercial product will be available. This is due to the fact that industrial manufacturers use equipment incorporated in an established production line. Adaptation to novel processes, *e.g.* angular evaporation, requires careful evaluations and adjustments. Furthermore, the plasmonic structures themselves have to be adapted for certain requirements of roll-to-roll manufacturing, *e.g.* higher structural depth for greater replication tolerance. Investigations with an external partner are underway to make the mass-replication of such optically variable features affordable. Similarly, the presented plasmonic spectral imaging system requires further development. Primarily, a substitute for the rotary stage and a more sophisticated solving algorithm have to be implemented. Furthermore, the combination with a multispectral imager, or even smartphone cameras could strongly push the usability of such a device. CSEM promotes ongoing projects in this direction.

Overall, plasmonic structures form the basis of these variable color filters. Their quality and control can be further enhanced by improving the fabrication parameters, testing novel plas-

monic materials, such as magnesium and copper, or designing 2D periodic plasmonic structures. This could enhance the contrast between plasmonic resonances while decreasing the structural dimensions. Ultimately, this fertile base of variable color filters could pave the way towards applications such as solar cells or displays that have not been addressed so far.

Bibliography

[1]   Georg, A. K. Industrial color physics. Springer, 2010.

[2]   Zollinger, H. *Color Chemistry*; Syntheses, Properties, and Applications of Organic Dyes and Pigments; John Wiley & Sons, 2003.

[3]   Kinoshita, S.; Yoshioka, S.; Miyazaki, J. Physics of structural colors. *Reports on Progress in Physics* **2008**, *71*, 076401.

[4]   Fu, Y.; Tippets, C. A.; Donev, E. U.; Lopez, R. Structural colors: from natural to artificial systems. *Wiley Interdisciplinary Reviews: Nanomedicine and Nanobiotechnology* **2016**, *8*, 758–775.

[5]   Kinoshita, S.; Yoshioka, S. Structural Colors in Nature: The Role of Regularity and Irregularity in the Structure. *ChemPhysChem* **2005**, *6*, 1442–1459.

[6]   Teyssier, J.; Saenko, S. V.; van der Marel, D.; Milinkovitch, M. C. Photonic crystals cause active colour change in chameleons. *Nature Communications* **2015**, *6*, 6368.

[7]   Parker, A. R. 515 million years of structural colour. *Journal of Optics A: Pure and Applied Optics* **2000**, *2*, R15–R28.

[8]   Parker, A. R.; Townley, H. E. Biomimetics of photonic nanostructures. *Nature Nanotechnology* **2007**, *2*, 347–353.

[9]   Chung, K.; Yu, S.; Heo, C.-J.; Shim, J. W.; Yang, S.-M.; Han, M. G.; Lee, H.-S.; Jin, Y.; Lee, S. Y.; Park, N.; Shin, J. H. Flexible, Angle-Independent, Structural Color Reflectors Inspired by Morpho Butterfly Wings. *Advanced Materials* **2012**, *24*, 2375–2379.

[10]   Garcia, M. A. Surface plasmons in metallic nanoparticles: fundamentals and applications. *Journal of Physics D: Applied Physics* **2011**, *44*, 283001–20.

[11]   Atwater, H. A. The Promise of Plasmonics. *Scientific American* **2007**, 56–63.

[12]   Colomban, P. The Use of Metal Nanoparticles to Produce Yellow, Red and Iridescent Colour, from Bronze Age to Present Times in Lustre Pottery and Glass: Solid State Chemistry, Spectroscopy and Nanostructure. *Journal of Nano Research* **2009**, *8*, 109–132.

[13]   Freestone, I.; Meeks, N.; Sax, M.; Higgitt, C. The Lycurgus Cup - A Roman nanotechnology. *Gold Bulletin* **2007**, *40*, 270–277.

[14]   Faraday, M. Experimental Relations of Gold (and Other Metals) to Light . *Philosophical Transactions of the Royal Society of London* **1857**, *147*, 145–181.

[15]   Liz-Marzán, L. M. Nanometals formation and color. *Materials Today* **2004**, *7*, 26–31.

[16] Novotny, L.; Hecht, B. Principles of nano-optics. Cambridge, 2012.

[17] Wood, R. W. On a Remarkable Case of Uneven Distribution of Light in a Diffraction Grating Spectrum. *Philosophical Magazine* **1902**, *4*, 1–7.

[18] Rayleigh, L. III. Note on the remarkable case of diffraction spectra described by Prof. Wood. *Philosophical Magazine Series 6* **1907**, *14*, 60–65.

[19] Maystre, D. *Plasmonics*; Chapter 2 - Theory of Wood's Anomalies; Springer-Verlag, 2012.

[20] Brongersma, M. L. Introductory lecture: nanoplasmonics. *Faraday Discussions* **2015**, *178*, 9–36.

[21] Fano, U. Effects of Configuration Interaction on Intensities and Phase Shifts. *Physical Review* **1961**, *124*, 1866–1878.

[22] Miroshnichenko, A. E.; Flach, S.; Kivshar, Y. S. Fano resonances in nanoscale structures. *Reviews of Modern Physics* **2010**, *82*, 2257–2298.

[23] Ebbesen, T. W.; Lezec, H. J.; Ghaemi, H. F.; Thio, T.; Wolff, P. A. Extraordinary optical transmission through sub-wavelength hole arrays. *Nature* **1998**, *391*, 667–669.

[24] Maier, S. A. Plasmonics: fundamentals and applications. Springer, 2007.

[25] Halas, N. J.; Lal, S.; Chang, W.-S.; Link, S.; Nordlander, P. Plasmons in Strongly Coupled Metallic Nanostructures. *Chemical Reviews* **2011**, *111*, 3913–3961.

[26] Liedberg, B.; Nylander, C.; Lundstrom, I. Surface-Plasmon Resonance for Gas-Detection and Biosensing. *Sensors and Actuators* **1983**, *4*, 299–304.

[27] Wang, S.; Ota, S.; Guo, B.; Ryu, J.; Rhodes, C.; Xiong, Y.; Kalim, S.; Zeng, L.; Chen, Y.; Teitell, M. A.; Zhang, X. Subcellular Resolution Mapping of Endogenous Cytokine Secretion by Nano-Plasmonic-Resonator Sensor Array. *Nano Letters* **2011**, *11*, 3431–3434.

[28] Howes, P. D.; Chandrawati, R.; Stevens, M. M. Colloidal nanoparticles as advanced biological sensors. *Science* **2014**, *346*, 1247390.

[29] Brongersma, M. L.; Halas, N. J.; Nordlander, P. Plasmon-induced hot carrier science and technology. *Nature Nanotechnology* **2015**, *10*, 25–34.

[30] Atwater, H. A.; Polman, A. Plasmonics for improved photovoltaic devices. *Nature Materials* **2010**, *9*, 205–213.

[31] Polman, A.; Atwater, H. A. Photonic design principles for ultrahigh-efficiency photovoltaics. *Nature Reviews Materials* **2012**, *11*, 174–177.

[32] Mubeen, S.; Lee, J.; Lee, W.-r.; Singh, N.; Stucky, G. D.; Moskovits, M. On the Plasmonic Photovoltaic. *ACS Nano* **2014**, *8*, 6066–6073.

[33] Schaadt, D. M.; Feng, B.; Yu, E. T. Enhanced semiconductor optical absorption via surface plasmon excitation in metal nanoparticles. *Applied Physics Letters* **2005**, *86*, 063106.

[34] Knight, M. W.; Wang, Y.; Urban, A. S.; Sobhani, A.; Zheng, B. Y.; Nordlander, P.; Halas, N. J. Embedding Plasmonic Nanostructure Diodes Enhances Hot Electron Emission. *Nano Letters* **2013**, *13*, 1687–1692.

[35] Chalabi, H.; Schoen, D.; Brongersma, M. L. Hot-Electron Photodetection with a Plasmonic Nanostripe Antenna. *Nano Letters* **2014**, *14*, 1374–1380.

[36] Linic, S.; Christopher, P.; Ingram, D. B. Plasmonic-metal nanostructures for efficient conversion of solar to chemical energy. *Nature Reviews Materials* **2011**, *10*, 911–921.

[37] Neumann, O.; Urban, A. S.; Day, J.; Lal, S.; Nordlander, P.; Halas, N. J. Solar Vapor Generation Enabled by Nanoparticles. *ACS Nano* **2013**, *7*, 42–49.

[38] Ozbay, E. Plasmonics: Merging Photonics and Electronics at Nanoscale Dimensions. *Science* **2006**, *311*, 189–193.

[39] Gramotnev, D. K.; Bozhevolnyi, S. I. Plasmonics beyond the diffraction limit. *Nature Photonics* **2010**, *4*, 83–91.

[40] Bozhevolnyi, S. *Plasmonic Nanoguides and Circuits*; Pan Stanford Publishing, 2009.

[41] Brongersma, M. L.; Shalaev, V. M. The case for plasmonics. *Science* **2010**, *328*, 440–441.

[42] Emboras, A.; Niegemann, J.; Ma, P.; Haffner, C.; Pedersen, A.; Luisier, M.; Hafner, C.; Schimmel, T.; Leuthold, J. Atomic Scale Plasmonic Switch. *Nano Letters* **2016**, *16*, 709–714.

[43] Haffner, C. et al. All-plasmonic Mach-Zehnder modulator enabling optical high-speed communication at the microscale. *Nature Photonics* **2015**, *9*, 525 –528.

[44] Bergman, D. J.; Stockman, M. I. Surface Plasmon Amplification by Stimulated Emission of Radiation: Quantum Generation of Coherent Surface Plasmons in Nanosystems. *Physical review letters* **2003**, *90*, 027402.

[45] Noginov, M. A.; Zhu, G.; Belgrave, A. M.; Bakker, R.; Shalaev, V. M.; Narimanov, E. E.; Stout, S.; Herz, E.; Suteewong, T.; Wiesner, U. Demonstration of a spaser-based nanolaser. *Nature* **2009**, *460*, 1110–1112.

[46] Kumar, K.; Duan, H.; Hegde, R. S.; Koh, S. C. W.; Wei, J. N.; Yang, J. K. W. Printing colour at the optical diffraction limit. *Nature Nanotechnology* **2012**, *7*, 557–561.

[47] Pendry, J. Photonics: Metamaterials in the sunshine. *Nature Materials* **2006**, *5*, 599–600.

[48] Pendry, J. B.; Schurig, D.; Smith, D. R. Controlling electromagnetic fields. *Science* **2006**, *312*, 1780–1782.

[49] Hess, O. Optics: farewell to flatland. *Nature* **2008**, *455*, 299–300.

[50] Chen, H.-T.; Taylor, A. J.; Yu, N. A review of metasurfaces: physics and applications. *Reports on Progress in Physics* **2016**, *79*, 076401.

[51] Pendry, J. B. Negative Refraction Makes a Perfect Lens. *Physical review letters* **2000**, *85*, 3966–3969.

[52] Shalaev, V. M. Optical negative-index metamaterials. *Nature Photonics* **2007**, *1*, 41–48.

[53] Schurig, D.; Mock, J. J.; Justice, B. J.; Cummer, S. A.; Pendry, J. B.; Starr, A. F.; Smith, D. R. Metamaterial Electromagnetic Cloak at Microwave Frequencies. *Science* **2006**, *314*, 977–980.

[54] Yu, N.; Capasso, F. Flat optics with designer metasurfaces. *Nature Materials* **2014**, *13*, 139–150.

[55] Lin, D.; Fan, P.; Hasman, E.; Brongersma, M. L. Dielectric gradient metasurface optical elements. *Science* **2014**, *345*, 298–302.

[56] Khorasaninejad, M.; Aieta, F.; Kanhaiya, P.; Kats, M. A.; Genevet, P.; Rousso, D.; Capasso, F. Achromatic Metasurface Lens at Telecommunication Wavelengths. *Nano Letters* **2015**, *15*, 5358–5362.

[57] Khorasaninejad, M.; Chen, W. T.; Zhu, A. Y.; Oh, J.; Devlin, R. C.; Rousso, D.; Capasso, F. Multispectral Chiral Imaging with a Metalens. *Nano Letters* **2016**, *16*, 4595–4600.

[58] Khorasaninejad, M.; Chen, W. T.; Devlin, R. C.; Oh, J.; Zhu, A. Y.; Capasso, F. Metalenses at visible wavelengths: Diffraction-limited focusing and subwavelength resolution imaging. *Science* **2016**, *352*, 1190–1194.

[59] Watts, C. M.; Liu, X.; Padilla, W. J. Metamaterial Electromagnetic Wave Absorbers. *Advanced Materials* **2012**, *24*, OP98–OP120.

[60] Akselrod, G. M.; Huang, J.; Hoang, T. B.; Bowen, P. T.; Su, L.; Smith, D. R.; Mikkelsen, M. H. Large-Area Metasurface Perfect Absorbers from Visible to Near-Infrared. *Advanced Materials* **2015**, *27*, 8028–8034.

[61] Yu, N.; Genevet, P.; Kats, M. A.; Aieta, F.; Tetienne, J. P.; Capasso, F.; Gaburro, Z. Light Propagation with Phase Discontinuities: Generalized Laws of Reflection and Refraction. *Science* **2011**, *334*, 333–337.

[62] Huang, L.; Chen, X.; Mühlenbernd, H.; Zhang, H.; Chen, S.; Bai, B.; Tan, Q.; Jin, G.; Cheah, K.-W.; Qiu, C.-W.; Li, J.; Zentgraf, T.; Zhang, S. Three-dimensional optical holography using a plasmonic metasurface. *Nature Communications* **2013**, *4*, 2808.

[63] Zheng, G.; Mühlenbernd, H.; Kenney, M.; Li, G.; Zentgraf, T.; Zhang, S. Metasurface holograms reaching 80% efficiency. *Nature Nanotechnology* **2015**, *10*, 308–312.

[64] de Leon, N. P.; Lukin, M. D.; Park, H. Quantum Plasmonic Circuits. *IEEE Journal of Selected Topics in Quantum Electronics* **2012**, *18*, 1781–1791.

[65] García de Abajo, F. J. Graphene Nanophotonics. *Science* **2013**, *339*, 917–918.

[66] Tetienne, J. P.; Hingant, T.; Kim, J. V.; Diez, L. H.; Adam, J. P.; Garcia, K.; Roch, J. F.; Rohart, S.; Thiaville, A.; Ravelosona, D.; Jacques, V. Nanoscale imaging and control of domain-wall hopping with a nitrogen-vacancy center microscope. *Science* **2014**, *344*, 1366–1369.

[67] Goodfellow, K. M.; Beams, R.; Chakraborty, C.; Novotny, L.; Vamivakas, A. N. Integrated nanophotonics based on nanowire plasmons and atomically thin material. *Optica* **2014**, *1*, 149–4.

[68] Kress, S. J. P.; Antolinez, F. V.; Richner, P.; Jayanti, S. V.; Kim, D. K.; Prins, F.; Riedinger, A.; Fischer, M. P. C.; Meyer, S.; McPeak, K. M.; Poulikakos, D.; Norris, D. J. Wedge Waveguides and Resonators for Quantum Plasmonics. *Nano Letters* **2015**, *15*, 6267–6275.

[69] Wang, Z.; Dong, Z.; Gu, Y.; Chang, Y.-H.; Zhang, L.; Li, L.-J.; Zhao, W.; Eda, G.; Zhang, W.; Grinblat, G.; Maier, S. A.; Yang, J. K. W.; Qiu, C.-W.; Wee, A. T. S. Giant photoluminescence enhancement in tungsten-diselenide-gold plasmonic hybrid structures. *Nature Communications* **2016**, *7*, 1–8.

[70] Guler, U.; Kildishev, A. V.; Boltasseva, A.; Shalaev, V. M. Plasmonics on the slope of enlightenment: the role of transition metal nitrides. *Faraday Discussions* **2015**, *178*, 71–86.

[71] Khurgin, J. B. How to deal with the loss in plasmonics and metamaterials. *Nature Nanotechnology* **2015**, *10*, 2–6.

[72] Chen, Q.; Hu, X.; Wen, L.; Yu, Y.; Cumming, D. R. S. Nanophotonic Image Sensors. *Small* **2016**, *12*, 4922–4935.

[73] Graydon, O. VIEW FROM... SPP7: A colourful future? *Nature Photonics* **2015**, *9*, 487–488.

[74] Tan, S. J.; Goh, X. M.; Wang, Y. M.; Yang, J. K. W.; Teng, J. Engineering Plasmonic Colors in Metal Nanostructures. *Journal of Molecular and Engineering Materials* **2014**, *2*, 1440011.

[75] Kristensen, A.; Yang, J. K. W.; Bozhevolnyi, S. I.; Link, S.; Nordlander, P.; Halas, N. J.; Mortensen, N. A. Plasmonic colour generation. *Nature Reviews Materials* **2016**, *2*, 16088–15.

[76] Zeng, B.; Gao, Y.; Bartoli, F. J. Ultrathin Nanostructured Metals for Highly Transmissive Plasmonic Subtractive Color Filters. *Scientific Reports* **2013**, *3*, 1–9.

[77] Lee, R. A. Micro-technology for anti-counterfeiting. *Microelectronic Engineering* **2000**, *53*, 513–516.

[78] Gale, M. T.; Knop, K.; Morf, R. Zero-order Diffractive Microstructures for Security Applications. *Proceedings of SPIE* **1990**, *1210*, 83–89.

[79] Lochbihler, H. Colored images generated by metallic sub-wavelength gratings. *Optics Express* **2009**, *17*, 12189–12196.

[80] Lochbihler, H. Reflective colored image based on metal–dielectric–metal-coated gratings. *Optics letters* **2013**, *38*, 1398–1400.

[81] Sauvage-Vincent, J.; Tonchev, S.; Veillas, C.; Reynaud, S.; Jourlin, Y. Optical security device for document protection using plasmon resonant transmission through a thin corrugated metallic film embedded in a plastic foil. *Journal of the European Optical Society: Rapid Publications* **2013**, *8*, 13015.

[82] Gallinet, B.; Martin, O. J. F. Refractive Index Sensing with Subradiant Modes: A Framework To Reduce Losses in Plasmonic Nanostructures. *ACS Nano* **2013**, *7*, 6978–6987.

[83] Shen, Y.; Zhou, J.; Liu, T.; Tao, Y.; Jiang, R.; Liu, M.; Xiao, G.; Zhu, J.; Zhou, Z.-K.; Wang, X.; Jin, C.; Wang, J. Plasmonic gold mushroom arrays with refractive index sensing figures of merit approaching the theoretical limit. *Nature Communications* **2013**, *4*, 1–9.

[84] Lindquist, N. C.; Nagpal, P.; McPeak, K. M.; Norris, D. J.; Oh, S.-H. Engineering metallic nanostructures for plasmonics and nanophotonics. *Reports on Progress in Physics* **2012**, *75*, 036501.

[85] Liddle, J. A.; Gallatin, G. M. Nanomanufacturing: A Perspective. *ACS Nano* **2016**, *10*, 2995–3014.

[86] Brunner, R.; Sandfuchs, O.; Pacholski, C.; Morhard, C.; Spatz, J. Lessons from nature: biomimetic subwavelength structures for high-performance optics. *Laser & Photonics Reviews* **2011**, *6*, 641–659.

[87] Palmer, C. *Diffraction Grating Handbook*; Newport Corporation, 2005.

[88] Gale, M. T. Diffractive Microstructures for Security Applications. *Third International Conference on Holographic Systems, Components and Applications, 1991* **1991**, 205–209.

[89] Lütolf, F.; Stalder, M.; Martin, O. J. F. Up-scalable method to amplify the diffraction efficiency of simple gratings. *Optics letters* **2014**, *39*, 6557–6560.

[90] van Renesse, R. L. *Optical Document Security*; Artech, 1998.

[91] Basset, G.; Quaranta, G.; Lütolf, F.; Davoine, L.; Schnieper, M. Subwavelength gratings for OVDs - From local interactions to using light-transport. *arXiv.org* **2015**,

[92] Loewen, E. G.; Neviere, M.; Maystre, D. Grating Efficiency Theory as It Applies to Blazed and Holographic Gratings. *Applied Optics* **1977**, *16*, 2711–2721.

[93] Aoyagi, T.; Aoyagi, Y.; Namba, S. High-Efficiency Blazed Grating Couplers. *Applied Physics Letters* **1976**, *29*, 303–304.

[94] Feng, J.; Zhou, Z. Polarization beam splitter using a binary blazed grating coupler. *Optics letters* **2007**, *32*, 1662–1664.

[95] Harvey, K. C.; Myatt, C. J. External-Cavity Diode-Laser Using a Grazing-Incidence Diffraction Grating. *Optics letters* **1991**, *16*, 910–912.

[96] Heine, C.; Morf, R. H. Submicrometer Gratings for Solar-Energy Applications. *Applied Optics* **1995**, *34*, 2476–2482.

[97] OShea, D. C.; Suleski, T. J.; Kathman, A. D.; Prather, D. W. *Diffractive Optics: Design, Fabrication, and Test*; SPIE Press, 2004; Vol. 62.

[98] Goodman, J. W. *Introduction to Fourier optics*; Roberts and Company Publishers, 2005.

[99] Miller, J. M.; De Beaucoudrey, N.; Chavel, P.; Turunen, J.; Cambril, E. Design and fabrication of binary slanted surface-relief gratings for a planar optical interconnection. *Applied Optics* **1997**, *36*, 5717–5727.

[100] Goebel, B.; Wang, L. L.; Tschudi, T. Multilayer technology for diffractive optical elements. *Applied Optics* **1996**, *35*, 4490–4493.

[101] Farn, M. W. Binary gratings with increased efficiency. *Applied Optics* **1992**, 4453–4458.

[102] Haidner, H.; Kipfer, P.; Sheridan, J. T.; Schwider, J.; Streibl, N.; Collischon, M.; Hutfless, J.; März, M. Diffraction Grating with Rectangular Grooves Exceeding 80-Percent Diffraction Efficiency. *Infrared Physics* **1993**, *34*, 467–475.

[103] Lalanne, P.; Astilean, S.; Chavel, P.; Cambril, E.; Launois, H. Blazed binary subwavelength gratings with efficiencies larger than those of conventional echelette gratings. *Optics letters* **1998**, *23*, 1081–1083.

[104] Lalanne, P.; Astilean, S.; Chavel, P.; Cambril, E.; Launois, H. Design and fabrication of blazed binary diffractive elements with sampling periods smaller than the structural cutoff. *Journal of the Optical Society of America A* **1999**, *16*, 1143–1156.

[105] Raguin, D. H.; Morris, G. M. Subwavelength structured surfaces and their applications. *Critical Reviews of Optical Science and Technology* **1993**, *CR49*, 234–261.

[106] Kikuta, H.; Toyota, H.; Yu, W. J. Optical elements with subwavelength structured surfaces. *Optical Review* **2003**, *10*, 63–73.

[107] Raguin, D. H.; Morris, G. M. Analysis of Antireflection-Structured Surfaces with Continuous One-Dimensional Surface Profiles. *Applied Optics* **1993**, *32*, 2582–2598.

[108] Flanders, D. C. Submicrometer periodicity gratings as artificial anisotropic dielectrics. *Applied Physics Letters* **1983**, *42*, 492–494.

[109] Chou, S. Y.; Deng, W. Subwavelength amorphous silicon transmission gratings and applications in polarizers and waveplates. *American Journal of Physics* **1996**, *67*, 742–744.

[110] Moharam, M. G.; Gaylord, T. K. Diffraction Analysis of Dielectric Surface-Relief Gratings. *Journal of the Optical Society of America* **1982**, *72*, 1385–1392.

[111] Grann, E. B.; Moharam, M. G.; Pommet, D. A. Optimal-Design for Antireflective Tapered 2-Dimensional Subwavelength Grating Structures. *Journal of the Optical Society of America A* **1995**, *12*, 333–339.

[112] Lalanne, P.; Morris, G. M. Antireflection behavior of silicon subwavelength periodic structures for visible light. *Nanotechnology* **1996**, *8*, 53–56.

[113] Wilson, S. J.; Hutley, M. C. The Optical Properties of 'Moth Eye' Antireflection Surfaces. *Optica Acta: International Journal of Optics* **2010**, *29*, 993–1009.

[114] Ding, F.; Pors, A.; Chen, Y.; Zenin, V. A.; Bozhevolnyi, S. I. Beam-Size-Invariant Spectropolarimeters Using Gap-Plasmon Metasurfaces. *ACS Photonics* **2017**, *4*, 943–949.

[115] Wang, S. S.; Magnusson, R. Theory and Applications of Guided-Mode Resonance Filters. *Applied Optics* **1993**, *32*, 2606–2613.

[116] Rosenblatt, D.; Sharon, A.; Friesem, A. A. Resonant Grating Waveguide Structures. *IEEE Journal of Quantum Electronics* **1997**, *33*, 2038–2059.

[117] Hessel, A.; Oliner, A. A. A New Theory of Wood's Anomalies on Optical Gratings. *Applied Optics* **1965**, *4*, 1275–1297.

[118] Loewen, E. G.; Popov, E. *Diffraction gratings and applications*; CRC Press, 1997.

[119] Maurel, A.; Felix, S.; Mercier, J. F.; Ourir, A.; Djeffal, Z. E. Wood's anomalies for arrays of dielectric scatterers. *Journal of the European Optical Society: Rapid Publications* **2014**, *9*, 14001.

[120] Ritchie, R. H.; Arakawa, E. T.; Cowan, J. J.; Hamm, R. N. Surface-Plasmon Resonance Effect in Grating Diffraction. *Physical review letters* **1968**, *21*, 1530–1533.

[121] Fano, U. The Theory of Anomalous Diffraction Gratings and of Quasi-Stationary Waves on Metallic Surfaces (Sommerfeld's Waves). *Journal of the Optical Society of America* **1941**, *31*, 213–222.

[122] Mashev, L.; Popov, E. Zero Order Anomaly of Dielectric Coated Gratings. *Optics Communications* **1985**, *55*, 377–380.

[123] Wang, S. S.; Magnusson, R.; Bagby, J. S.; Moharam, M. G. Guided-Mode Resonances in Planar Dielectric-Layer Diffraction Gratings. *Journal of the Optical Society of America A* **1990**, *7*, 1470–1474.

[124] Tikhodeev, S. G.; Yablonskii, A. L.; Muljarov, E. A.; Gippius, N. A.; Ishihara, T. Quasiguided modes and optical properties of photonic crystal slabs. *Physical Review B* **2002**, *66*, 045102.

[125] Christ, A.; Zentgraf, T.; Kuhl, J.; Tikhodeev, S.; Gippius, N.; Giessen, H. Optical properties of planar metallic photonic crystal structures: Experiment and theory. *Physical Review B* **2004**, *70*, 125113.

[126] Kats, M. A.; Blanchard, R.; Genevet, P.; Capasso, F. Nanometre optical coatings based on strong interference effects in highly absorbing media. *Nature Materials* **2012**, *12*, 20–24.

[127] Macleod, H. *Thin-Film Optical Filters, Third Edition*; Series in Optics and Optoelectronics; Taylor & Francis, 2001.

[128] Raut, H. K.; Ganesh, V. A.; Nair, A. S.; Ramakrishna, S. Anti-reflective coatings: A critical, in-depth review. *Energy & Environmental Science* **2011**, *4*, 3779–3804.

[129] Kats, M. A.; Byrnes, S. J.; Blanchard, R.; Kolle, M.; Genevet, P.; Aizenberg, J.; Capasso, F. Enhancement of absorption and color contrast in ultra-thin highly absorbing optical coatings. *Applied Physics Letters* **2013**, *103*, 101104.

[130] Busch, K.; von Freymann, G.; Linden, S.; Mingaleev, S. F.; Tkeshelashvili, L.; Wegener, M. Periodic nanostructures for photonics. *Physics Reports* **2007**, *444*, 101–202.

[131] Yablonovitch, E. Photonic band-gap structures. *Journal of the Optical Society of America B* **1993**, *10*, 283–295.

[132] Arriaga, J.; Knight, J. C.; Russell, P. S. J. Modeling the propagation of light in photonic crystal fibers. *Physica D: Nonlinear Phenomena* **2004**, *189*, 100–106.

[133] Joannopoulos, J. D.; Johnson, S. G.; Winn, J. N.; Meade, R. D. *Photonic Crystals*; Molding the Flow of Light (Second Edition); Princeton University Press, 2011.

[134] Astratov, V. N.; Bogomolov, V. N.; Kaplyanskii, A. A.; Prokofiev, A. V.; Samoilovich, L. A.; Samoilovich, S. M.; Vlasov, Y. A. Optical spectroscopy of opal matrices with CdS embedded in its pores: Quantum confinement and photonic band gap effects. *Nuovo Cimento Della Societa Italiana Di Fisica D-Condensed Matter Atomic Molecular and Chemical Physics Fluids Plasmas Biophysics* **1995**, *17*, 1349–1354.

[135] Seo, K.; Wober, M.; Steinvurzel, P.; Schonbrun, E.; Dan, Y.; Ellenbogen, T.; Crozier, K. B. Multicolored Vertical Silicon Nanowires. *Nano Letters* **2011**, *11*, 1851–1856.

[136] Cao, L.; Fan, P.; Barnard, E. S.; Brown, A. M.; Brongersma, M. L. Tuning the Color of Silicon Nanostructures. *Nano Letters* **2010**, *10*, 2649–2654.

[137] Zhao, Q.; Zhou, J.; Zhang, F.; Lippens, D. Mie resonance-based dielectric metamaterials. *Materials Today* **2009**, *12*, 60–69.

[138] Proust, J.; Bedu, F.; Gallas, B.; Ozerov, I.; Bonod, N. All-Dielectric Colored Metasurfaces with Silicon Mie Resonators. *ACS Nano* **2016**, *10*, 7761–7767.

[139] Gu, Y.; Zhang, L.; Yang, J. K. W.; Yeo, S. P.; Qiu, C.-W. Color Generation via Subwavelength Plasmonic Nanostructures. *Nanoscale* **2015**, *7*, 6409–6419.

[140] Yu, Y.; Wen, L.; Song, S.; Chen, Q. Transmissive/Reflective structural color filters: theory and applications. *Journal of Nanomaterials* **2014**, 1–16.

[141] Xu, T.; Shi, H.; Wu, Y.-K.; Kaplan, A. F.; Ok, J. G.; Guo, L. J. Structural Colors: From Plasmonic to Carbon Nanostructures. *Small* **2011**, *7*, 3128–3136.

[142] Henzie, J.; Lee, J.; Lee, M. H.; Hasan, W.; Odom, T. W. Nanofabrication of Plasmonic Structures. *Annual Review of Physical Chemistry* **2009**, *60*, 147–165.

[143] Popov, E.; Tsonev, L.; Maystre, D. Lamellar Metallic Grating Anomalies. *Applied Optics* **1994**, *33*, 5214–5219.

[144] Kuta, J. J.; Van Driel, H. M.; Landheer, D.; Feng, Y. Coupled-Wave Analysis of Lamellar Metal Transmission Gratings for the Visible and the Infrared. *Journal of the Optical Society of America A* **1995**, *12*, 1118–1127.

[145] Schider, G.; Krenn, J. R.; Gotschy, W.; Lamprecht, B.; Ditlbacher, H.; Leitner, A.; Aussenegg, F. R. Optical properties of Ag and Au nanowire gratings. *Journal of Applied Physics* **2001**, *90*, 3825–3830.

[146] Christ, A.; Tikhodeev, S.; Gippius, N.; Kuhl, J.; Giessen, H. Waveguide-Plasmon Polaritons: Strong Coupling of Photonic and Electronic Resonances in a Metallic Photonic Crystal Slab. *Physical review letters* **2003**, *91*, 183901.

[147] Shrestha, V. R.; Lee, S.-S.; Kim, E.-S.; Choi, D.-Y. Polarization-tuned Dynamic Color Filters Incorporating a Dielectric- loaded Aluminum Nanowire Array. *Scientific Reports* **2015**, *5*, 12450.

[148] Wu, Y.-K. R.; Hollowell, A. E.; Zhang, C.; Guo, L. J. Angle-Insensitive Structural Colours based on Metallic Nanocavities and Coloured Pixels beyond the Diffraction Limit. *Scientific Reports* **2013**, *3*, 1194.

[149] Yoon, Y.-T.; Park, C.-H.; Lee, S.-S. Highly Efficient Color Filter Incorporating a Thin Metal–Dielectric Resonant Structure. *Applied Physics Express* **2012**, *5*, 022501.

[150] Lütolf, F.; Martin, O. J. F.; Gallinet, B. Fano-resonant aluminum and gold nanostructures created with a tunable, up-scalable process. *Nanoscale* **2015**, *7*, 18179–18187.

[151] Lütolf, F.; Casari, D.; Gallinet, B. Low-Cost and Large-Area Strain Sensors Based on Plasmonic Fano Resonances. *Advanced Optical Materials* **2016**, *4*, 715–721.

[152] Lütolf, F.; Stalder, M.; Martin, O. J. F. Metallized Gratings Enable Color Effects and Floating Screen Films by First-Order Diffraction. *Advanced Optical Materials* **2015**, *3*, 1793–1799.

[153] Ellenbogen, T.; Seo, K.; Crozier, K. B. Chromatic Plasmonic Polarizers for Active Visible Color Filtering and Polarimetry. *Nano Letters* **2012**, *12*, 1026–1031.

[154] Olson, J.; Manjavacas, A.; Basu, T.; Huang, D.; Schlather, A. E.; Zheng, B.; Halas, N. J.; Nordlander, P.; Link, S. High Chromaticity Aluminum Plasmonic Pixels for Active Liquid Crystal Displays. *ACS Nano* **2015**, *10*, 1108–1117.

[155] Olson, J.; Manjavacas, A.; Liu, L.; Chang, W. S.; Foerster, B.; King, N. S.; Knight, M. W.; Nordlander, P.; Halas, N. J.; Link, S. Vivid, full-color aluminum plasmonic pixels. *Proceedings of the National Academy of Sciences* **2014**, *111*, 14348–14353.

[156] Shrestha, V. R.; Park, C.-S.; Lee, S.-S. Enhancement of color saturation and color gamut enabled by a dual-band color filter exhibiting an adjustable spectral response. *Optics Express* **2014**, *22*, 3691.

[157] Hu, X. L.; Sun, L. B.; Zeng, B.; Wang, L. S.; Yu, Z. G.; Bai, S. A.; Yang, S. M.; Zhao, L. X.; Li, Q.; Qiu, M.; Tai, R. Z.; Fecht, H. J.; Jiang, J. Z.; Zhang, D. X. Polarization-independent plasmonic subtractive color filtering in ultrathin Ag nanodisks with high transmission. *Applied Optics* **2016**, *55*, 148–5.

[158] Ye, M.; Sun, L.; Hu, X.; Shi, B.; Zeng, B.; Wang, L.; Zhao, J.; Yang, S.; Tai, R.; Fecht, H.-J.; Jiang, J.-Z.; Zhang, D.-X. Angle-insensitive plasmonic color filters with randomly distributed silver nanodisks. *Optics letters* **2015**, *40*, 4979–4982.

[159] Si, G.; Zhao, Y.; Lv, J.; Lu, M.; Wang, F.; Liu, H.; Xiang, N.; Huang, T. J.; Danner, A. J.; Teng, J.; Liu, Y. J. Reflective plasmonic color filters based on lithographically patterned silver nanorod arrays. *Nanoscale* **2013**, *5*, 6243.

[160] Li, Z.; Clark, A. W.; Cooper, J. M. Dual Color Plasmonic Pixels Create a Polarization Controlled Nano Color Palette. *ACS Nano* **2016**, *10*, 492–498.

[161] Genet, C.; Ebbesen, T. W. Light in tiny holes. *Nature* **2007**, *445*, 39–46.

[162] Lin, L.; Roberts, A. Angle-robust resonances in cross-shaped aperture arrays. *Applied Physics Letters* **2010**, *97*, 061109.

[163] Do, Y. S.; Park, J. H.; Hwang, B. Y.; Lee, S.-M.; Ju, B.-K.; Choi, K. C. Plasmonic Color Filter and its Fabrication for Large-Area Applications. *Advanced Optical Materials* **2013**, *1*, 133–138.

[164] Inoue, D.; Miura, A.; Nomura, T.; Fujikawa, H.; Sato, K.; Ikeda, N.; Tsuya, D.; Sugimoto, Y.; Koide, Y. Polarization independent visible color filter comprising an aluminum film with surface-plasmon enhanced transmission through a subwavelength array of holes. *Applied Physics Letters* **2011**, *98*, 093113.

[165] Lee, H.-S.; Yoon, Y.-T.; Lee, S.-S.; Kim, S.-H.; Lee, K.-D. Color filter based on a subwavelength patterned meta. *Optics Express* **2007**, *15*, 15457–15463.

[166] Burgos, S. P.; Yokogawa, S.; Atwater, H. A. Color Imaging via Nearest Neighbor Hole Coupling in Plasmonic Color Filters Integrated onto a Complementary Metal-Oxide Semiconductor Image Sensor. *ACS Nano* **2013**, *7*, 10038–10047.

[167] Yokogawa, S.; Burgos, S. P.; Atwater, H. A. Plasmonic Color Filters for CMOS Image Sensor Applications. *Nano Letters* **2012**, *12*, 4349–4354.

[168] Chen, Q.; Cumming, D. R. S. High transmission and low color cross-talk plasmonic color filters using triangular-lattice hole arrays in aluminum films. *Optics Express* **2010**, *18*, 14056–14062.

[169] Chen, Q.; Das, D.; Chitnis, D.; Walls, K.; Drysdale, T. D.; Collins, S.; Cumming, D. R. S. A CMOS Image Sensor Integrated with Plasmonic Colour Filters. *Plasmonics* **2012**, *7*, 695–699.

[170] Chen, Q.; Chitnis, D.; Walls, K.; Drysdale, T. D.; Collins, S.; Cumming, D. R. S. CMOS Photodetectors Integrated With Plasmonic Color Filters. *IEEE Photonics Technology Letters* **2012**, *24*, 197–199.

[171] Rajasekharan, R.; Balaur, E.; Minovich, A.; Collins, S.; James, T. D.; Djalalian-Assl, A.; Ganesan, K.; Tomljenovic-Hanic, S.; Kandasamy, S.; Skafidas, E.; Neshev, D. N.; Mulvaney, P.; Roberts, A.; Prawer, S. Filling schemes at submicron scale: Development of submicron sized plasmonic colour filters. *Scientific Reports* **2014**, *4*, 6435.

[172] Diest, K.; Dionne, J. A.; Spain, M.; Atwater, H. A. Tunable Color Filters Based on Metal−Insulator−Metal Resonators. *Nano Letters* **2009**, *9*, 2579–2583.

[173] Xu, T.; Wu, Y.-K.; Luo, X.; Guo, L. J. Plasmonic nanoresonators for high-resolution colour filtering and spectral imaging. *Nature Communications* **2010**, *1*, 59.

[174] Tan, S. J.; Zhang, L.; Zhu, D.; Goh, X. M.; Wang, Y. M.; Kumar, K.; Qiu, C.-W.; Yang, J. K. W. Plasmonic Color Palettes for Photorealistic Printing with Aluminum Nanostructures. *Nano Letters* **2014**, *14*, 4023–4029.

[175] Li, W.-D.; Hu, J.; Chou, S. Y. Extraordinary light transmission through opaque thin metal film with subwavelength holes blocked by metal disks. *Optics Express* **2011**, *19*, 21098–21108.

[176] Lochbihler, H.; Ye, Y. Two-dimensional subwavelength gratings with different frontside/backside reflectance. *Optics letters* **2013**, *38*, 1028–1030.

[177] Clausen, J. S.; Højlund-Nielsen, E.; Christiansen, A. B.; Yazdi, S.; Grajower, M.; Taha, H.; Levy, U.; Kristensen, A.; Mortensen, N. A. Plasmonic Metasurfaces for Coloration of Plastic Consumer Products. *Nano Letters* **2014**, *14*, 4499–4504.

[178] James, T. D.; Mulvaney, P.; Roberts, A. The Plasmonic Pixel: Large Area, Wide Gamut Color Reproduction Using Aluminum Nanostructures. *Nano Letters* **2016**, *16*, 3817–3823.

[179] Goh, X. M.; Zheng, Y.; Tan, S. J.; Zhang, L.; Kumar, K.; Qiu, C.-W.; Yang, J. K. W. Three-dimensional plasmonic stereoscopic prints in full colour. *Nature Communications* **2014**, *5*, 1–8.

[180] Roberts, A. S.; Pors, A.; Albrektsen, O.; Bozhevolnyi, S. I. Subwavelength Plasmonic Color Printing Protected for Ambient Use. *Nano Letters* **2014**, *14*, 783–787.

[181] Miyata, M.; Hatada, H.; Takahara, J. Full-Color Subwavelength Printing with Gap-Plasmonic Optical Antennas. *Nano Letters* **2016**, *16*, 3166–3172.

[182] Zhu, X.; Vannahme, C.; Hølund-Nielsen, E.; Mortensen, N. A.; Kristensen, A. Plasmonic colour laser printing. *Nature Nanotechnology* **2015**, *11*, 325 –329.

[183] Yoon, Y.-T.; Lee, S.-S. Transmission type color filter incorporating a silver film based etalon. *Optics Express* **2010**, *18*, 5344–5349.

[184] Huang, Y.-W.; Chen, W. T.; Tsai, W.-Y.; Wu, P. C.; Wang, C.-M.; Sun, G.; Tsai, D. P. Aluminum Plasmonic Multicolor Meta-Hologram. *Nano Letters* **2015**, *15*, 3122–3127.

[185] Cheng, F.; Gao, J.; Luk, T. S.; Yang, X. Structural color printing based on plasmonic metasurfaces of perfect light absorption. *Scientific Reports* **2015**, *5*, 11045.

[186] Cheng, F.; Gao, J.; Stan, L.; Rosenmann, D.; Czaplewski, D.; Yang, X. Aluminum plasmonic metamaterials for structural color printing. *Optics Express* **2015**, *23*, 14552–14560.

[187] Lochbihler, H. Surface polaritons on metallic wire gratings studied via power losses. *Physical Review B* **1996**, *53*, 10289–10295.

[188] Raether, H. Surface-Plasmons on Smooth and Rough Surfaces and on Gratings. *Springer Tracts in Modern Physics* **1988**, *111*, 1–133.

[189] Sarrazin, M.; Vigneron, J.-P.; Vigoureux, J.-M. Role of Wood anomalies in optical properties of thin metallic films with a bidimensional array of subwavelength holes. *Physical Review B* **2003**, *67*, 085415.

[190] Lee, S. Y.; Forestiere, C.; Pasquale, A. J.; Trevino, J. Plasmon-enhanced structural coloration of metal films with isotropic Pinwheel nanoparticle arrays. *Optics Express* **2011**, *19*, 23818–23830.

[191] Zhang, J.; Ou, J.-Y.; Papasimakis, N.; Chen, Y.; MacDonald, K. F.; Zheludev, N. I. Continuous metal plasmonic frequency selective surfaces. *Optics Express* **2011**, *19*, 23279–23285.

[192] Zhang, J.; Ou, J.-Y.; MacDonald, K. F.; Zheludev, N. I. Optical response of plasmonic relief meta-surfaces. *Journal of Optics* **2012**, *14*, 114002.

[193] Ng, R. J. H.; Goh, X. M.; Yang, J. K. W. All-metal nanostructured substrates as subtractive color reflectors with near-perfect absorptance. *Optics Express* **2015**, *23*, 32597–32605.

[194] Guay, J.-M.; Lesina, A. C.; Côté, G.; Charron, M.; Ramunno, L.; Berini, P.; Weck, A. Topographical coloured plasmonic coins. *arXiv.org* **2016**, 1–9.

[195] Goh, X. M.; Ng, R. J. H.; Wang, S.; Tan, S. J.; Yang, J. K. W. Comparative Study of Plasmonic Colors from All-Metal Structures of Posts and Pits. *ACS Photonics* **2016**, *3*, 1000–1009.

[196] Varghese, L. T.; Fan, L.; Xuan, Y.; Tansarawiput, C.; Kim, S.; Qi, M. Resistless Nanoimprinting in Metal for Plasmonic Nanostructures. *Small* **2013**, *9*, 3778–3783.

[197] Si, G.; Zhao, Y.; Liu, H.; Teo, S.; Zhang, M.; Jun Huang, T.; Danner, A. J.; Teng, J. Annular aperture array based color filter. *Applied Physics Letters* **2011**, *99*, 033105.

[198] Lee, K.-T.; Jang, J.-Y.; Park, S. J.; Ji, C.; Yang, S.-M.; Guo, L. J.; Park, H. J. Angle-Insensitive and CMOS-Compatible Subwavelength Color Printing. *Advanced Optical Materials* **2016**, *4*, 1696–1702.

[199] Xue, J.; Wei, Z.; Su, R.; Lai, J.; Li, J.; Li, C.; Zhang, T.; Zhou, Z.-K.; Wang, X.-H. Scalable, full-colour and controllable chromotropic plasmonic printing. *Nature Communications* **2015**, *6*, 8906.

[200] Yin, Y.; Alivisatos, A. P. Colloidal nanocrystal synthesis and the organic–inorganic interface. *Nature* **2005**, *437*, 664–670.

[201] Mock, J. J.; Barbic, M.; Smith, D. R.; Schultz, D. A.; Schultz, S. Shape effects in plasmon resonance of individual colloidal silver nanoparticles. *The Journal of Chemical Physics* **2002**, *116*, 6755–6759.

[202] Sun, Y.; Xia, Y. Gold and silver nanoparticles: A class of chromophores with colors tunable in the range from 400 to 750 nm. *The Analyst* **2003**, *128*, 686–691.

[203] McClain, M. J.; Schlather, A. E.; Ringe, E.; King, N. S.; Liu, L.; Manjavacas, A.; Knight, M. W.; Kumar, I.; Whitmire, K. H.; Everitt, H. O.; Nordlander, P.; Halas, N. J. Aluminum Nanocrystals. *Nano Letters* **2015**, *15*, 2751–2755.

[204] Hsu, C. W.; Zhen, B.; Qiu, W.; Shapira, O.; DeLacy, B. G.; Joannopoulos, J. D.; Soljačić, M. Transparent displays enabled by resonant nanoparticle scattering. *Nature Communications* **2014**, *5*, 1–6.

[205] DeSantis, C. J.; Weiner, R. G.; Radmilovic, A.; Bower, M. M.; Skrabalak, S. E. Seeding Bimetallic Nanostructures as a New Class of Plasmonic Colloids. *The Journal of Physical Chemistry Letters* **2013**, *4*, 3072–3082.

[206] Park, G.; Lee, C.; Seo, D.; Song, H. Full-Color Tuning of Surface Plasmon Resonance by Compositional Variation of Au@Ag Core–Shell Nanocubes with Sulfides. *Langmuir* **2012**, *28*, 9003–9009.

[207] Yu, R.; Mazumder, P.; Borrelli, N. F.; Carrilero, A.; Ghosh, D. S.; Maniyara, R. A.; Baker, D.; García de Abajo, F. J.; Pruneri, V. Structural Coloring of Glass Using Dewetted Nanoparticles and Ultrathin Films of Metals. *ACS Photonics* **2016**, *3*, 1194–1201.

[208] King, N. S.; Li, Y.; Ayala-Orozco, C.; Brannan, T.; Nordlander, P.; Halas, N. J. Angle- and Spectral-Dependent Light Scattering from Plasmonic Nanocups. *ACS Nano* **2011**, *5*, 7254–7262.

[209] Klinkova, A.; Choueiri, R. M.; Kumacheva, E. Self-assembled plasmonic nanostructures. *Chemical Society Reviews* **2014**, *43*, 3976–16.

[210] Chen, T.; Reinhard, B. M. Assembling Color on the Nanoscale: Multichromatic Switchable Pixels from Plasmonic Atoms and Molecules. *Advanced Materials* **2016**, *28*, 3522–3527.

[211] Cheng, W.; Campolongo, M. J.; Cha, J. J.; Tan, S. J.; Umbach, C. C.; Muller, D. A.; Luo, D. Free-standing nanoparticle superlattice sheets controlled by DNA. *Nature Materials* **2009**, *8*, 519–525.

[212] Kuzyk, A.; Schreiber, R.; Fan, Z.; Pardatscher, G.; Roller, E.-M.; Högele, A.; Simmel, F. C.; Govorov, A. O.; Liedl, T. DNA-based self-assembly of chiral plasmonic nanostructures with tailored optical response. *Nature* **2012**, *483*, 311–314.

[213] McPeak, K. M.; Jayanti, S. V.; Kress, S. J. P.; Meyer, S.; Iotti, S.; Rossinelli, A.; Norris, D. J. Plasmonic Films Can Easily Be Better: Rules and Recipes. *ACS Photonics* **2015**, *2*, 326–333.

[214] Højlund-Nielsen, E.; Clausen, J.; Mäkela, T.; Thamdrup, L. H.; Zalkovskij, M.; Nielsen, T.; Li Pira, N.; Ahopelto, J.; Mortensen, N. A.; Kristensen, A. Plasmonic Colors: Toward Mass Production of Metasurfaces. *Advanced Materials Technologies* **2016**, *1*, 1600054.

[215] Guo, H. C.; Nau, D.; Radke, A.; Zhang, X. P.; Stodolka, J.; Yang, X. L.; Tikhodeev, S. G.; Gippius, N. A.; Giessen, H. Large-area metallic photonic crystal fabrication with interference lithography and dry etching. *Applied Physics B* **2005**, *81*, 271–275.

[216] Xia, D.; Ku, Z.; Lee, S. C.; Brueck, S. R. J. Nanostructures and Functional Materials Fabricated by Interferometric Lithography. *Advanced Materials* **2011**, *23*, 147–179.

[217] Vala, M.; Homola, J. Flexible method based on four-beam interference lithography for fabrication of large areas of perfectly periodic plasmonic arrays. *Optics Express* **2014**, *22*, 18778–18789.

[218] van Wolferen, H.; Adelmann, L. In *Lithography: Principles, Processes and Materials*; Hennessy, T. C., Ed.; 2011; pp 133–148.

[219] Bagheri, S.; Strohfeldt, N.; Sterl, F.; Berrier, A.; Tittl, A.; Giessen, H. Large-Area Low-Cost Plasmonic Perfect Absorber Chemical Sensor Fabricated by Laser Interference Lithography. *ACS Sensors* **2016**, *1*, 1148–1154.

[220] Chou, S. Y. Nanoimprint lithography. *Journal of Vacuum Science & Technology B: Microelectronics and Nanometer Structures* **1996**, *14*, 4129–4133.

[221] Guo, L. J. Nanoimprint Lithography: Methods and Material Requirements. *Advanced Materials* **2007**, *19*, 495–513.

[222] Hegner, M.; Wagner, P.; Semenza, G. Ultralarge atomically flat template-stripped Au surfaces for scanning probe microscopy. *Surface Science* **1993**, *291*, 39–46.

[223] Nagpal, P.; Lindquist, N. C.; Oh, S. H.; Norris, D. J. Ultrasmooth Patterned Metals for Plasmonics and Metamaterials. *Science* **2009**, *325*, 594–597.

[224] Dong, Z.; Asbahi, M.; Lin, J.; Zhu, D.; Wang, Y. M.; Hippalgaonkar, K.; Chu, H.-S.; Goh, W. P.; Wang, F.; Huang, Z.; Yang, J. K. W. Second-Harmonic Generation from Sub-5 nm Gaps by Directed Self-Assembly of Nanoparticles onto Template-Stripped Gold Substrates. *Nano Letters* **2015**, *15*, 5976–5981.

[225] Yoo, D.; Johnson, T. W.; Cherukulappurath, S.; Norris, D. J.; Oh, S.-H. Template-Stripped Tunable Plasmonic Devices on Stretchable and Rollable Substrates. *ACS Nano* **2015**, *9*, 10647–10654.

[226] Ahn, S. H.; Guo, L. J. Large-Area Roll-to-Roll and Roll-to-Plate Nanoimprint Lithography: A Step toward High-Throughput Application of Continuous Nanoimprinting. *ACS Nano* **2009**, *3*, 2304–2310.

[227] Murthy, S.; Matschuk, M.; Huang, Q.; Mandsberg, N. K.; Feidenhans'l, N. A.; Johansen, P.; Christensen, L.; Pranov, H.; Kofod, G.; Pedersen, H. C.; Hassager, O.; Taboryski, R. Fabrication of Nanostructures by Roll-to-Roll Extrusion Coating. *Advanced Engineering Materials* **2015**, *18*, 484–489.

[228] Kaplan, A. F.; Xu, T.; Wu, Y.-K.; Guo, L. J. Multilayer pattern transfer for plasmonic color filter applications. *Journal of Vacuum Science & Technology B: Microelectronics and Nanometer Structures* **2010**, *28*, C6O60–C6063.

[229] Chen, Q.; Martin, C.; Cumming, D. R. S. Transfer Printing of Nanoplasmonic Devices onto Flexible Polymer Substrates from a Rigid Stamp. *Plasmonics* **2012**, *7*, 755–761.

[230] Bagheri, S.; Weber, K.; Gissibl, T.; Weiss, T.; Neubrech, F.; Giessen, H. Fabrication of Square-Centimeter Plasmonic Nanoantenna Arrays by Femtosecond Direct Laser Writing Lithography: Effects of Collective Excitations on SEIRA Enhancement. *ACS Photonics* **2015**, *2*, 779–786.

[231] Bagheri, S.; Zgrabik, C. M.; Gissibl, T.; Tittl, A.; Sterl, F.; Walter, R.; De Zuani, S.; Berrier, A.; Stauden, T.; Richter, G.; Hu, E. L.; Giessen, H. Large-area fabrication of TiN nanoantenna arrays for refractory plasmonics in the mid-infrared by femtosecond direct laser writing and interference lithography [Invited]. *Optical Materials Express* **2015**, *5*, 2625–2633.

[232] Zhao, J.; Frank, B.; Burger, S.; Giessen, H. Large-Area High-Quality Plasmonic Oligomers Fabricated by Angle-Controlled Colloidal Nanolithography. *ACS Nano* **2011**, *5*, 9009–9016.

[233] Chen, H. L.; Chuang, S. Y.; Cheng, H. C.; Lin, C. H.; Chu, T. C. Directly patterning metal films by nanoimprint lithography with low-temperature and low-pressure. *Microelectronic Engineering* **2006**, *83*, 893–896.

[234] Auzelyte, V.; Gallinet, B.; Flauraud, V.; Santschi, C.; Dutta-Gupta, S.; Martin, O. J. F.; Brugger, J. Large-Area Gold/Parylene Plasmonic Nanostructures Fabricated by Direct Nanocutting. *Advanced Optical Materials* **2013**, *1*, 50–54.

[235] Cadusch, J. J.; Panchenko, E.; Kirkwood, N.; James, T. D.; Gibson, B. C.; Webb, K. J.; Mulvaney, P.; Roberts, A. Emission enhancement and polarization of semiconductor quantum dots with nanoimprinted plasmonic cavities: towards scalable fabrication of plasmon-exciton displays. *Nanoscale* **2015**, *7*, 13816–13821.

[236] Do, J.; Fedoruk, M.; Jäckel, F.; Feldmann, J. Two-Color Laser Printing of Individual Gold Nanorods. *Nano Letters* **2013**, *13*, 4164–4168.

[237] Zijlstra, P.; Chon, J. W. M.; Gu, M. Five-dimensional optical recording mediated by surface plasmons in gold nanorods. *Nature* **2009**, *459*, 410–413.

[238] Kim, J. Y.; Ingrosso, C.; Fakhfouri, V.; Striccoli, M.; Agostiano, A.; Curri, M. L.; Brugger, J. Inkjet-Printed Multicolor Arrays of Highly Luminescent Nanocrystal-Based Nanocomposites. *Small* **2009**, *5*, 1051–1057.

[239] Yakovlev, A. V.; Milichko, V. A.; Vinogradov, V. V.; Vinogradov, A. V. Inkjet Color Printing by Interference Nanostructures. *ACS Nano* **2016**, *10*, 3078–3086.

[240] Richner, P.; Galliker, P.; Lendenmann, T.; Kress, S. J. P.; Kim, D. K.; Norris, D. J.; Poulikakos, D. Full-Spectrum Flexible Color Printing at the Diffraction Limit. *ACS Photonics* **2016**, *3*, 754–757.

[241] Richner, P.; Eghlidi, H.; Kress, S. J. P.; Schmid, M.; Norris, D. J.; Poulikakos, D. Printable Nanoscopic Metamaterial Absorbers and Images with Diffraction-Limited Resolution. *ACS Applied Materials & Interfaces* **2016**, *8*, 11690–11697.

[242] Luetolf, F.; Dümpelmann, L.; Bosshard, C. Poster "Custom Nanostructures: From Design to Applications". Swiss Nano Convention. 2014; pp 1–1.

[243] Ahn, S. H.; Guo, L. J. High-Speed Roll-to-Roll Nanoimprint Lithography on Flexible Plastic Substrates. *Advanced Materials* **2008**, *20*, 2044–2049.

[244] Gallinet, B.; Butet, J.; Martin, O. J. F. Numerical methods for nanophotonics: standard problems and future challenges. *Laser & Photonics Reviews* **2015**, *9*, 577–603.

[245] Yee, K. S. Numerical Solution of Initial Boundary Value Problems Involving Maxwells Equations in Isotropic Media. *IEEE Transactions on Antennas and Propagation* **1966**, *14*, 302–307.

[246] Taflove, A.; Hagness, S. C. Computational Electrodynamics: The Finite-Difference Time-Domain Method. *Artech House* **2005**,

[247] Jin, J.-M. *The finite element method in electromagnetics*; John Wiley & Sons, 2014.

[248] Kern, A. M.; Martin, O. J. F. Surface integral formulation for 3D simulations of plasmonic and high permittivity nanostructures. *Journal of the Optical Society of America A* **2009**, *26*, 732–740.

[249] Gallinet, B.; Kern, A. M.; Martin, O. J. F. Accurate and versatile modeling of electromagnetic scattering on periodic nanostructures with a surface integral approach. *Journal of the Optical Society of America A* **2010**, *27*, 2261–2271.

[250] Moharam, M. G.; Gaylord, T. K. Rigorous coupled-wave analysis of planar-grating diffraction. *Journal of the Optical Society of America* **1981**, *71*, 811–818.

[251] West, P. R.; Ishii, S.; Naik, G. V.; Emani, N. K.; Shalaev, V. M.; Boltasseva, A. Searching for better plasmonic materials. *Laser & Photonics Reviews* **2010**, *4*, 795–808.

[252] Murray, W. A.; Barnes, W. L. Plasmonic Materials. *Advanced Materials* **2007**, *19*, 3771–3782.

[253] Khurgin, J. B.; Sun, G. In search of the elusive lossless metal. *Applied Physics Letters* **2010**, *96*, 181102.

[254] Boltasseva, A.; Atwater, H. A. Low-Loss Plasmonic Metamaterials. *Science* **2011**, *331*, 290–291.

[255] Naik, G. V.; Shalaev, V. M.; Boltasseva, A. Alternative Plasmonic Materials: Beyond Gold and Silver. *Advanced Materials* **2013**, *25*, 3264–3294.

[256] Ndukaife, J. C.; Shalaev, V. M.; Boltasseva, A. Plasmonics–turning loss into gain. *Science* **2016**, *351*, 334–335.

[257] Langhammer, C.; Schwind, M.; Kasemo, B.; Zorić, I. Localized Surface Plasmon Resonances in Aluminum Nanodisks. *Nano Letters* **2008**, *8*, 1461–1471.

[258] Knight, M. W.; King, N. S.; Liu, L.; Everitt, H. O.; Nordlander, P.; Halas, N. J. Aluminum for Plasmonics. *ACS Nano* **2013**, *8*, 834–840.

[259] Babicheva, V. E.; Kinsey, N.; Naik, G. V.; Ferrera, M.; Lavrinenko, A. V.; Shalaev, V. M.; Boltasseva, A. Towards CMOS-compatible nanophotonics: Ultra-compact modulators using alternative plasmonic materials. *Optics Express* **2013**, *21*, 27326–27337.

[260] Kostarelos, K.; Novoselov, K. S. Exploring the Interface of Graphene and Biology. *Science* **2014**, *344*, 261–263.

[261] Guler, U.; Boltasseva, A.; Shalaev, V. M. Refractory Plasmonics. *Science* **2014**, *344*, 263–264.

[262] Strohfeldt, N.; Tittl, A.; Schäferling, M.; Neubrech, F.; Kreibig, U.; Griessen, R.; Giessen, H. Yttrium Hydride Nanoantennas for Active Plasmonics. *Nano Letters* **2014**, *14*, 1140–1147.

[263] Sterl, F.; Strohfeldt, N.; Walter, R.; Griessen, R.; Tittl, A.; Giessen, H. Magnesium as Novel Material for Active Plasmonics in the Visible Wavelength Range. *Nano Letters* **2015**, *15*, 7949–7955.

[264] Shrestha, V. R.; Lee, S.-S.; Kim, E.-S.; Choi, D.-Y. Aluminum Plasmonics Based Highly Transmissive Polarization-Independent Subtractive Color Filters Exploiting a Nanopatch Array. *Nano Letters* **2014**, *14*, 6672–6678.

[265] Sun, S.; Ye, Z.; Guo, L.; Sun, N. Wide-incident-angle chromatic polarized transmission on trilayer silver/dielectric nanowire gratings. *Journal of the Optical Society of America B* **2014**, *31*, 1211.

[266] Shin, Y. J.; Wu, Y.-K.; Lee, K.-T.; Ok, J. G.; Guo, L. J. Fabrication and Encapsulation of a Short-Period Wire Grid Polarizer with Improved Viewing Angle by the Angled-Evaporation Method. *Advanced Optical Materials* **2013**, *1*, 863–868.

[267] Ye, F.; Burns, M. J.; Naughton, M. J. Structured metal thin film as an asymmetric color filter: the forward and reverse plasmonic halos. *Scientific Reports* **2014**, *4*, 1–5.

[268] Lochbihler, H. Polarizing and angle-sensitive color filter in transmittance for security feature applications. *Advanced Optical Technologies* **2015**, *4*, 71–77.

[269] van Renesse, R. L. In *Holography, The first Years*; Fournier, J. M., Ed.; 2003.

[270] Kaplan, A. F.; Xu, T.; Jay Guo, L. High efficiency resonance-based spectrum filters with tunable transmission bandwidth fabricated using nanoimprint lithography. *Applied Physics Letters* **2011**, *99*, 143111.

[271] Watt, F.; Bettiol, A. A.; van KAN, J. A. V.; van Kan, J. A.; Teo, E. J.; Breese, M. B. H. Ion Beam Lithography and Nanofabrication: A Review. *International Journal of Nanoscience* **2005**, *4*, 269–286.

[272] Manfrinato, V. R.; Zhang, L.; Su, D.; Duan, H.; Hobbs, R. G.; Stach, E. A.; Berggren, K. K. Resolution Limits of Electron-Beam Lithography toward the Atomic Scale. *Nano Letters* **2013**, *13*, 1555–1558.

[273] Sanders, D. P. Advances in Patterning Materials for 193 nm Immersion Lithography. *Chemical Reviews* **2010**, *110*, 321–360.

[274] Bloomstein, T. M.; Marchant, M. F.; Deneault, S.; Hardy, D. E.; Rothschild, M. 22-nm immersion interference lithography. *Optics Express* **2006**, *14*, 6434–6443.

[275] Sidharthan, R.; Murukeshan, V. M.; Sathiyamoorthy, K. Sub-60 nm Periodic Grating Feature Patterning by Immersion Based 364 nm Laser Interference. *Journal of Nanoscience and Nanotechnology* **2012**, *12*, 6428–6431.

[276] Artar, A.; Yanik, A. A.; Altug, H. Directional Double Fano Resonances in Plasmonic Hetero-Oligomers. *Nano Letters* **2011**, *11*, 3694–3700.

[277] Liu, T.; Shen, Y.; Shin, W.; Zhu, Q.; Fan, S.; Jin, C. Dislocated Double-Layer Metal Gratings: An Efficient Unidirectional Coupler. *Nano Letters* **2014**, *14*, 3848–3854.

[278] Christ, A.; Martin, O. J. F.; Ekinci, Y.; Gippius, N. A.; Tikhodeev, S. G. Symmetry Breaking in a Plasmonic Metamaterial at Optical Wavelength. *Nano Letters* **2008**, *8*, 2171–2175.

[279] Palomba, S.; Danckwerts, M.; Novotny, L. Nonlinear plasmonics with gold nanoparticle antennas. *Journal of Optics A: Pure and Applied Optics* **2009**, *11*, 114030.

[280] Kauranen, M.; Zayats, A. V. Nonlinear plasmonics. *Nature Photonics* **2012**, *6*, 737–748.

[281] Luk'yanchuk, B.; Zheludev, N. I.; Maier, S. A.; Halas, N. J.; Nordlander, P.; Giessen, H.; Chong, T. C. The Fano resonance in plasmonic nanostructures and metamaterials. *Nature Materials* **2010**, *9*, 707–715.

[282] Gallinet, B.; Martin, O. J. F. Influence of Electromagnetic Interactions on the Line Shape of Plasmonic Fano Resonances. *ACS Nano* **2011**, *5*, 8999–9008.

[283] Tittl, A.; Harats, M. G.; Walter, R.; Yin, X.; Schäferling, M.; Liu, N.; Rapaport, R.; Giessen, H. Quantitative Angle-Resolved Small-Spot Reflectance Measurements on Plasmonic Perfect Absorbers: Impedance Matching and Disorder Effects. *ACS Nano* **2014**, *8*, 10885–10892.

[284] Christ, A.; Zentgraf, T.; Tikhodeev, S.; Gippius, N.; Kuhl, J.; Giessen, H. Controlling the interaction between localized and delocalized surface plasmon modes: Experiment and numerical calculations. *Physical Review B* **2006**, *74*, 155435.

[285] Kravets, V.; Schedin, F.; Grigorenko, A. Extremely Narrow Plasmon Resonances Based on Diffraction Coupling of Localized Plasmons in Arrays of Metallic Nanoparticles. *Physical review letters* **2008**, *101*, 087403.

[286] Novotny, L. Strong coupling, energy splitting, and level crossings: A classical perspective. *American Journal of Physics* **2010**, *78*, 1199–1202.

[287] Lovera, A.; Gallinet, B.; Nordlander, P.; Martin, O. J. F. Mechanisms of Fano Resonances in Coupled Plasmonic Systems. *ACS Nano* **2013**, *7*, 4527–4536.

[288] Törmä, P.; Barnes, W. L. Strong coupling between surface plasmon polaritons and emitters: a review. *Reports on Progress in Physics* **2014**, 1–34.

[289] Prodan, E.; Radloff, C.; Halas, N. J.; Nordlander, P. A Hybridization Model for the Plasmon Response of Complex Nanostructures. *Science* **2003**, *302*, 419–422.

[290] Gallinet, B. Fano Resonances in Plasmonic Nanostructures: Fundamentals, Numerical Modeling and Applications. *Thesis* **2012**, 1–120.

[291] Fairchild, M. D. Color appearance models. John Wiley & Sons, Ltd, Chichester, UK, 2013.

[292] de Gans, B. J.; Duineveld, P. C.; Schubert, U. S. Inkjet Printing of Polymers: State of the Art and Future Developments. *Advanced Materials* **2004**, *16*, 203–213.

[293] Galliker, P.; Schneider, J.; Eghlidi, H.; Kress, S.; Sandoghdar, V.; Poulikakos, D. Direct printing of nanostructures by electrostatic autofocussing of ink nanodroplets. *Nature Communications* **2012**, *3*, 890.

[294] Maystre, D. Rigorous vector theories of diffraction gratings. *Progress in optics* **1984**, *21*, 1–67.

[295] Qiao, W.; Huang, W.; Liu, Y.; Li, X.; Chen, L.-S.; Tang, J.-X. Toward Scalable Flexible Nanomanufacturing for Photonic Structures and Devices. *Advanced Materials* **2016**, *28*, 10353–10380.

[296] Barnes, W. L.; Dereux, A.; Ebbesen, T. W. Surface plasmon subwavelength optics. *Nature* **2003**, *424*, 824–830.

[297] Zheng, B. Y.; Wang, Y.; Nordlander, P.; Halas, N. J. Color-Selective and CMOS-Compatible Photodetection Based on Aluminum Plasmonics. *Advanced Materials* **2014**, *26*, 6318–6323.

[298] Vilas, J. L.; Sanchez-Brea, L. M.; Bernabeu, E. Optimal achromatic wave retarders using two birefringent wave plates. *Applied Optics* **2013**, *52*, 1892–1896.

[299] Kang, G.; Tan, Q.; Wang, X.; Jin, G. Achromatic phase retarder applied to MWIR & LWIR dual-band. *Optics Express* **2010**, *18*, 1695–1703.

[300] Li, T.; Liu, H.; Wang, S.-M.; Yin, X.-G.; Wang, F.-M.; Zhu, S.-N.; Zhang, X. Manipulating optical rotation in extraordinary transmission by hybrid plasmonic excitations. *Applied Physics Letters* **2008**, *93*, 021110.

[301] Biagioni, P.; Savoini, M.; Huang, J.-S.; Duò, L.; Finazzi, M.; Hecht, B. Near-field polarization shaping by a near-resonant plasmonic cross antenna. *Physical Review B* **2009**, *80*, 153409.

[302] Zhao, Y.; Alù, A. Manipulating light polarization with ultrathin plasmonic metasurfaces. *Physical Review B* **2011**, *84*, 205428.

[303] Sambles, J. R.; Bradbery, G. W.; Yang, F. Optical excitation of surface plasmons: An introduction. *Contemporary Physics* **1991**, *32*, 173–183.

[304] Park, C.-H.; Yoon, Y.-T.; Shrestha, V. R.; Park, C.-S.; Lee, S.-S.; Kim, E.-S. Electrically tunable color filter based on a polarization-tailored nano-photonic dichroic resonator featuring an asymmetric subwavelength grating. *Optics Express* **2013**, *21*, 28783.

[305] Lee, K. M.; Tondiglia, V. P.; McConney, M. E.; Natarajan, L. V.; Bunning, T. J.; White, T. J. Color-Tunable Mirrors Based on Electrically Regulated Bandwidth Broadening in Polymer-Stabilized Cholesteric Liquid Crystals. *ACS Photonics* **2014**, *1*, 1033–1041.

[306] Franklin, D.; Chen, Y.; Vazquez-Guardado, A.; Modak, S.; Boroumand, J.; Xu, D.; Wu, S.-T.; Chanda, D. Polarization-independent actively tunable colour generation on imprinted plasmonic surfaces. *Nature Communications* **2015**, *6*, 1–8.

[307] Xu, Q.; Chen, L.; Wood, M. G.; Sun, P.; Reano, R. M.; Wood, M. G.; Reano, R. M. Electrically tunable optical polarization rotation on a silicon chip using Berry's phase. *Nature Communications* **2014**, *5*, 5337.

[308] Huang, C.-p.; Wang, Q.-j.; Yin, X.-g.; Zhang, Y.; Li, J.-q.; Zhu, Y.-y. Break Through the Limitation of Malus' Law with Plasmonic Polarizers. *Advanced Optical Materials* **2014**, *2*, 723–728.

[309] Kokhanovsky, A. A. Light Scattering Reviews 4. Springer Berlin Heidelberg, Berlin, Heidelberg, 2016.

[310] Liu, M.; Zhang, X. Nano-optics: Plasmon-boosted magneto-optics. *Nature Photonics* **2013**, *7*, 429–430.

[311] Garini, Y.; Young, I. T.; McNamara, G. Spectral imaging: Principles and applications. *Cytometry Part A* **2006**, *69A*, 735–747.

[312] Lillesand, T.; Kiefer, R. W.; Chipman, J. Remote sensing and image interpretation. John Wiley & Sons, 2014.

[313] ElMasry, G.; Sun, D.-W.; Allen, P. Near-infrared hyperspectral imaging for predicting colour, pH and tenderness of fresh beef. *Journal of Food Engineering* **2012**, *110*, 127–140.

[314] Qin, J.; Chao, K.; Kim, M. S.; Lu, R.; Burks, T. F. Hyperspectral and multispectral imaging for evaluating food safety and quality. *Journal of Food Engineering* **2013**, *118*, 157–171.

[315] Lu, G.; Fei, B. Medical hyperspectral imaging: a review. *Journal of Biomedical Optics* **2014**, *19*, 010901.

[316] Ozeki, Y.; Umemura, W.; Otsuka, Y.; Satoh, S.; Hashimoto, H.; Sumimura, K.; Nishizawa, N.; Fukui, K.; Itoh, K. High-speed molecular spectral imaging of tissue with stimulated Raman scattering. *Nature Photonics* **2012**, *6*, 845–851.

[317] Liang, H. Advances in multispectral and hyperspectral imaging for archaeology and art conservation. *Applied Physics A* **2011**, *106*, 309–323.

[318] Apfel, J. H.; Illsley, R. F.; Thelen, A. J. Circular variable filter. *US Patent* **1969**, 1–11.

[319] Gunning, W.; Pasko, J.; Tracy, J. A Liquid Crystal Tunable Spectral Filter: Visible And Infrared Operation. *1981 Los Angeles Technical Symposium* **1981**, *0268*, 190–194.

[320] Hagen, N.; Kudenov, M. W. Review of snapshot spectral imaging technologies. *Optical Engineering* **2013**, *52*, 090901.

[321] Geelen, B.; Tack, N.; Lambrechts, A. A snapshot multispectral imager with integrated tiled filters and optical duplication. *Proceedings of SPIE* **2013**, *8613*, 861314.

[322] Lapray, P.-J.; Wang, X.; Thomas, J.-B.; Gouton, P. Multispectral Filter Arrays: Recent Advances and Practical Implementation. *Sensors* **2014**, *14*, 21626–21659.

[323] Shogenji, R.; Kitamura, Y.; Yamada, K.; Miyatake, S.; Tanida, J. Multispectral imaging using compact compound optics. *Optics Express* **2004**, *12*, 1643–1655.

[324] Imai, F. H.; Berns, R. S. Spectral estimation using trichromatic digital cameras. *Proceedings of the International Symposium on Multispectral Imaging and Color Reproduction for Digital Archives* **1999**, *42*, 1–8.

[325] Bacon, C. P.; Mattley, Y.; DeFrece, R. Miniature spectroscopic instrumentation: Applications to biology and chemistry. *Review of Scientific Instruments* **2004**, *75*, 1–16.

[326] Bao, J.; Bawendi, M. G. A colloidal quantum dot spectrometer. *Nature* **2015**, *523*, 67–70.

[327] Tittl, A.; Michel, A. K. U.; Schäferling, M.; Yin, X.; Gholipour, B.; Cui, L.; Wuttig, M.; Taubner, T.; Neubrech, F.; Giessen, H. A Switchable Mid-Infrared Plasmonic Perfect Absorber with Multispectral Thermal Imaging Capability. *Advanced Materials* **2015**, *27*, 4597–4603.

[328] Park, H.; Crozier, K. B. Multispectral imaging with vertical silicon nanowires. *Scientific Reports* **2013**, *3*, 2460.

[329] Stigell, P.; Miyata, K.; Hauta-Kasari, M. Wiener estimation method in estimating of spectral reflectance from RGB images. *Pattern Recognition and Image Analysis* **2007**, *17*, 233–242.

[330] Strang, G. *Introduction to linear algebra*; Wellesley-Cambridge Press, 2016.

[331] Connah, D.; Westland, S.; Thomson, M. G. A. Recovering spectral information using digital camera systems. *Coloration Technology* **2001**, *117*, 309–312.

[332] Kandi, G. Representing Spectral Data Using Lab PQR Color Space in Comparison with PCA Method. *Progress in Color, Colorants and Coatings* **2011**, *4*, 95–106.

[333] Tzeng, D.-Y.; Berns, R. S. A review of principal component analysis and its applications to color technology. *Color Research & Application* **2005**, *30*, 84–98.

[334] Haneishi, H.; Hasegawa, T.; Hosoi, A.; Yokoyama, Y.; Tsumura, N.; Miyake, Y. System design for accurately estimating the spectral reflectance of art paintings. *Applied Optics* **2000**, *39*, 6621–6632.

[335] Sharma, G.; Wu, W.; Dalal, E. N. The CIEDE2000 color-difference formula: Implementation notes, supplementary test data, and mathematical observations. *Color Research & Application* **2005**, *30*, 21–30.

[336] Tsumura, N.; Sato, H.; Hasegawa, T.; Haneishi, H.; Miyake, Y. Limitation of Color Samples for Spectral Estimation from Sensor Responses in Fine Art Painting. *Optical Review* **1999**, *6*, 57–61.

[337] Shen, H.-L.; Cai, P.-Q.; Shao, S.-J.; Xin, J. H. Reflectance reconstruction for multispectral imaging by adaptive Wiener estimation. *Optics Express* **2007**, *15*, 15545–15554.

[338] Agahian, F.; Amirshahi, S. A.; Amirshahi, S. H. Reconstruction of reflectance spectra using weighted principal component analysis. *Color Research & Application* **2008**, *33*, 360–371.

[339] Urban, P.; Rosen, M. R.; Berns, R. S. A Spatially Adaptive Wiener Filter for Reflectance Estimation. *Color and Imaging Conference* **2008**, *1*, 279–284.

[340] Kimmel, R. Demosaicing: image reconstruction from color CCD samples. *IEEE Transactions on Image Processing* **1999**, *8*, 1221–1228.

[341] Alleysson, D.; Süsstrunk, S. Influence of spectral sensitivity functions on color demosaicing. *Color and Imaging Conference* **2003**, *2003*, 351–357.

A   Abbreviations

α	evaporation angle
β	prism angle
δ	incident angle of laser onto photoresist
γ	tilt angle parallel to periodic nanostructures
λ	wavelength of light
λ_R	wavelength of the plasmon resonance
Φ	rotation angle of the sample
ψ_p	phase of p-pol
ψ_s	phase of s-pol
ψ_{diff}	phase difference between s-pol and p-pol
θ	tilt angle perpendicular to periodic nanostructures
φ	rotation angle of a polarizer
φ_1	rotation angle of input polarizer
φ_2	rotation angle of analyzing polarizer
dc	duty cycle
E	electric field
k	wavevector

n refractive index of material

p period

*, λ_R, † and #   positions before, at, above and far above the plasmon resonance

B/W   black and white

CMOS   complementary metal-oxide-semiconductor

EBL   electron-beam lithography

FDTD   finite difference in time domain

FIB   focussed ion beam

FOV   field-of-view

FWHM   full width half maximum

LSPR   localized surface plasmon resonance

p-pol   p-polarization, transverse-magnetic (TM)

PMSI   plasmonic multispectral imaging

PPR   plasmonic phase retarder

PR   propagating resonance

PSPR   propagating surface plasmon resonance

PTF   plasmonic tunable filter

RCWA   rigorous coupled wave analysis

RGB   additive color model based on red, green and blue

RI   refractive index

s-pol   s-polarization, transverse-electric (TE)

SIE   surface integral equation

UV   ultraviolet

WR   Wood Rayleigh anomaly

Curriculum Vitae

Personal Information

Name: Luc Duempelmann

Date of birth: December 15, 1986

Nationality: Swiss, German

Email: luc.duempelmann@gmail.com

ORCID: 0000-0002-7552-543X

Education

2013-2017	PhD candidate at the Centre Suisse d'Electronique et Microtechnique (CSEM SA), enrolled in the Departement of Information Technology and Electrical Engineering at the Swiss Federal Institute of Technology in Zürich (ETH Zurich), October 2013 to February 2017.
2009-2012	Master of Science in Nanosciences, Major in Physics, University of Basel
2006-2009	Bachelor of Science in Nanosciences, University of Basel

Languages

German	native, CEFR[i]: C2
English	fluent/business, CEFR: C1
Spanish	fluent, CEFR: B2
French	conversational, CEFR: A2

---

[i]Common European Framework of Reference for Languages (CEFR), see http://www.cambridgeenglish.org

Peer-reviewed publications

- **L. Duempelmann**, D. Casari, A. Luu-Dinh, B. Gallinet, & L. Novotny, "Color Rendering Plasmonic Aluminum Substrates with Angular Symmetry Breaking". *ACS Nano* **9** (12), 12383–12391 (2015), DOI: 10.1021/acsnano.5b05710

- **L. Duempelmann**, A. Luu-Dinh, B. Gallinet, & L. Novotny, "Four-Fold Color Filter Based on Plasmonic Phase Retarder". *ACS Photonics* **3** (2), 190–196 (2016), DOI: 10.1021/acsphotonics.5b00604

- **L. Duempelmann**, B. Gallinet, & L. Novotny, "Multispectral Imaging with Tunable Plasmonic Filters". *ACS Photonics* **4** (2), 236-241 (2017), DOI: 10.1021/acsphotonics.6b01003

- **L. Duempelmann**, J. Müller, F. Lütolf, B. Gallinet, R. Ferrini, & L. Novotny, "Color Control of Plasmonic Substrates with Inkjet Printing". *Advanced Optical Materials*, **in press** (2017), DOI: 10.1002/adom.201700153

Patents

- G. Basset, B. Gallinet, **L. Duempelmann**, A. Luu-Dinh, J. Sauvage-Vincent, & M. Schnieper. WO2017025277 (A1), 15.08.2015, link

- **L. Duempelmann**, B. Gallinet, 62/409,894 (US62/409,894), 19.10.2016

Non-peer-reviewed publications

- **L. Duempelmann**, B. Gallinet, & L. Novotny, "Nanoimprinted and Angular Evaporated Aluminum Plasmonic Nanoantennas Arrays". *Advanced Photonics* Optical Society of America **JTu2C.5–2** (2014), DOI: 10.1364/BGPP.2014.JTu2C.5

- B. Gallinet, F. Lütolf, **L. Duempelmann**, G. Basset, A. Luu-Dinh, M. Schnieper, and C. Bosshard, "Optical Security Features and Filters Using Plasmonic Nanostructures". *SPIE OPTO*, International Society for Optics and Photonics, 101121E (2017), DOI: 10.1117/12.2250642

White Papers

- **L. Duempelmann**, A. Luu-Dinh, C. Schneider, M. Stalder, B. Gallinet, & M. Schnieper, "Large-scale Fabrication of Nanoimprinted Plasmonic Nanostructures", *CSEM Scientific and Technical Reports 2014*, p. 73, link

- D. Kallweit, **L. Duempelmann**, A. Luu-Dinh, N. Glaser, M. Schnieper, & B. Gallinet, "Magical Watch Dial - Subwavelength Polarizing Nanostructures for Appealing Color Effects", *CSEM Scientific and Technical Reports 2014*, p. 74, link

- **L. Duempelmann**, F. Lütolf, D. Casari, A. Luu-Dinh, G. Basset, & B. Gallinet, "Large-area Plasmonic Substrates Based on Ordered Metallic Nanostructures", *CSEM Scientific and Technical Reports 2015*, p. 41, link

- **L. Duempelmann**, A. Luu-Dinh, & B. Gallinet, "Four Color Filters in one Using Large Area Plasmonic Substrates", *CSEM Scientific and Technical Reports 2016*, p. 52, link

- **L. Duempelmann**, B. Gallinet, D. Casari, A. Luu-Dinh, G. Basset, & M. Schnieper, "Asymmetric Color Appearance with Aluminum Plasmonic Substrates", *CSEM Scientific and Technical Reports 2016*, p. 51, link

- F. Lütolf, J. Müller, **L. Duempelmann**, B. Gallinet, A. Luu-Dinh, G. Basset, & R. Ferrini, "Inkjet Printing Structural Colors Based on Plasmonics", *CSEM Scientific and Technical Reports 2016*, p. 62, link

Presentations

- 6th Gordon Conference on Plasmonics & Nanophotonics (Sunday River, USA, 2016)

- 9th International Nanoscience Student Conference INASCON (Basel, CH, 2015)
  - Best Talk Award

- 40th Micro and Nano Engineering Conference MNE (Lausanne, CH, 2014)

- Advanced Photonics - Optical Sensors OSA (Barcelona, ES, 2014)

Posters

- 6th Gordon Conference on Plasmonics & Nanophotonics (Sunday River, USA, 2016)

- Frontiers in Nanophotonics (Locarno, CH, 2015)

- Swiss Nano Convention (CH: 2013, 2014 and 2015)

Others

- Cover Art of *ACS Photonics*, **3** (2), February 2016. link

- D-ITET Research Photo Competition 2016 - 3rd place, link